Monolayer Transition Metal Dichalcogenide NanoLEDs: Towards High Speed and High Efficiency

By

Kevin Han

A dissertation submitted in partial satisfaction of the

requirements for the degree of

Doctor of Philosophy
in

Engineering – Electrical Engineering and Computer Sciences

in the

Graduate Division

of the

University of California, Berkeley

Committee in charge:

Professor Ming C. Wu, Chair
Professor Ali Javey
Professor Feng Wang

Spring 2019

Abstract

Monolayer Transition Metal Dichalcogenide NanoLEDs:

Towards High Speed and High Efficiency

by

Kevin Han

Doctor of Philosophy in Engineering – Electrical Engineering and Computer Sciences

University of California, Berkeley

Professor Ming C. Wu, Chair

On-chip optical interconnects promise to drastically reduce energy consumption compared to electrical interconnects, which dominate power dissipation in modern integrated circuits (ICs). One key requirement is a low-power, high-efficiency, and high-speed nanoscale light source. However, existing III-V semiconductor light sources face a high surface recombination velocity (SRV ~ 10^4 – 10^6 cm/s) that greatly reduces efficiency at nanoscale sizes. An alternative material system is the monolayer transition metal dichalcogenides (TMDCs), single-molecule-thick direct-bandgap semiconductors that are being investigated for a variety of applications in photonics and electronics. In particular, they are intrinsically nanoscale in one dimension and lack dangling bonds at the surface, leading to high optical efficiency. In addition, they can be electrically injected, transferred to arbitrary substrates, and processed in a top-down manner similar to traditional semiconductors.

However, the development of electrically-injected light emitting devices based on TMDCs is still in an early stage, with relatively few reports of high-efficiency light emission. In this dissertation, we identify current decay over time as the main limitation preventing stable operation of lateral-junction TMDC light-emitting diodes (LEDs), particularly in ambient (non-vacuum) conditions. To solve this, we propose operating WSe_2 LEDs under pulsed voltage, which shows much more stable light emission over time than DC operation (hours vs. seconds of continuous device operation). Electroluminescence (EL) efficiency matches that of photoluminescence, confirming material-quality-limited efficiency. In addition, we demonstrate fast rise and fall times of ~15 ns, a record for TMDC LEDs.

For nanoscale light emitters that require high efficiency at low input power, LEDs are preferred over lasers due to their lack of threshold requirement. The slow speed of LEDs can be greatly enhanced by coupling the emitter to an optical antenna, extending its optical transition dipole

length and resulting in possible ~100x-1000x enhancement of spontaneous emission rate. We experimentally demonstrate three electrically-injected antenna-coupled designs: the double-gate LED coupled to bowtie antennas, the light-emitting capacitor coupled to a slot antenna array, and the single-gate LED coupled to a nanosquare antenna array. The light-emitting capacitor shows very high polarization ratios >30x, and the nanosquare array shows >10x improved intensity over control devices, both indicators of strong antenna enhancement. We discuss the tradeoffs involved in each design. Finally, we theoretically investigate high-speed, highly scaled TMDC nanoLED devices and identify the limits to speed and efficiency. We conclude that edge recombination can be largely overcome with sufficient antenna enhancement, while exciton-exciton annihilation ultimately limits efficiency at high injection levels. Under our model, high speeds >70 GHz can be achieved at modest quantum efficiencies >10%. However, much further work remains in improving material properties and devices.

To my parents

Table of contents

List of Figures

List of Tables

Acknowledgements

This work would not have been possible without the help and support of many others. I would firstly like to thank my advisor, Prof. Ming C. Wu. His knowledge and experience was invaluable in guiding my research down promising avenues, as well as allowing me the freedom to pursue my own ideas. I would also like to thank Prof. Ali Javey for many interesting discussions, which helped move my research forward on many occasions. I'd like to thank Prof. Eli Yablonovitch for serving on my qualifying committee and for his leadership and vision on the nanoLED project, as well as Prof. Feng Wang for serving on my qualifying and dissertation committees.

Many students and postdocs have helped me along the way, both inside and outside the lab. I'd like to thank my mentor, Michael Eggleston, for getting me started in experimental research and serving as an excellent role model. I'd also like to thank Prof. Kyoungsik Yu, Dr. Seth Fortuna, Dr. Kyungmok Kwon, Kevin Messer, Ryan Going, Nicolas Andrade, and Sean Hooten for their help and involvement on the nanoLED project, as well as other members of the Wu group, including Dr. Tae Joon Seok, Dr. Guan Lin Su, Dr. Youmin Wang, Jianheng Luo, and Jodi Loo. I have also benefited greatly from many discussions and collaborations with members of the Javey group, including Matin Amani, Der-Hsien (Danny) Lien, Sujay Desai, Peter Zhao, Hyungjin (Aiden) Kim, Mahmut Tosun, Dr. Tania Roy, George Zhang, Niharika Gupta, Geun Ho Ahn, and Joy Cho.

I am very thankful for the support of the staff of the Marvell NanoLab, as well as BSAC and the E^3S center for providing many opportunities for professional development and sharing my research.

Finally, I'd like to thank my parents for their constant love and support.

Introduction

Lasers have traditionally dominated optical communication due to the high speed of stimulated emission compared to spontaneous emission. However, the speed of spontaneous emission depends not only on the emitter, but also on its optical environment. In particular, by coupling the emitter to an optical antenna, we can increase its effective dipole length from ~1 nm to ~$\lambda/2$, and in doing so speed up spontaneous emission by hundreds or thousands of times, making light-emitting diode (LED) speed competitive with lasers. For short-range communication that requires high efficiency at low power, and where broadband emission may be acceptable, LEDs become even more attractive due to their lack of threshold requirement.

Bulk semiconductor emitters face an efficiency issue when scaled down to the nanoscale, in the form of non-radiative surface recombination. Surface passivation techniques exist but are challenging to implement in a practical nanoLED process. An alternative route is to look for new material systems – namely, low dimensional materials, which inherently avoid surface recombination while having a high surface to volume ratio at the nanoscale. In particular, monolayer transition metal dichalcogenides (TMDCs) are an emerging class of 2D materials that are direct band gap, show bright light emission, can be electrically injected, and are easily processed and transferred to arbitrary substrates. They feature novel excitonic physics that open new opportunities and challenges for nanoLED device design.

This work will discuss the motivation and theory of spontaneous emission enhancement using optical antennas, present TMDCs as a promising active material for nanoLEDs, and analyze future prospects for efficient, high-speed modulation. Chapter 1 introduces nanoLEDs and spontaneous emission rate enhancement. Chapter 2 discusses helium-ion milling, a novel fabrication technique for creating high quality nanoantennas. Chapter 3 provides an overview of monolayer TMDCs. Chapter 4 presents results on pulsed injection of TMDC LEDs to achieve greater device stability and efficiency. Chapter 5 shows electroluminescence results of various antenna-coupled TMDC light emitters and discusses tradeoffs of each. Chapter 6 discusses challenges of device scaling to improve speed while preserving efficiency. Finally, Chapter 7 concludes with a summary and future outlook.

1 Optical communication at the nanoscale

The steady progress of Moore's law, in which transistor density doubles every 18 – 24 months, has led to highly scaled computing systems with billions of transistors per chip. However, as the transistors have become faster, smaller, and lower power, the interconnects have not kept up. Indeed, even in 2004, interconnects consumed over 50% of the power in a high-performance microprocessor [1], and this has likely risen to over 80% today [2]. Electrical interconnects face fundamental limitations on energy consumption that are not improved with scaling. These are in addition to the increased crosstalk, wave reflections, and other design issues that come with high frequency electrical signals [3].

One alternative to electrical wires that avoids these issues is optical interconnects. In fact, optical communication has a long history of displacing electrical wires at shorter and shorter distance scales as the loss of the wires increases at high frequencies (Figure 1). Modern datacenters already use inter-rack and inter-module connections due to higher energy efficiency, lower cost, and lower pin count limitations, and this trend is likely to continue down to the chip scale [4].

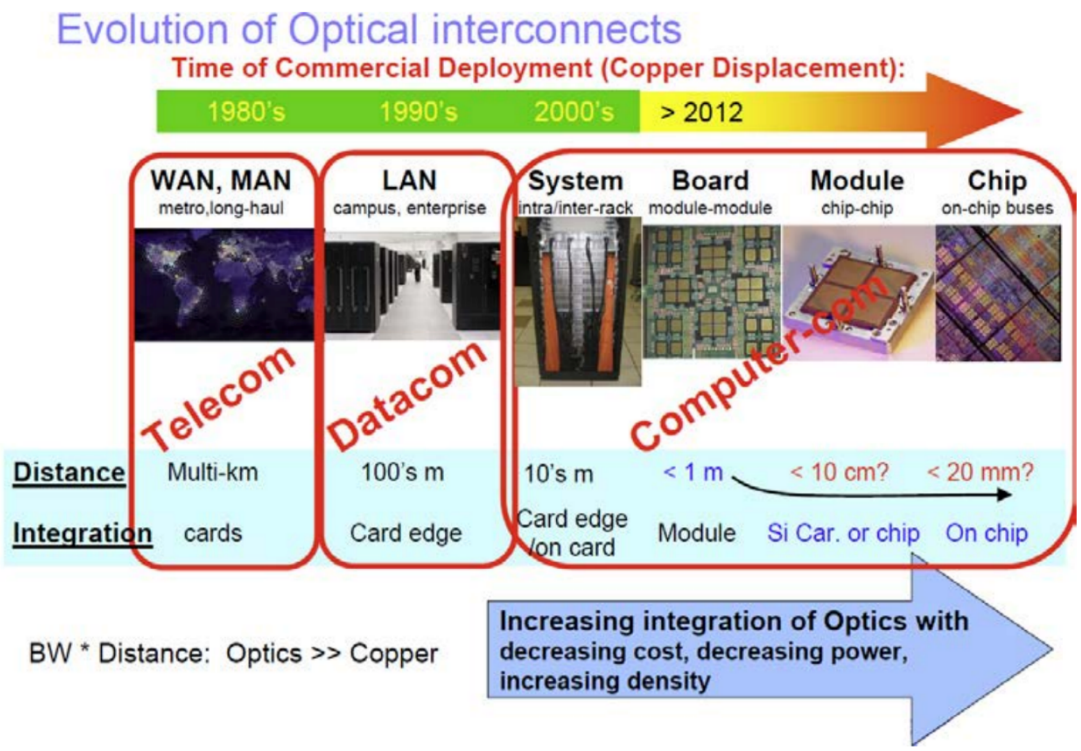

Figure 1. Evolution of optical interconnects from long-haul telecommunications to chip-chip or on-chip interconnects. Reproduced from [4].

1.1 Energy comparison of electrical and optical links

Let us compare the energy required to send one bit for on-chip electrical versus optical links. For an electrical wire, this is essentially the energy it takes to charge the capacitance of the line. The capacitance per unit length of all well-designed electrical lines is $C_l \sim 2$ pF/cm [3]. This basically arises because if we try to make the wire pitch smaller to reduce parallel-plate capacitance from the wire to the ground plane, the fringing-field capacitance to adjacent wires becomes larger, and vice versa [5] (Figure 2). Thus, for a 1 cm global interconnect, the energy is

$$E = \frac{1}{2} C_l l V^2 \cong 1\ pJ/bit \tag{1}$$

One may wonder if this is really the energy cost to send a signal, as a capacitor does not dissipate power alone. However, it is easy to show with a series RC circuit connected to a step voltage signal that the energy dissipated in the resistor as the capacitor charges up is independent of the resistance, and equal to the final energy on the capacitor. For lower resistance, the initial current (power) is higher while the charging time is smaller, and vice versa. This suggests that one way to decrease the energy dissipated is to charge the capacitance more uniformly over time, using a constant current source instead of a voltage source, for example. Indeed, this is the idea of "adiabatic logic", another avenue towards more energy-efficient computation [6]. This is outside of the scope of this work so we will not discuss it further here.

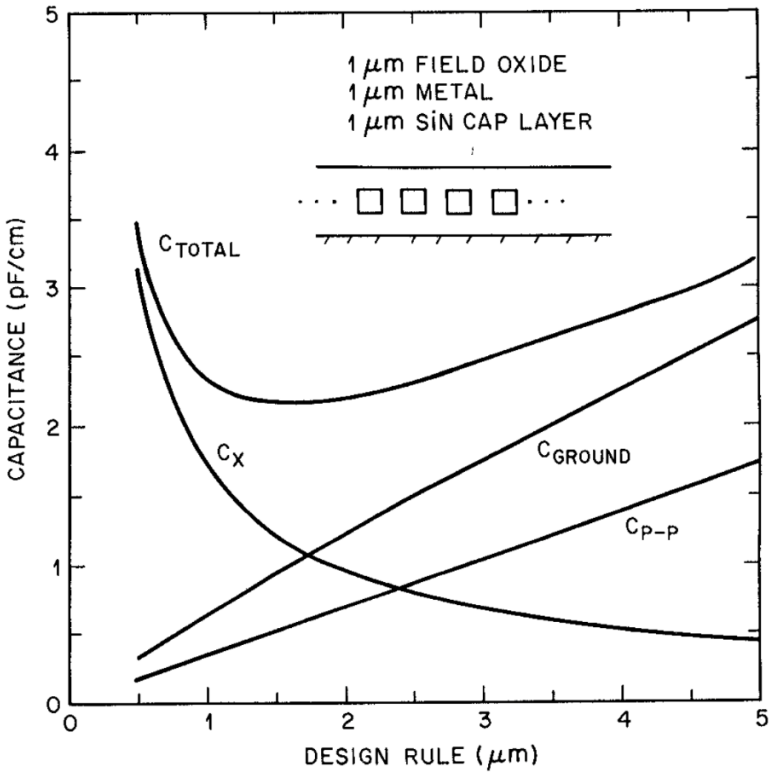

Figure 2. Capacitance per unit length versus wire pitch (design rule). The minimum capacitance is around 2 pF/cm. Reproduced from [5].

For optics, the energy per bit is ideally the energy of the photons needed to send that bit. An ideal coherent state such as that output by a laser is described by Poissonian statistics. The probability of finding n photons is [7]:

$$P_N(n) = e^{-N}\left(\frac{N^n}{n!}\right) \tag{2}$$

where N is the average (expected) number of photons in the mode. For intensity modulation, an "off" bit is represented by zero photons, while an "on" bit is a wave packet with N average photons. Thus, the probability of a bit error is $P_N(0) = e^{-N}$, and the minimum number of photons/bit is determined by the bit error rate (BER) requirement:

$$BER = e^{-N} \tag{3}$$

For a low BER of 10^{-25}, this gives ~58 photons/bit (or half of this, since half the bits are 0). At ~1 eV/photon, this is a mere 9 aJ/bit, over 5 orders of magnitude lower than electrical links!

Note that "thermal" light, such as that output by spontaneous emission or blackbody sources, follows Bose-Einstein statistics instead [7]:

$$P_N(n) = \frac{1}{N+1}\left(\frac{N}{N+1}\right)^n \tag{4}$$

This would seem to preclude any possibility of low power communication, since $P_N(0) = \frac{1}{N+1}$, and we would require an enormous amount of power to ensure such a low BER. However, this is for a single mode (frequency). Of course, such sources are highly broadband, and in the limit of many modes, Poissonian statistics are recovered [7].

1.2 Choice of light source

For most of the history of optical communication, lasers have been the preferred choice over other light sources. Lasers rely on stimulated emission (Figure 3b), producing highly narrowband emission that can be modulated quickly (10s of GHz), ideal for long distance communication. However, the requirements for on-chip links are very different. Here, we would like a light source that is efficient at low powers (~μW) and nanoscale (for high integration density).

Unfortunately, lasers require a threshold current before light is emitted, which is >1 μA at room temperature even for state-of-the-art nanolasers [8]. This is closely related to the difficulty of making a nanoscale laser cavity. The primary way of shrinking an optical mode below the diffraction limit ~$(\lambda/n)^3$ is with plasmonics, which essentially stores energy in the kinetic energy of electrons instead of the magnetic field. This requires a material with negative permittivity, usually a metal. However, metals are highly lossy. For a typical noble metal, the velocity damping rate of electrons is $\gamma_m \sim 10^{14}$ Hz [9]. This leads to a fundamental limit on the threshold current for a deep-sub-wavelength cavity of ~$q\gamma_m \cong 10\ \mu A$ [10]. This arises because energy is stored in the kinetic motion of electrons approximately half the time, and this energy is damped at the rate ~$2\gamma_m$ [9]. We must inject at least one photon (electron) in the cavity during this time to maintain the photon population, leading to the result above. We can avoid this to some extent by engineering the mode to remain in low-loss dielectrics adjacent to the metal [11–13] or avoiding the deep-sub-wavelength regime [14, 15], but the metal loss problem remains challenging to overcome. Indeed, the lowest threshold electrical injection lasers experimentally demonstrated are photonic crystal lasers, which have large footprint (~10 μm) and complex fabrication process [8].

One alternative to lasers is the light-emitting diode (LED), which uses spontaneous emission (Figure 3a). LEDs can be made very efficient at low powers due to their lack of threshold requirement. Also, their broadband emission is not as much a concern at short distances where the effect of dispersion is minimal. However, they have not been used for traditional high-speed communications because spontaneous emission is generally slower than stimulated emission. Fortunately, the rate of spontaneous emission depends not only on the emitter itself but also on

its optical environment. By properly engineering the optical density of states using a cavity (Figure 3c), the spontaneous emission rate can be greatly increased (>1000x), making it competitive with stimulated emission.

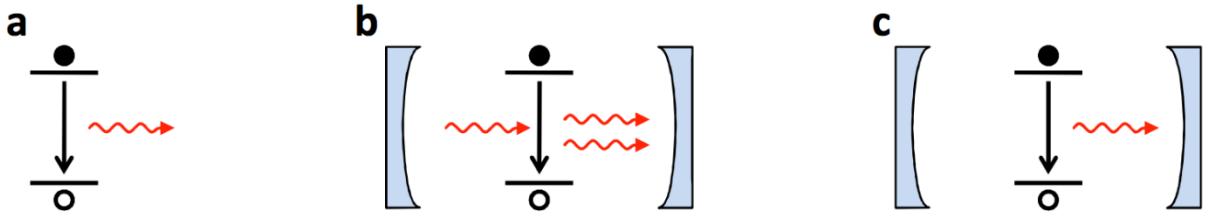

Figure 3. Schematic of optical emitters. a) Spontaneous emission, b) Stimulated emission, c) Cavity-enhanced spontaneous emission. Reproduced from [16].

1.3 Rate enhancement

In this section, we will review the standard theory of rate enhancement using the Purcell effect, present the equivalent classical picture using antenna theory, and discuss some practical considerations in trying to achieve high rate enhancement.

1.3.1 The Purcell effect

Fermi's Golden Rule [17] states that the decay rate from an initial eigenstate $|i\rangle$ of the Hamiltonian to a set of final states $|f\rangle$, to first order in the perturbation H', is given by:

$$\Gamma_{i\to f} = \frac{2\pi}{\hbar}|\langle f|H'|i\rangle|^2\rho(\nu) \tag{5}$$

where $\rho(\nu)$ is the density of final states at the frequency ν. For spontaneous emission, the initial state could be an excited atom, and the final state a ground state atom plus a photon. We can immediately see that the decay rate can be enhanced by increasing the density of final states (DOS). In the case of spontaneous emission, this includes the photonic DOS in the optical environment.

Purcell [18] noted that by placing the emitter in a cavity, the photonic DOS can be enhanced by a factor $\propto Q/V$ over free space, the famous "Purcell factor". Recall that the free space density of photon states per unit volume per unit frequency is

$$\rho_{fs}(\nu) = 8\pi\nu^2/c^3 \tag{6}$$

Assume the cavity has a Lorentzian lineshape:

$$L(\nu) = \frac{\frac{1}{\pi}\left(\frac{1}{2}\Gamma\right)}{(\nu - \nu_0)^2 + \left(\frac{1}{2}\Gamma\right)^2} \tag{7}$$

where Γ is the width. We have $Q = \nu_0/\Gamma$, $L(\nu_0) = 2/\pi\Gamma = 2\mathrm{Q}/\pi\nu_0$, so the cavity DOS at resonance is:

$$\rho_c(\nu_0) = \frac{L(\nu_0)}{V} = \left(\frac{2}{\pi\nu_0}\right)\left(\frac{Q}{V}\right) \tag{8}$$

where V is the volume of the cavity. The ratio of the two is:

$$F \equiv \frac{\rho_c(\nu)}{\rho_{fs}(\nu)} = \left(\frac{3}{4\pi^2}\right)\left(\frac{\lambda}{n}\right)^3\left(\frac{Q}{V}\right) \tag{9}$$

where F is the Purcell factor, and we have added a factor of three for the three polarization directions and accounted for a refractive index n.

This shows that there are two ways to make spontaneous emission faster: increase the cavity Q or decrease mode volume. Since we would like to emit the cavity radiation quickly, increasing the cavity Q only works up to a point, since the cavity lifetime is

$$\tau_{cav} = Q/\omega \tag{10}$$

Decreasing mode volume past the diffraction limit is possible with plasmonics as mentioned above. In this case, however, metal loss can be avoided by compromising on Q, i.e. creating a lossy mode where the energy is radiated quickly. An LED, unlike a laser, does not have a threshold so does not need a high Q. It turns out that this is a highly desirable tradeoff to make, leading to ultrahigh modulation rates with ultrasmall mode volumes $\ll (\lambda/n)^3$ and modest Q factors ~10-50. This can be quickly seen by considering the total lifetime [16]:

$$\tau \cong \sqrt{\tau_{cav}^2 + \left(\frac{\tau_0}{F(Q,V)}\right)^2} \tag{11}$$

where τ_0 is the unenhanced lifetime. For a given mode volume V, speed is maximized when $d\tau/dQ = 0$. After some algebra, this leads to $Q_{opt} \propto \sqrt{V}$, and $F_{opt} \propto 1/\sqrt{V}$ [16]. Thus, the

decrease in mode volume overtakes the decrease in Q, leading to higher speed. Figure 4 shows a more rigorous analysis of modulation bandwidth versus Q and V, assuming the unenhanced emitter can be modulated at 1 GHz. For a given mode volume, there is an optimal quality factor, above which the speed is cavity lifetime limited (grey). Conventional lasers operate with high Q and have difficulty reaching this ultralow mode volume regime.

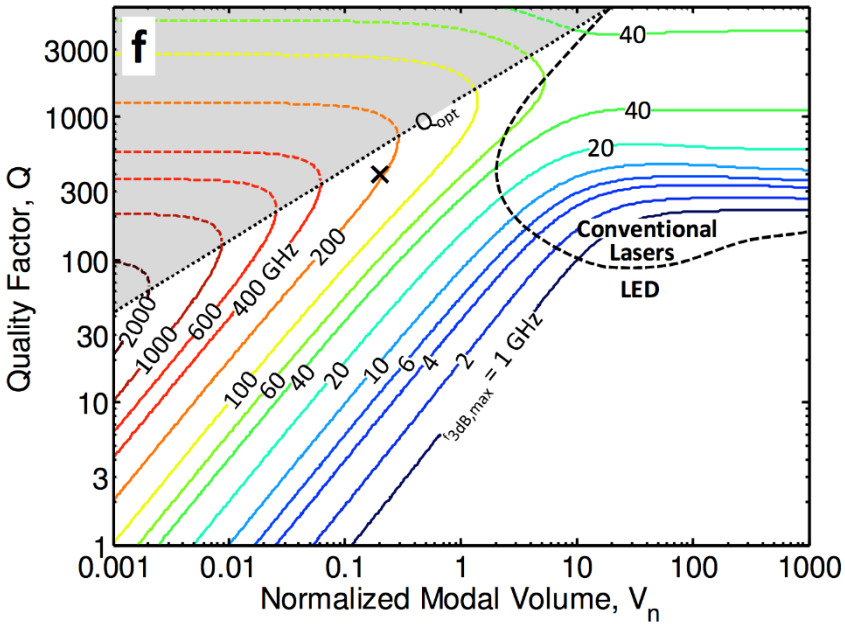

Figure 4. Modulation bandwidth versus quality factor and mode volume, for LEDs and lasers. Reproduced from [16].

1.3.2 Classical optical antenna picture

To guide intuition and design real devices, a classical picture of rate enhancement based on antenna theory is often more useful than the quantum picture above. Most radiative transitions in nature are dipole transitions, so we will be most concerned with dipole emitters. It can be shown using an eigenmode expansion that the local optical density of states is related to the power emitted by a dipole placed at that location [19]:

$$LDOS_l(\boldsymbol{x}_0, \omega) = \frac{4}{\pi}\epsilon(\boldsymbol{x}_0)P_l(\boldsymbol{x}_0, \omega) \tag{12}$$

where $P_l(\boldsymbol{x}_0, \omega)$ is the power radiated by the current source $\boldsymbol{J} = \boldsymbol{e_l}\delta(\boldsymbol{x} - \boldsymbol{x}_0)e^{-i\omega t}$ and $\boldsymbol{e}_l$ is the unit vector in the direction l. Thus, to find the Purcell factor, we can simply look at the power radiated by a dipole at that location in the cavity and divide by the power from the same dipole without a cavity.

The effective dipole length of an atomic emitter is ~0.3 nm, on the order of the atomic spacing. If we imagine the emitter oscillating with a frequency ω, the current is simply $I = q\omega$. The radiation resistance of an infinitesimal dipole is [20]:

$$R_{rad} = \eta\left(\frac{2\pi}{3}\right)\left(\frac{l}{\lambda}\right)^2 \tag{13}$$

where l is the dipole length and $\eta = \sqrt{\mu/\epsilon}$. The power radiated is then

$$P_{fs} = \frac{1}{2}I^2R_{rad} = q^2\omega^2\eta\left(\frac{\pi}{3}\right)\left(\frac{l}{\lambda}\right)^2 \tag{14}$$

Since $l \ll \lambda$, this is a relatively inefficient emitter. We can increase the effective length by coupling to an optical antenna. Consider placing the oscillating dipole between two conductors. By the Shockley-Ramo theorem [21], the current induced on the conductors is

$$I_{ant} = q\omega\left(\frac{l}{d}\right) \tag{15}$$

where d is the distance between the conductors, i.e. the antenna feedgap. If these two conductors form the arms of a short dipole antenna with length L, then the total power radiated is

$$P_{ant} = \frac{1}{2}I_{ant}^2R_{rad,ant} = q^2\omega^2\left(\frac{l}{d}\right)^2\eta\left(\frac{\pi}{12}\right)\left(\frac{L}{\lambda}\right)^2 = P_{fs}\frac{1}{4}\left(\frac{L^2}{d^2}\right) \tag{16}$$

(Note that the radiation resistance of a short dipole is 1/4 that of an infinitesimal dipole.) Thus, the rate enhancement is simply $L^2/4d^2$. It scales as the square inverse of the antenna gap, showing that small antenna gaps $\ll \lambda$ are required for high enhancement. For a half-wave dipole, the enhancement is $\sim\lambda^2/16d^2$, up to a factor since this is not a "short" dipole. For a typical wavelength of ~1 um and d ~ 10 nm, this leads to >500x enhancement!

We can compare the power radiated from antenna theory to the result obtained from the Purcell effect by considering the limit of small gap d, or large gap capacitance. In this case, the mode is highly confined in the gap and the effective mode volume can be estimated as the volume of the gap capacitor (otherwise, it is difficult to calculate mode volume of a general dipole antenna). The simplified equivalent circuit is an RLC resonator shown in Fig. 5a, where R is the lumped resistance of the antenna and ohmic losses, and L is the lumped inductance. For large gap capacitance, the voltage on the capacitor is then

(17)

$$V \cong \frac{q}{C_g}\left(\frac{l}{d}\right)$$

and the power dissipated in the resistor for large R is then

$$P \cong \frac{1}{2}\frac{V^2}{R} = \frac{1}{2R}\left(\frac{q}{C_g}\left(\frac{l}{d}\right)\right)^2 = \frac{(ql)^2\omega_0}{2\epsilon_0}\left(\frac{Q}{V}\right) = \frac{3}{4\pi^2}\lambda^3\left(\frac{Q}{V}\right)P_{fs} \tag{18}$$

where $Q = \left(R\omega_0 C_g\right)^{-1}$, $V = Ad$, $C_g = A\epsilon_0/d$, and A is the capacitor area. P_{fs} is the radiated power in free space found above. Thus, the power radiated by the dipole is enhanced by the Purcell factor derived above.

Real antennas include many non-idealities such as the finite size of the metal, the metal loss, and the antenna reactance (including the kinetic inductance). One way to include these effects is through electromagnetic simulations, usually with finite-difference time-domain (FDTD) methods. By monitoring the total power radiated by a dipole in the cavity plus power dissipated in the metal, and comparing to the same dipole in free space, it is straightforward to find the rate enhancement and external quantum efficiency of the antenna. However, nonlocal effects such as the anomalous skin effect [22] cannot be easily included in FDTD simulations, so an alternative is to develop a circuit model for the antenna (Fig. 5b), as is commonly done in antenna design. This has proven successful in replicating the results from full-wave simulations as well as including the anomalous skin effect [23] (Fig. 6).

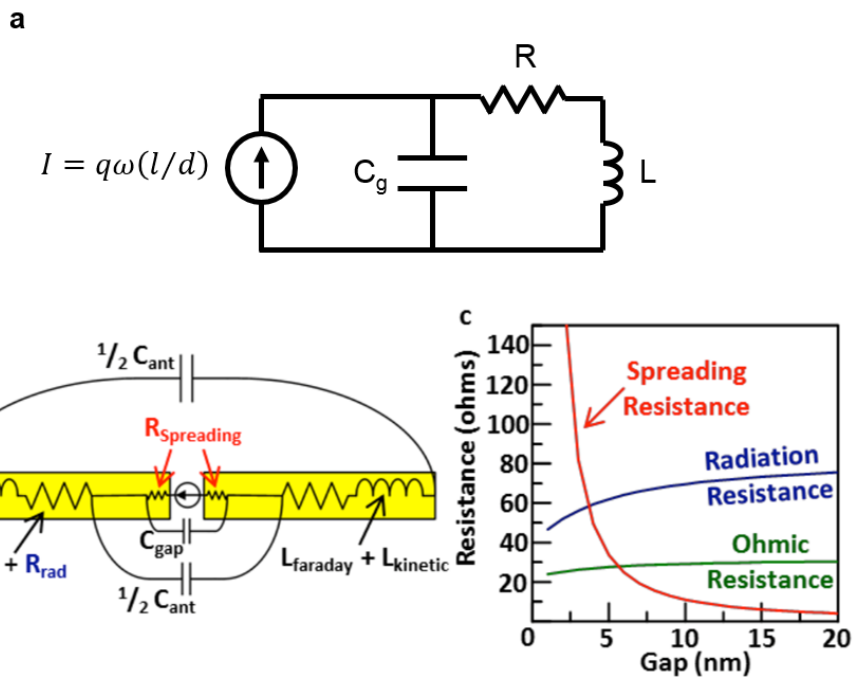

Figure 5. a) Simplified circuit model for antenna to compare with Purcell factor. b) Circuit model of dipole antenna. c) Plot of resistances versus gap width. At small gap width, spreading resistance takes over and reduces efficiency. (b), (c) reproduced from [23].

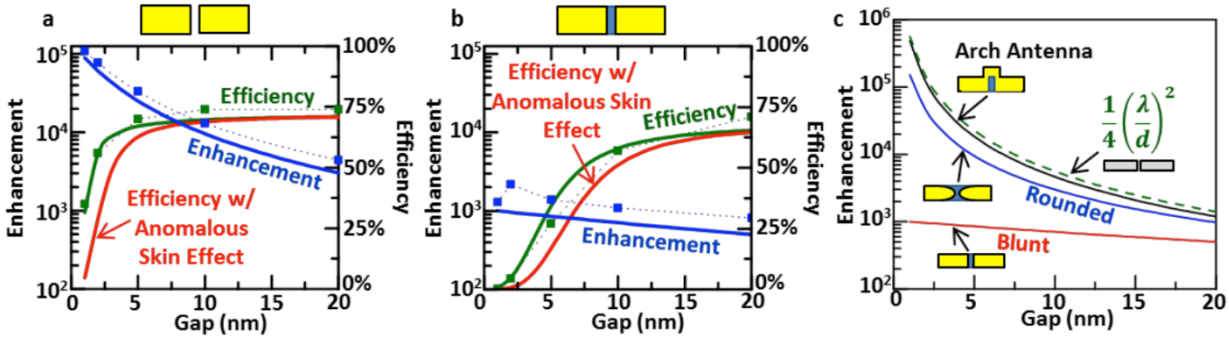

Figure 6. Efficiency and enhancement from circuit model and FDTD simulation. Solid lines: circuit model. Solid squares: FDTD simulation. a) Dipole with vacuum in gap. b) Dipole with high-index semiconductor in gap. c) Comparison of blunt, rounded, and arch antenna geometries. Reproduced from [23].

From Fig. 6, we see that for dipole antennas with gaps of ~5-20 nm, we can achieve >50% efficiency, with enhancements of $>10^4$ for vacuum in the gap, and $\sim 10^3$ with high-index semiconductor. The enhancement is lower for semiconductor in the gap due to increased gap capacitance, which acts as a shunt path for the current. One way to remedy this is by making the antenna tips rounded, decreasing capacitance. Another way is to add an inductor in parallel to

form an LC matching network, increasing the impedance of this shunt path. This can easily be done using an arch dipole with metal connecting the two antenna arms. Both approaches restore high enhancement similar to the vacuum gap (Fig. 6c).

Also note that at gaps <10 nm, although enhancement continues increasing, efficiency drops sharply due to spreading resistance. This is because the effective contact area of the atomic dipole emitter decreases as it is brought closer to the metal surface, increasing resistance. Thus, the optimal gap width for this design to obtain good efficiency and reasonably high enhancement is ~10-20 nm.

1.3.3 Practical challenges

Although we have shown that peak enhancement can be extremely high (>1000x) with good efficiency (>50%) limited by metal loss, real devices face many other challenges to achieving such high speed and efficiency. The model above was for a single dipole placed in the optimal location with the optimal polarization, emitting at a single frequency. A real semiconductor consists of randomly placed emitters, with random polarization, and typically broadband emission (> 2kT linewidth). We will investigate the effect of each of these in turn.

Positioning of the emitter can be accounted for by defining a spatially-dependent enhancement $F(\vec{x})$, using FDTD simulation of dipoles in different locations, or an appropriate circuit model. It is also possible to find the approximate enhancement in a single simulation by looking at the mode profile induced at the antenna by a plane wave, assuming the antenna radiates mainly in that direction. The Lorentz reciprocity theorem states that [20]:

$$\int E_1 \cdot J_2 \, dV = \int E_2 \cdot J_1 \, dV \tag{19}$$

where E_1 is the field produced by the current source J_1 and E_2 is the field produced by the source J_2. As shown in Fig. 7, if we take J_1 as the current source for the antenna and J_2 as a current source in the far field with the correct polarization, the enhancement is proportional to $|E_2|^2$. If J_1 is moved to a non-optimal location, the far field E_1 will drop, and therefore so will the received field E_2 at that location. As an example, a cavity-backed slot antenna (Fig. 8a) has a mode profile along the length of the slot $|E|^2 \propto \cos^2(\pi x/l_{eff})$. The effective slot length l_{eff} is slightly longer than the physical length (Fig. 8c), due to the field extending into the metal.

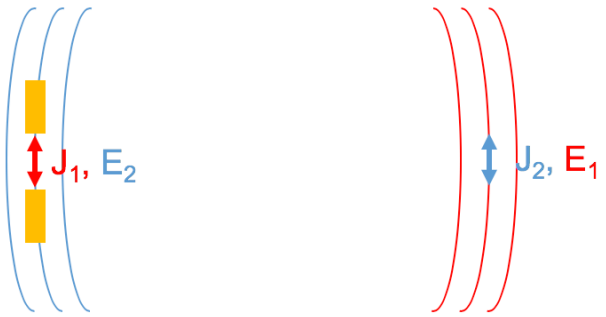

$$F \propto P_{rad} \propto |E_1|^2 \cong |E_2|^2 \left(\frac{J_1}{J_2}\right)$$

Figure 7. Lorentz reciprocity for two current sources J_1 and J_2.

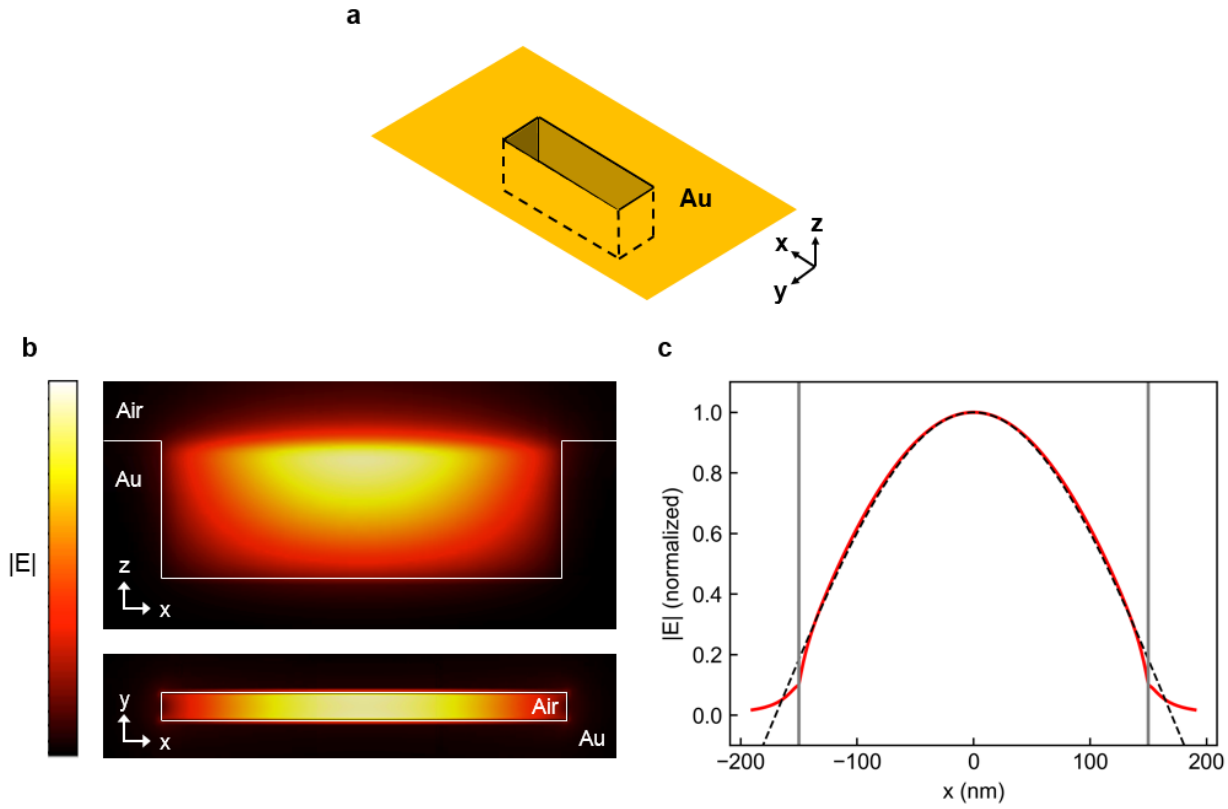

Figure 8. a) Schematic of simulated cavity-backed slot antenna. b) Simulated electric field profile for a cavity-backed slot antenna under normal plane-wave excitation, in the x-z and x-y planes. The slot length (along x) is 300 nm and slot depth (along z) is 100 nm. c) Cross section of normalized |E| across the length of the slot. Red solid line: simulation. Black dashed line: fitting to sinusoid. Grey lines denote boundary between metal and air.

To account for polarization, recall Fermi's Golden Rule, written here for band-to-band transitions in a semiconductor [17]:

$$\Gamma = \frac{2\pi}{\hbar}|\langle c|H'|v\rangle|^2 \rho_{op}(E, \hat{e}) \tag{20}$$

$$H' = qE_0 \hat{e} \cdot \vec{r} \tag{21}$$

where $|c\rangle$ and $|v\rangle$ are the conduction and valence band wavefunctions. For a bulk material, the dipole matrix element $\vec{r}_{cv} \equiv \langle c|\vec{r}|v\rangle$ may point in any direction. Thus, for a given polarization $\hat{e}$, we must average over direction, giving a factor of

$$\frac{\int d\Omega \cos^2(\theta)}{\int d\Omega} = \frac{1}{3} \tag{22}$$

compared to an optimally aligned dipole. This essentially cancels out the factor of 3 in the Purcell factor, since the other two polarizations can couple to free-space modes but not to the cavity mode. Similarly, if the dipole is mainly oriented in a plane, such as in monolayer materials or for the conduction-heavy hole (C-HH) transition in III-V quantum wells [1], we obtain a factor of ½. This is one motivation to move to lower-dimensional materials.

Now let us consider the effect of a finite linewidth of the emitter. This can be written as a spectrally-averaged Purcell factor, assuming the carrier populations are in thermal equilibrium at all times. The total spontaneous emission rate is [17]:

$$R_{sp} = \int C_0(E)\rho_{el}(E)f_2(E)\big(1 - f_1(E)\big)\rho_{op}(E)dE \tag{23}$$

where E is the photon energy, $\rho_{el}(E)$ is the reduced electronic density of states, $f_1(E)$ and $f_2(E)$ are the Fermi distribution functions for valence and conduction band respectively, $\rho_{op}(E)$ is the optical density of states, and C_0 is an overall constant that is weakly dependent on energy compared to the other terms. We obtain for the overall enhancement:

$$F_{avg} \equiv \frac{R_{sp,cav}}{R_{sp,fs}} = \frac{\int C_0(E)\rho_{el}(E)f_2(E)\big(1 - f_1(E)\big)F(E)\rho_{fs}(E)dE}{\int C_0(E)\rho_{el}(E)f_2(E)\big(1 - f_1(E)\big)\rho_{fs}(E)dE} \tag{24}$$

where $F(E)$ is the enhancement spectrum, and $\rho_{fs}(E)$ is the free space optical density of states. We can write the integrand in the denominator as the "intrinsic" spontaneous emission spectrum and obtain:

(25)

$$F_{avg} = \frac{\int R_0(E)F(E)dE}{\int R_0(E)dE}$$

$$R_0(E) \equiv C_0(E)\rho_{el}(E)f_2(E)\big(1 - f_1(E)\big)\rho_{fs}(E) \tag{26}$$

The emission spectrum in semiconductors is usually not an ideal Gaussian or Lorentzian lineshape, due to the thermal distribution of carriers and various broadening mechanisms. However, to ease computation and extract general trends, we will assume both $R_0(E)$ and $F(E)$ are Lorentzian, and centered on the same energy E_0:

$$R_0(E) = \frac{\Delta E_s}{2\pi}\frac{1}{(E - E_0)^2 + (\Delta E_s/2)^2} \tag{32}$$

$$F(E) = F_0\frac{(\Delta E_c)^2}{4}\frac{1}{(E - E_0)^2 + (\Delta E_c/2)^2} \tag{33}$$

where ΔE_s and ΔE_c are the intrinsic and cavity linewidths respectively, and F_0 is the peak enhancement. R_0 is normalized so that $\int R_0(E)dE = 1$. F_{avg} is then simply:

$$F_{avg} = F_0\frac{\Delta E_c}{\Delta E_s + \Delta E_c} \tag{34}$$
(27)

We see that if $\Delta E_s \ll \Delta E_c$, the average enhancement is indeed F_0. We can also write this in terms of the cavity Q factor $Q_c = E_0/\Delta E_c$ and intrinsic Q factor $Q_s = E_0/\Delta E_s$:
(28)

$$F_{avg} = \frac{3}{4\pi^2}\left(\frac{\lambda}{n}\right)^3\frac{1}{V}\frac{Q_cQ_s}{Q_c + Q_s} \tag{35}$$

where we used the expression for the Purcell factor above. For a fixed Q_s, F_{avg} saturates at

(29)
$$F_{avg,max} = \frac{3}{4\pi^2}\left(\frac{\lambda}{n}\right)^3\frac{Q_s}{V} \tag{36}$$

as $Q_c \to \infty$ [24]. Thus, for a broadband emitter and a single-mode cavity, there is little reason to use a cavity Q much higher than $\sim Q_s$. Taking the emission width as $\Delta E_s \cong 2kT = 51\ meV$ and $E_0 \cong 1\ eV$, this gives $Q_s \cong 20$. Fig. 9 plots the spectrally-averaged enhancement versus Q_c, for various Q_s, assuming $V_{eff} = 10^{-3}(\lambda/n)^3$. We see that using a more narrowband emitter is (30)
desirable to increase the average enhancement. This provides another motivation to move away from bulk semiconductors with their broad density of states, to quantum-confined active

(31)

materials or atomic/molecular systems with discrete energy levels. We will now consider the choice of active material in more detail.

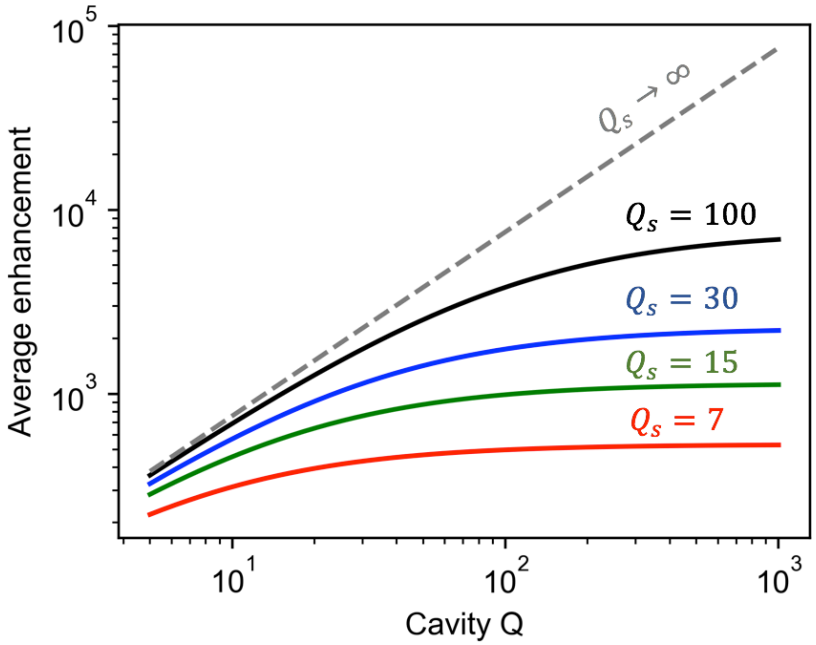

Figure 9. Spectrally-averaged enhancement versus cavity Q, for various Q_s, and $V_{eff} = 10^{-3}(\lambda/n)^3$.

1.4 Choice of active material

Many active materials have been used to achieve high Purcell enhancement, including molecules [25–27], III-V bulk ridges, quantum wells, and quantum dots [28–30], colloidal quantum dots [31], nanocrystals [32], and monolayer materials [33–36]. Molecular approaches are generally difficult to electrically inject, which is required for a practical LED. Colloidal quantum dot LEDs have shown high internal quantum efficiencies ~90% under electrical injection [37], although they appear to be relatively unexplored for optical communication applications. Their low conductivity and mobility [38] may limit the device modulation speed and maximum current density.

III-Vs are the most commonly used option for communications, and their material properties and processing technology are well understood. However, one disadvantage is their high rate of non-radiative recombination due to dangling bonds at the surface. This is characterized by the surface recombination velocity (SRV), which reaches ~10^4-10^6 cm/s for InP [39] and ~10^6 cm/s for GaAs even with oxide passivation [40]. For comparison, Si has shown extremely low SRV <10 cm/s [41, 42]. Sulfur-based chemical treatments have been shown to reduce the SRV to <10^3

cm/s in GaAs [43], but these are challenging to incorporate into a nanoLED process. High surface recombination competes with radiative recombination and can drastically reduce the device efficiency at small surface-to-volume ratios. For example, for a ridge 20 nm wide in its smallest dimension, the non-radiative lifetime is

$$\tau_{nr} \cong \frac{d}{2v_s} = 10\ ps \tag{37}$$

for a surface recombination velocity $v_s = 10^5$ cm/s. If the SRV can be made low (10^3 – 10^4 cm/s) or enhancement is sufficiently high, good efficiency can still be achieved [44].

Another promising approach is given by monolayer transition-metal dichalcogenides (TMDCs), a recently discovered material system with many novel physical properties. In particular, they are intrinsically nanoscale in one dimension, and their pristine surfaces contain no dangling bonds, leading to high optical quantum yield. We will discuss TMDCs and their use in optical antenna-coupled nanoLEDs further in Chapter 3 and the remainder of this work.

2 Helium ion milling of slot antennas

Achieving high enhancement requires fabricating small antenna gap widths <30 nm, a challenging task. The most common fabrication method is electron-beam lithography (EBL), in which a high-energy (~20-100 keV) electron beam is focused onto a resist layer, followed by resist development and either liftoff or etching to transfer the pattern underneath. Electrons have a much smaller effective wavelength ($\lambda = h/mv \cong 0.004 - 0.01\ nm$) than photons, allowing feature sizes <20 nm to be produced. However, edge roughness from the resist and metal deposition/etching, as well as poor dose repeatability, degrade performance at small scales.

In this chapter, we investigate helium-ion milling (HIM) as an alternative, high-resolution method for creating optical slot antennas. Helium ions are more massive than electrons (4 u vs. 0.0005 u), leading to even smaller effective wavelength. In addition, the interaction volume with the sample can also be much smaller compared to electrons due to lower backscattering [45] (Fig. 10).

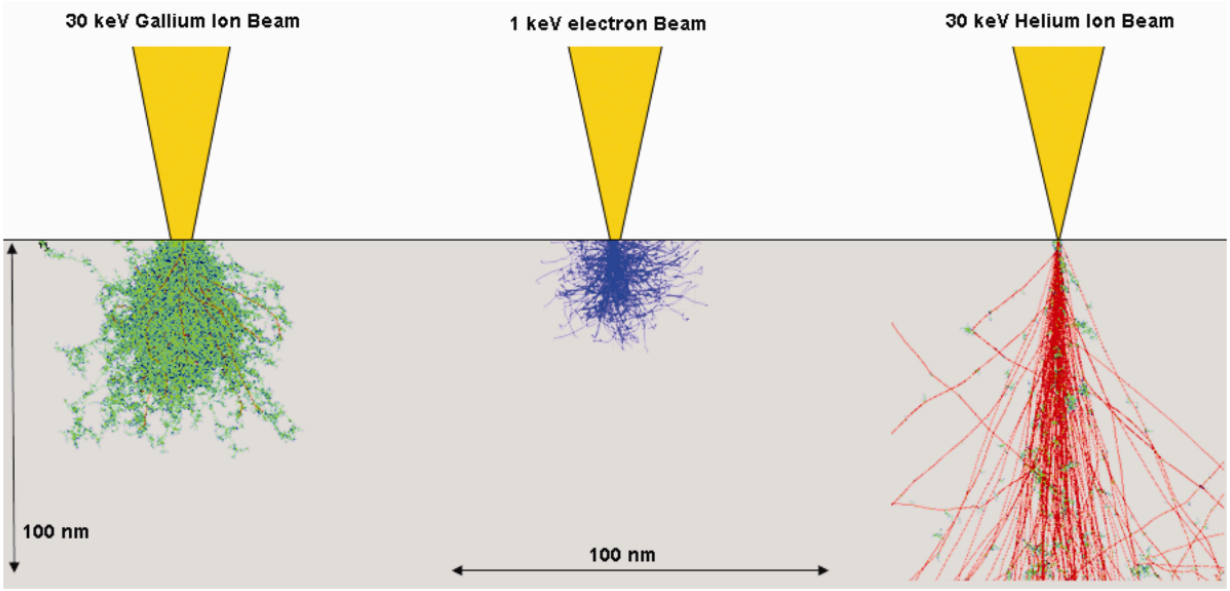

Figure 10. Monte Carlo plots showing scattering of various particles in a Si substrate. Reproduced from [45].

Past work with HIM has focused on dipole antennas using a combination of EBL and HIM to create the gaps [4,5]. Extremely small gap widths <5 nm have been achieved (Fig. 11) [46, 47]. In practice, slot antennas are more attractive for optoelectronic devices due to easier electrical injection and higher enhancement compared to dipole antennas with similar dimensions [2,3]. He-ion milling is similar to gallium focused-ion beam milling (Ga-FIB), in that the unwanted material is directly sputtered away instead of patterned using lithography followed by etching or

liftoff. HIM allows for higher resolution that Ga-FIB, due to the larger probe size of the liquid-metal Ga-ion source versus the atomic He-ion source, and the larger interaction volume of the Ga ions with the specimen (Fig. 10). We demonstrate HIM slot antennas with controllable 20 nm gaps, which show extremely high polarization ratios and resonance shifts with antenna length. As shown above, gaps much smaller than ~20 nm tend to suffer from low antenna efficiency due to spreading resistance, despite high rate enhancement. In addition, we compare the optical quality of He- and Ga- milled antennas with larger gap widths.

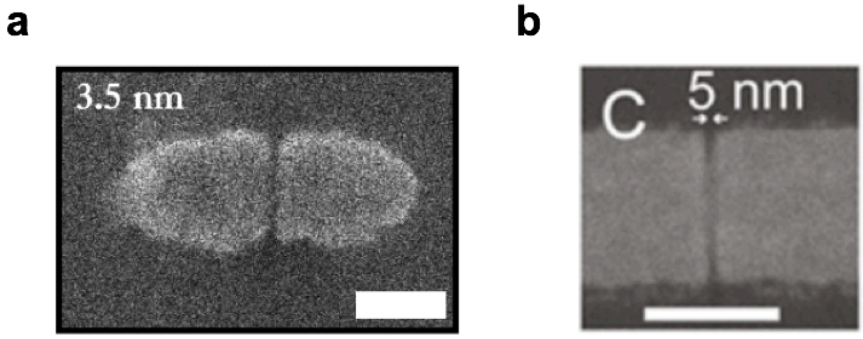

Figure 11. Dipole antennas fabricated using a combination of EBL and HIM to form the gaps. Scale bar is 50 nm for a) and 100 nm for b). Reproduced from [46, 47].

2.1 Antenna design and fabrication

Fig. 12a shows a schematic of our antenna design. Slot antennas are milled into 23 nm Au layer deposited on a Borofloat glass substrate using electron-beam evaporation. The slot width is 20 nm for HIM slots, while antenna length is varied between 70-150 nm. In addition, 35 nm wide slots are milled using HIM and Ga-FIB to compare antenna quality, as Ga-FIB was unable to achieve 20 nm widths after successive focusing steps. The relatively thin Au layer allows for faster milling times and minimizes redeposition of sputtered material inside the slot. HIM is performed using a Carl Zeiss ORION NanoFab He/Ne/Ga triple-beam ion microscope, while Ga-FIB is performed using an FEI Quanta dual-beam SEM/FIB. Fig. 12b,c show electric field profiles inside the slot for vertical and horizontal cross sections, respectively.

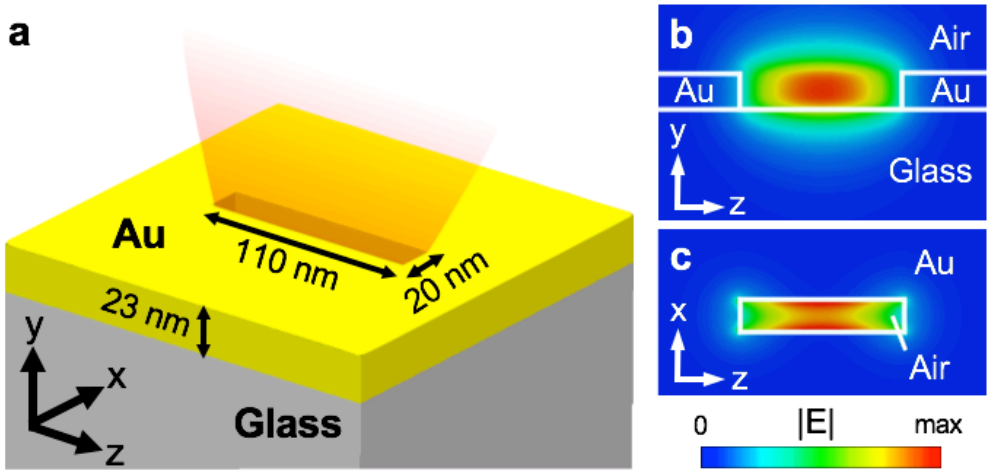

Figure 12. a) Antenna schematic showing substrate and light emission from slot. b, c) Simulated electric field inside the slot.

One of the main challenges with HIM is the tendency for He ions to collect in the substrate, which can cause substrate swelling and interfere with the sputtering process. In extreme cases, this can even cause large blisters to form in the substrate. Fig. 13 shows He ion milling results of 150 nm Au on Si using various doses. At low dose, there is no visible interaction with the substrate, while at higher doses, swelling and eventually blistering occurs. This can be avoided by choosing a substrate with higher He diffusion rate, such as glass in this work.

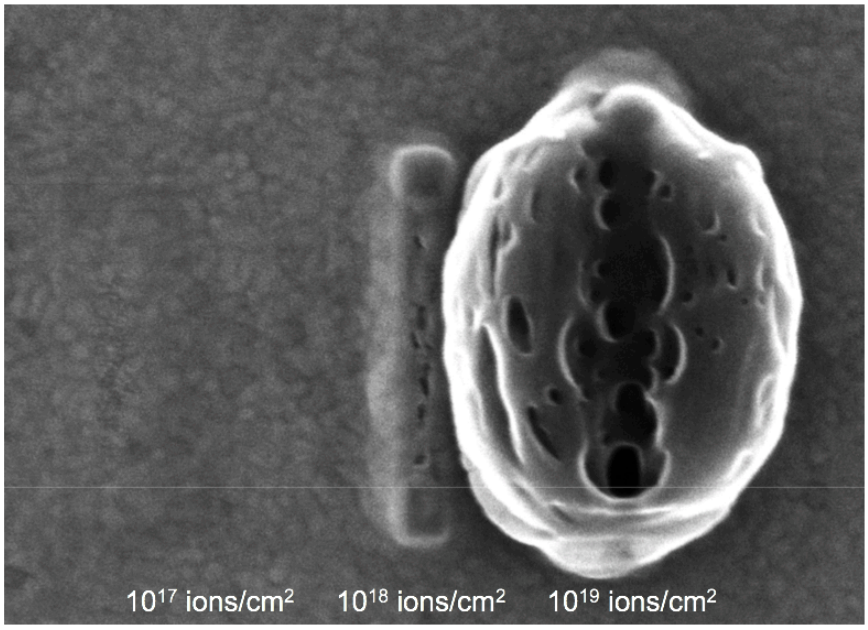

Figure 13. He ion milling results of 150 nm Au on Si, using various He ion doses shown.

Fig. 14a shows images of the milled 20 nm slots for various He ion doses. Fig. 14b shows a close up of the three doses. The antenna is observed to "shrink" as dose increases, most likely due to redeposition or He ion implantation. Fig. 14c compares the 20 nm HIM slot with the 35 nm HIM slot and 35 nm Ga-FIB slot. The 35 nm Ga-FIB slot exhibits rounded corners compared with the 35 nm HIM slot.

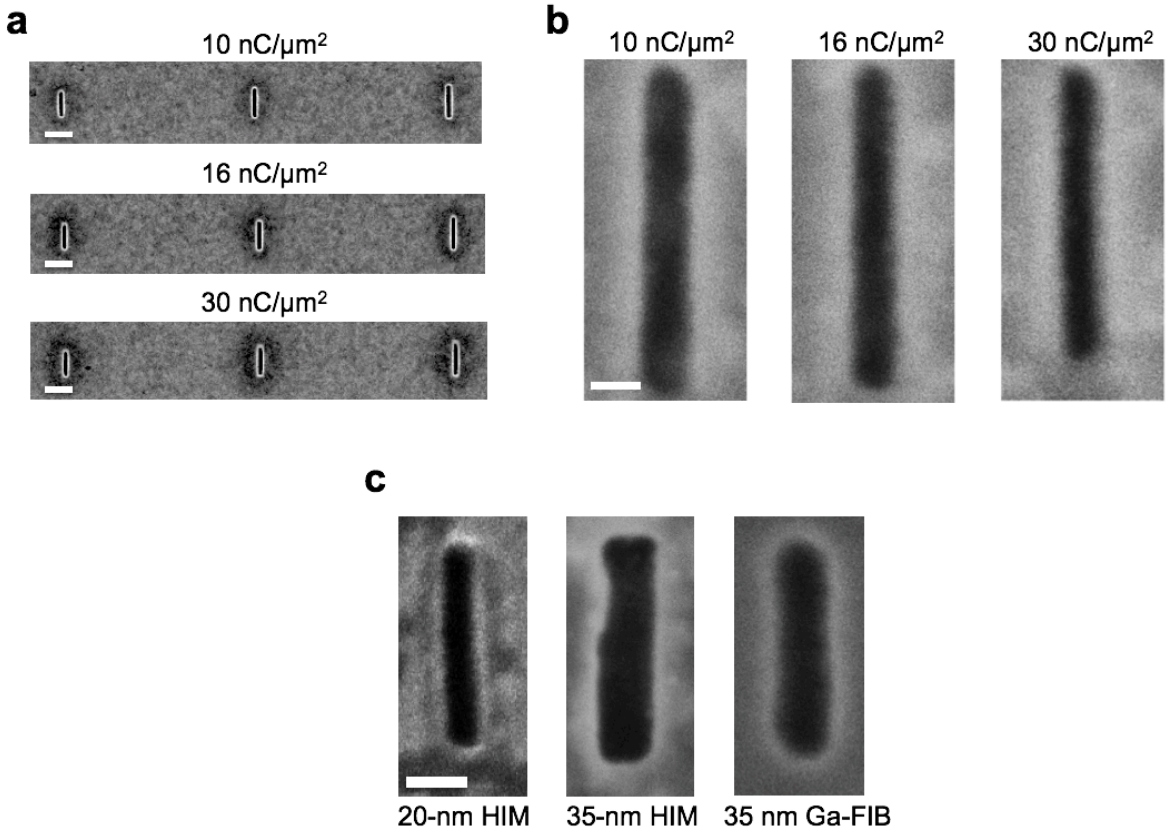

Figure 14. a) 20 nm HIM slots with various doses. Scale bar: 100 nm. b) Close up of the three doses. Scale bar: 20 nm. c) Comparison of 20 nm HIM, 35 nm HIM, and 35 nm Ga-FIB slots. Scale bar: 40 nm. Images of 20 nm HIM slots were taken with the helium-ion microscope, while 35 nm HIM and 35 nm Ga-FIB slot images were taken using a scanning electron microscope (SEM).

One drawback of milling techniques is that there is no simple way to determine the milled depth without damaging the sample. Due to the small dimensions, atomic force microscopy or optical methods are difficult. In our case, overetching partly into the glass substrate will cause a slight shift in the antenna resonance. Fig. 15 shows FDTD simulated resonances of 110 x 20 nm slots, for varying overetch depths. An overetch of 5 nm causes a ~20 nm blueshift in the resonance. The resonance shift saturates at ~50 nm for overetch depths of >20 nm, since the optical mode only extends a finite depth into the glass.

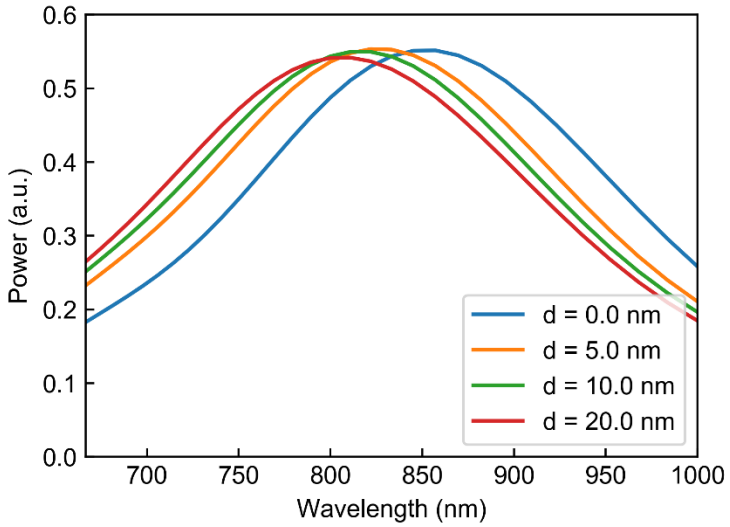

Figure 15. Simulated antenna resonances for varying overetch depth into the glass, of a 110 x 20 nm Au slot on glass.

2.2 Measurement results

Polarization-dependent scattering measurements were performed using a dark-field microscope setup. White light was focused onto the sample with a 100x objective, and the scattered light was filtered by a polarizer and collected in a grating spectrometer with a silicon CCD (Fig. 16). The polarization ratio between light scattered orthogonal to the slot versus parallel to the slot is related to antenna quality, since rough or uneven edges can cause excess scattering from the parallel polarization.

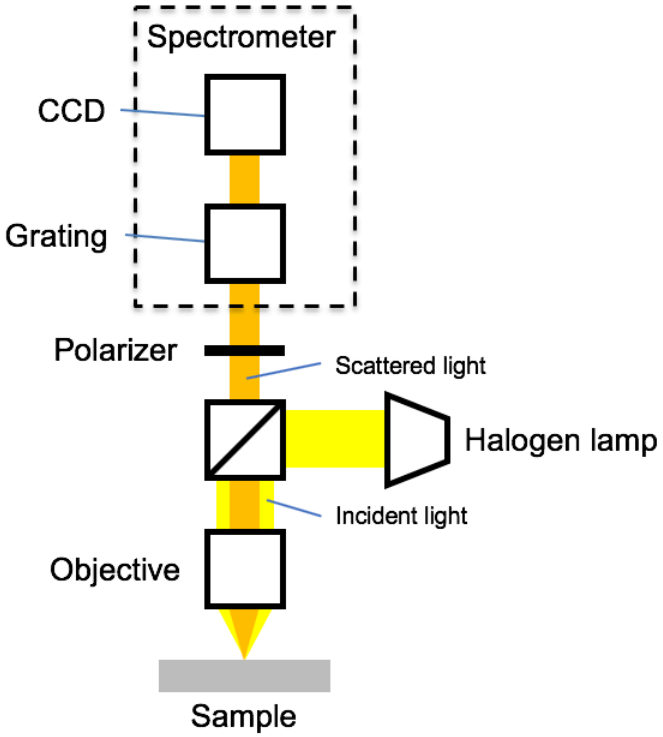

Figure 16. Schematic of dark-field scattering setup for measuring antenna resonance and polarization ratio.

Fig. 17a-c show scattering spectra of the orthogonal (antenna) polarization collected from the He- and Ga- milled antennas. Resonance shifts with length are observed for all three sets of antennas. Shorter antennas have a smaller scattering cross section, so the intensity decreases along with the length. All spectra were normalized by subtracting the background scattering from a nearby area on the sample, dividing by the measured spectrum of a uniform scatterer. In equation form:

$$S_{norm}(\lambda) = \frac{S_{ant}(\lambda) - S_{bg}(\lambda)}{S_{white}(\lambda) - S_{off}(\lambda)} \tag{38}$$

where $S_{norm}(\lambda)$ is the final normalized spectrum, $S_{ant}(\lambda)$ is the measured antenna spectrum, $S_{bg}(\lambda)$ is the background scattering, $S_{white}(\lambda)$ is the measured spectrum of a Lambertian scatterer, and $S_{off}(\lambda)$ is the measured spectrum with the lamp off, to eliminate the effect of dark counts. White paper was used here as the uniform scatterer here, as it exhibits near-Lambertian scattering. As shown in Fig. 17b,c insets, the maximum polarization ratio was about 17 for the 35-nm HIM slots and 15 for the Ga-FIB slots. Fig. 18 shows the scattering spectra of the 35 nm HIM and Ga-FIB slots at the two polarizations, for varying lengths.

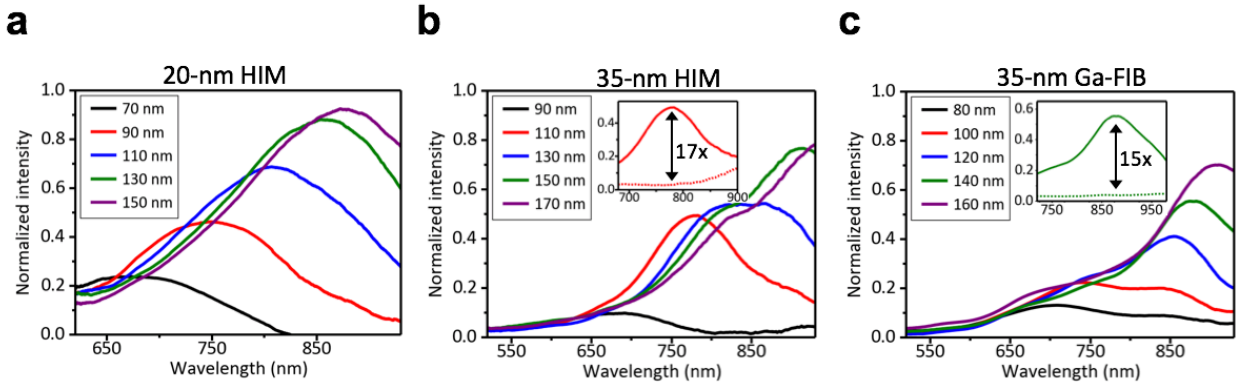

Figure 17. Normalized scattering intensity of antenna polarization, for all three antenna arrays. a) 20-nm HIM antennas. b) 35-nm HIM antennas. Inset: spectra for both polarizations of 110-nm length antenna. c) 35-nm Ga-FIB antennas. Inset: spectra for both polarizations of 140-nm length antenna.

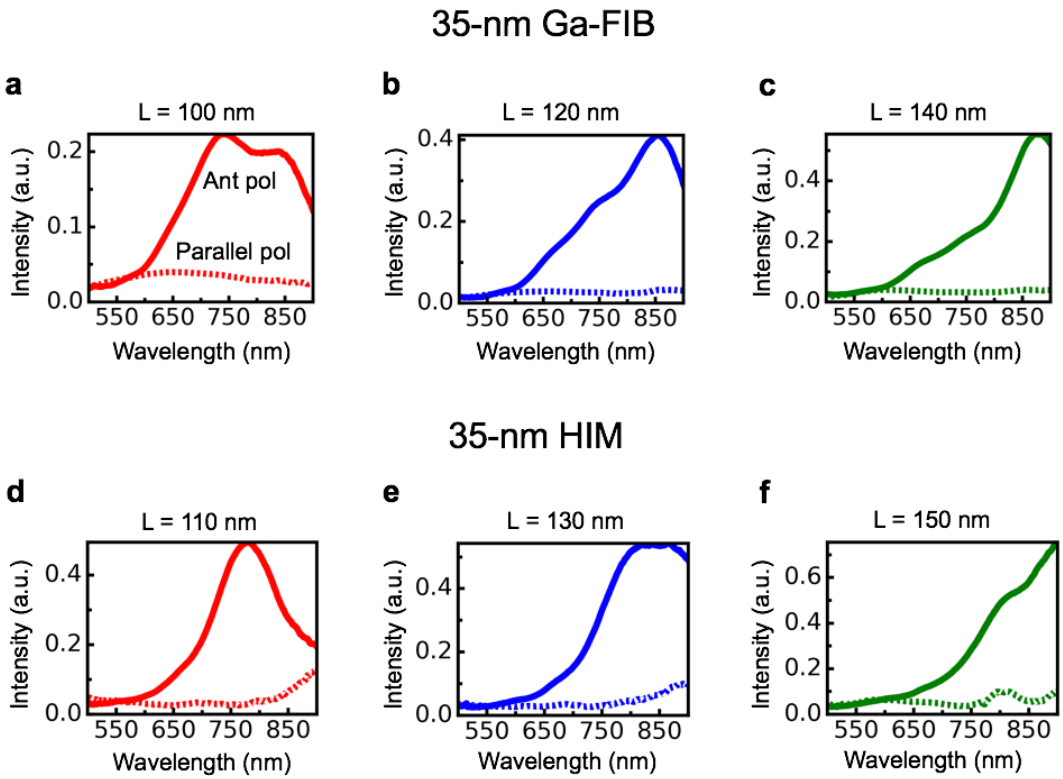

Figure 18. Scattering spectra for antenna polarization (solid curves) and polarization parallel to the slot (dotted curves), for 35 nm Ga-FIB (a-c) and HIM antennas (d-f) of varying lengths.

Fig. 19a-c show CCD images for all three antenna arrays at antenna (top) and parallel (bottom) polarizations. Scattering from the parallel polarization is visible in the CCD images for the 35-nm HIM and Ga-FIB antennas, but was extremely weak for the 20-nm HIM slots, making it

difficult to calculate polarization ratio using the spectra. By fitting a sine curve to the CCD spot intensity at different polarizer angles (Fig. 19d), we estimate a polarization ratio of ~37x.

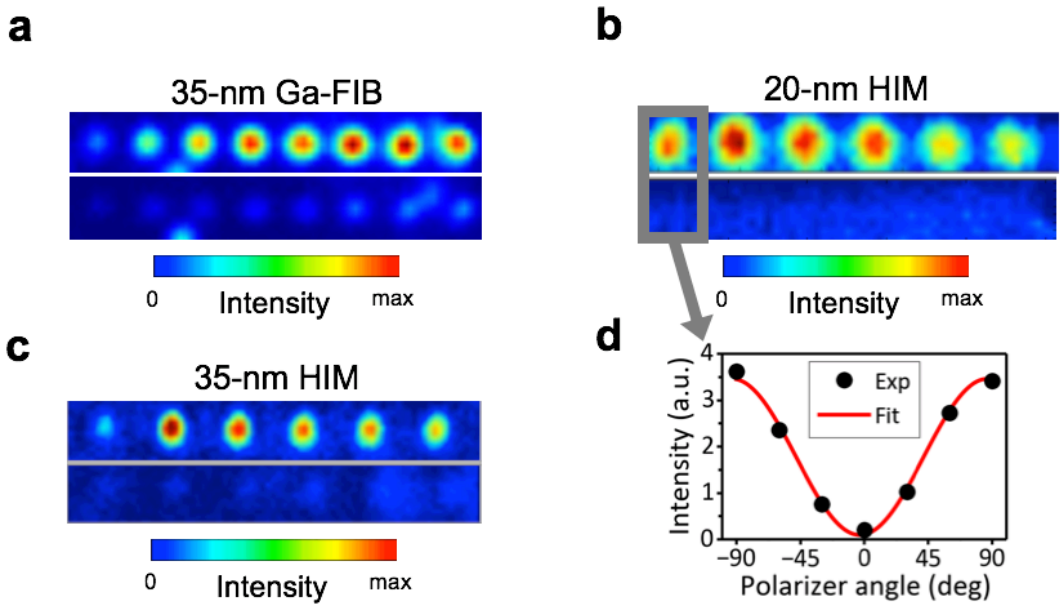

Figure 19. a-c) CCD images of all three antenna arrays for antenna polarization (top panels) and parallel polarization (bottom panels). d) Intensity of single antenna spot with varying polarizer angle.

Both HIM and Ga-FIB antennas show similar resonance wavelength to that predicted by simulation (Fig. 20). We observed a small uniform blue shift for 35-nm and 20-nm HIM antennas compared to simulation, likely due to slight milling into the substrate, as described above. The apparent blue shift for both sets of antennas above 900 nm is due to the detector cutoff.

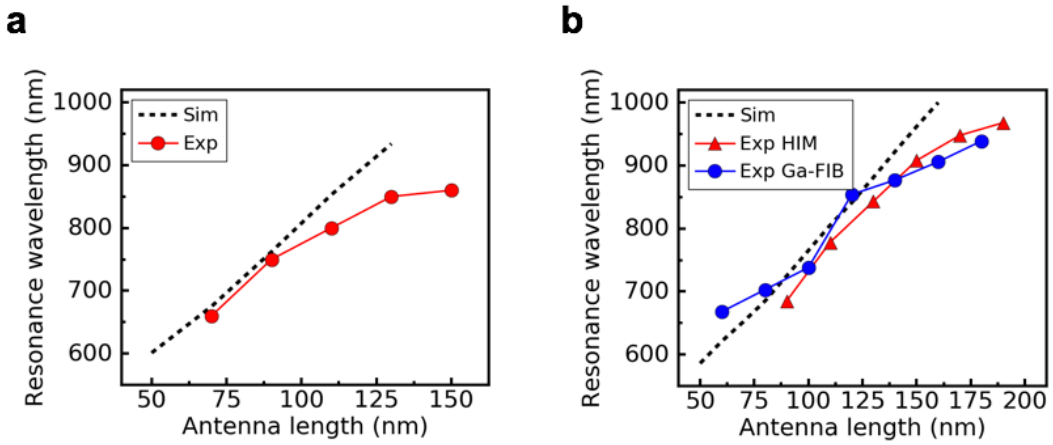

Figure 20. Measured and simulated antenna resonance wavelength vs antenna length, for 20 nm HIM (a) and 35 nm HIM and Ga-FIB (b).

Finally, we note that cavity-backed slot antennas may be preferred to the non-cavity-backed slots shown above, due to higher mode confinement, higher enhancement, and directional emission. However, as mentioned previously, milling depth is hard to control and hard to characterize without damaging the sample. One way to monitor the depth in-situ is with endpoint detection using two material layers with different secondary electron (SE) yield [48]. By monitoring the SE yield during the milling process, milling can stop when it reaches the second material. This requires two materials with significantly different SE yield. The two most common antenna metals, Au and Ag, have relatively similar SE yield at He ion energy of 30 keV (Fig. 21). On the other hand, Ti has a ~2.5x lower SE yield than Au and Ag, so it may be an effective endpoint monitor. In a cavity-backed slot, the electric field at the bottom of the slot is relatively small (Fig. 8a), so loss of antenna efficiency can be minimized if Ti is used as the bottom layer, or integrated as the middle layer in a trilayer stack. Fig. 22 shows preliminary results of He ion milling on a trilayer stack of Au/Ti/Ag. We use a milling area of 100x100 nm^2 and monitor the total integrated image intensity within the milling area over time. We observe an initial decrease of image intensity caused by shadowing as the gold is milled away, followed by an increase in intensity, and finally another decrease. This suggests that the endpoint detection is working as intended, although further work is needed to confirm milling depth.

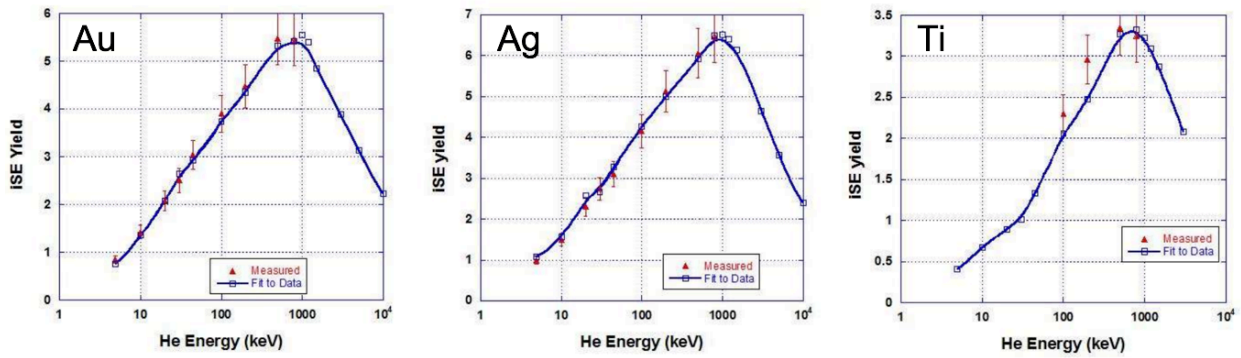

Figure 21. Secondary electron yield vs. He ion energy, for Au, Ag, and Ti. Reproduced from [49].

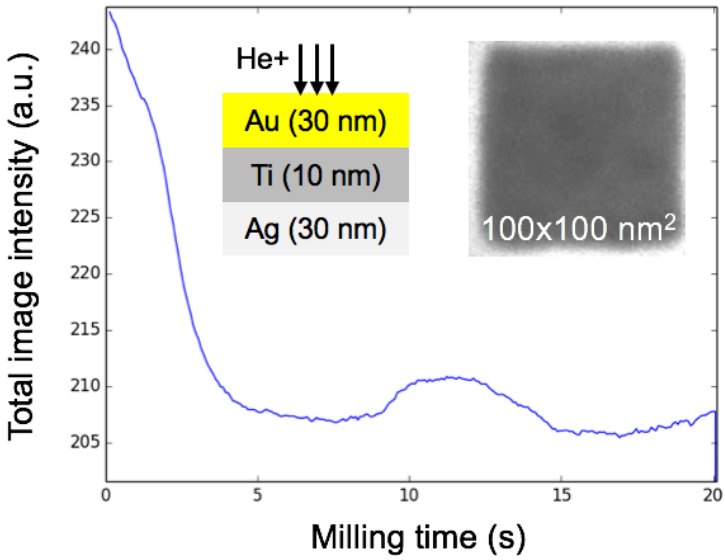

Figure 22. Integrated image intensity in milling area vs milling time, for trilayer stack of Au/Ti/Ag. Left inset: schematic of substrate. Right inset: Secondary electron image during the milling process.

In conclusion, helium-ion milling is a promising fabrication technique to produce nanoscale structures with ultimate resolution limit smaller than e-beam lithography and other types of focused-ion beam. Our results show that HIM is capable of producing high quality slot antennas with smaller gap widths than Ga-FIB and very large polarization ratios of ~37x. Wider HIM antennas exhibit similar polarization ratios and resonance wavelength behavior to their Ga-FIB counterparts. For producing cavity-backed slot antennas, endpoint detection may be an effective way to control slot depth. Some drawbacks of HIM include the redeposition of sputtered material when milling depth is large or dose is too high, the swelling of certain substrates due to He implantation, and the low throughput compared to Ga ion milling.

3 Transition metal dichalcogenide monolayers

As mentioned in Chapter 1, one challenge of traditional III-Vs nanoLEDs is their large surface recombination velocity, which leads to high non-radiative recombination and low efficiency as the device size decreases. This motivates the switch to lower dimensional materials where at least one dimension is intrinsically nanoscale, with chemically pristine surfaces lacking dangling bonds. In the rest of this work, we focus on the monolayer transition metal dichalcogenides and their use in nanoLEDs. This chapter will review past work on TMDCs and discuss the relevant carrier dynamics for high-speed modulation.

Transition metal dichalcogenides are a class of layered materials formed from one transition metal atom (W, Mo, etc.) and two chalcogen atoms (S, Se, or Te). Like graphite, they occur naturally as single-molecule layers loosely bonded by van der Waals interactions. A schematic of the layer structure of MoS_2 is shown in Fig. 23.

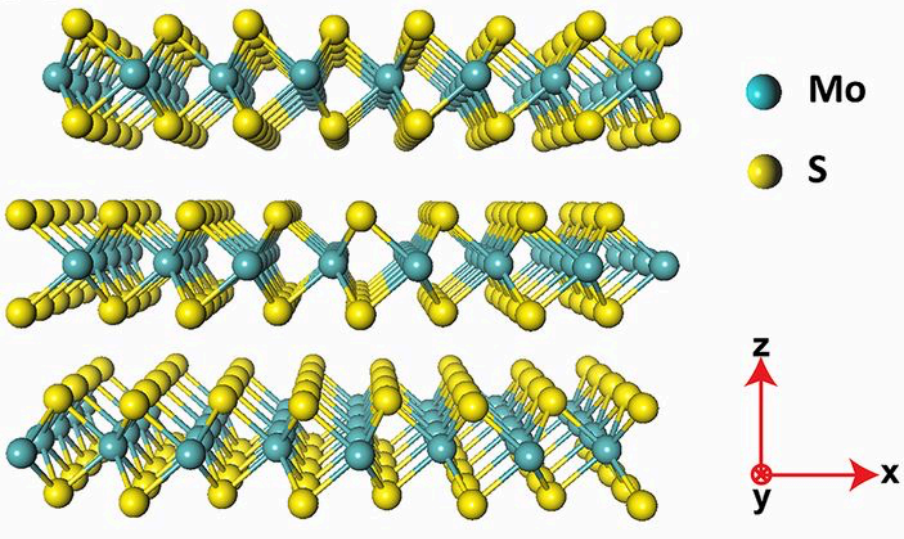

Figure 23. Layer structure of MoS_2, a commonly-studied TMDC. Reproduced from [50].

When thinned down to a single layer, they exhibit a dramatic change in optical and electronic properties, including emergence of a direct band gap (typically 1 – 2 eV) and huge exciton binding energy, up to 100s of meV [51]. In contrast to bulk semiconductors, excitons dominate the optical properties of TMDCs even at room temperature. These tightly-bound excitons arise from the reduced dielectric screening and stronger spatial confinement in 2D compared to 3D [52]. Optical absorbance can reach >5% even for a single atomic layer, due to the strong excitonic light-matter interaction [53].

Since the discovery in 2010 [51] of the first monolayer TMDC, MoS_2, these materials have been intensely explored for electronic and optoelectronic applications, which we will review below. From a practical standpoint, monolayer TMDCs are easily produced through mechanical

exfoliation or chemical vapor deposition. They exhibit good air and chemical stability, and can be easily transferred onto arbitrary substrates and processed using traditional semiconductor fabrication methods.

3.1 Applications in electronics

For transistors, their monolayer nature results in good electrostatic control over the channel. However, several challenges remain. Experimental carrier mobility is usually low (<200 cm^2/Vs for MoS_2), thought to be limited by defects and interface scattering [54]. This is less important in nanoLEDs, where in fact high mobility may not be desired due to increased carrier overshoot or ballistic transport across a nanoscale device.

In addition, ohmic contacts, desired for any electrically-injected device, still prove difficult to achieve. The lack of dangling bonds on the surface can result in a weak chemical interaction between the metal and semiconductor, leading to a tunnel barrier and high contact resistance (Fig. 24a, b) [55]. Some metals are predicted to hybridize with the monolayer and form a "metallized" region (Fig. 24c, d). However, even in this case there exists a lateral Schottky barrier between the metallized region and the uncovered TMDC (Fig. 24d). The Schottky barrier is high for most contacts due to Fermi-level pinning [56]. Some approaches to improve contact resistance include chemical doping, plasma-induced doping, and use of low/high work function metals (for electron and hole injection respectively) [55, 57–60]. Note that these doping methods only work for one type of doping (P or N) at a time; integrating both types of doping of a single material in the same device is a significant processing challenge. Contact resistance is mainly important in nanoLEDs to reduce operating voltage and thus increase energy efficiency, which may be low even if quantum efficiency is high. However, doping may not be necessary for carrier confinement due to the extremely fast exciton formation time, as we will discuss later.

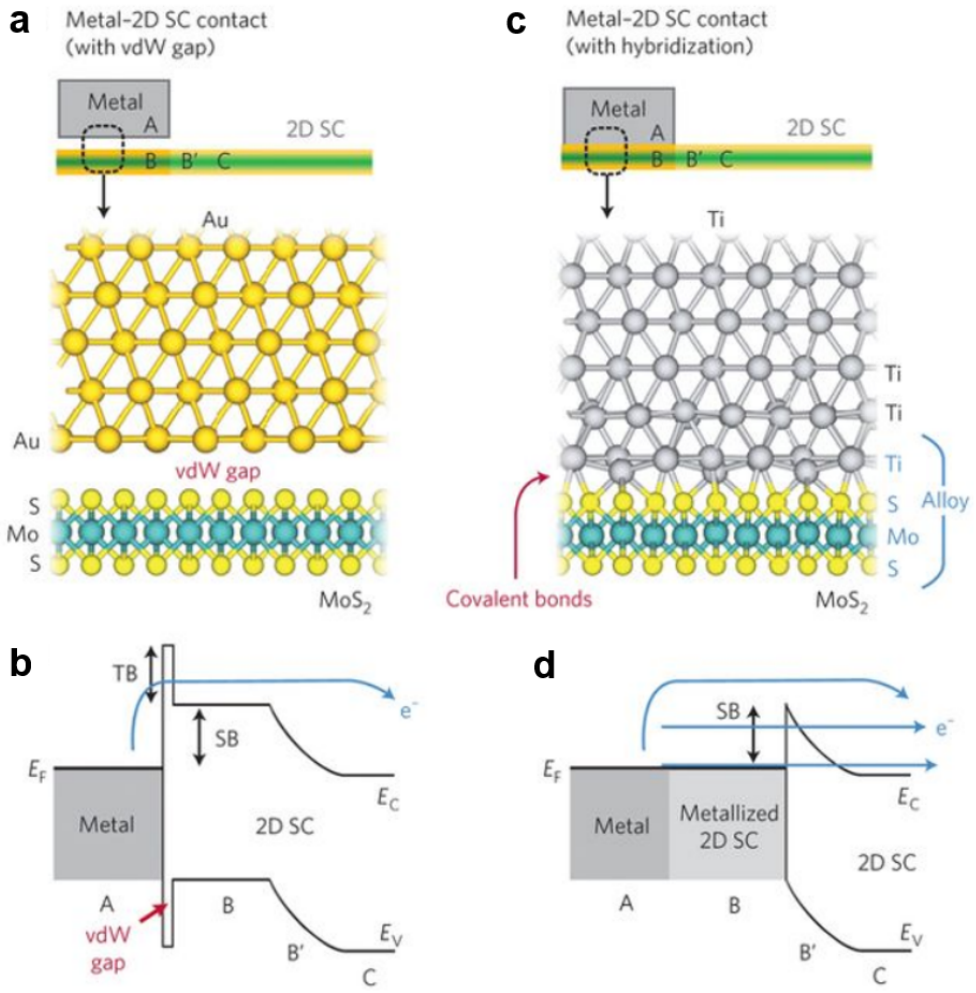

Figure 24. Metal-TMDC contact mechanisms. a) Schematic with van der Waals gap between metal and TMDC. b) Corresponding band diagram showing tunnel barrier (TB) and Schottky barrier (SB). c) Schematic with hybridization between metal and TMDC. d) Corresponding band diagram. Reproduced from [55].

Another long-recognized challenge in TMDC electronics is the large hysteresis in TMDC field-effect transistors (FETs). The cause of this hysteresis has been studied extensively, with some results pointing to charge trapping caused by adsorption of water and oxygen on the monolayer surface [61–63], and others to intrinsic defects [63, 64]. In lateral-junction LEDs, electrostatic gating is needed to form a P-N junction, and so the same problem is encountered, as we will show in the next chapter. In FETs, hysteresis manifests as a shift in the I_d-V_g curve as gate voltage is swept in opposite directions. At a constant gate bias, this is seen as a decay in current over time [61, 63]. Although past work on TMDC electroluminescence has shown high electroluminescence (EL) quantum efficiencies, these are reported only in high-vacuum conditions, where hysteresis is partially mitigated.

A simple alternative approach is pulsed voltage bias, which has been shown to yield hysteresis-free FET characteristics in ambient conditions [65–67] (Fig. 25), as well as bright electroluminescence using the LEC structure above. In the next chapter, we show that pulsed injection is also effective for lateral-junction TMDC LEDs, yielding stable EL from monolayer WSe_2 devices in ambient conditions.

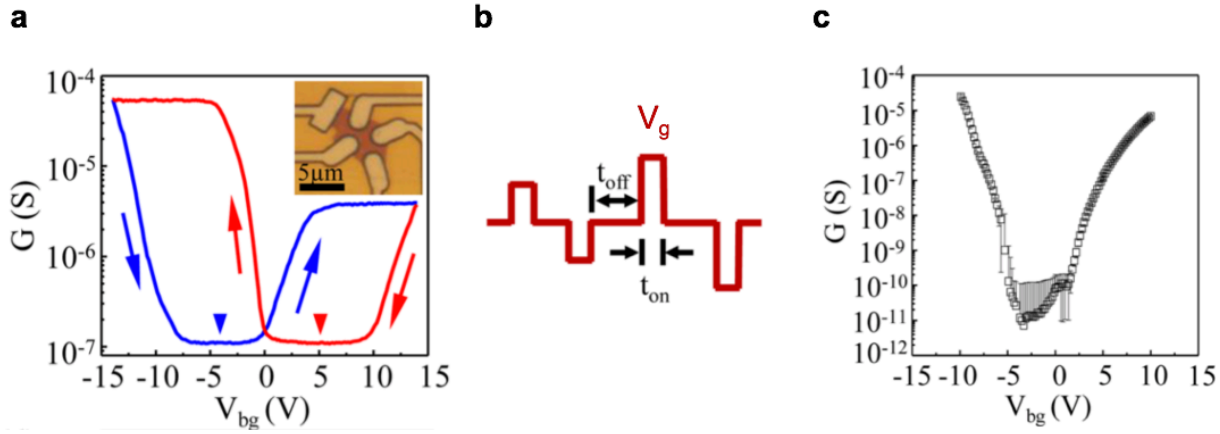

Figure 25. a) Conductance vs back gate voltage for WSe_2 FET, showing large hysteresis. b) Pulsing scheme for pulsed gate voltage sweep. c) Conductance vs back gate voltage using pulsed voltage, showing no hysteresis. Reproduced from [66].

3.2 Applications in optoelectronics

Due to their direct bandgap and novel excitonic physics, TMDCs are also attractive for optoelectronics. Various optoelectronic devices using TMDCs have been demonstrated, including LEDs, solar cells, and photodetectors [33, 68–79]. For nanoLEDs, the optical quantum yield (QY) is an important figure of merit, as this will ultimately limit the quantum efficiency (QE) of the device. The QY of unprocessed TMDCs is generally ~0.1-1% [80, 81] but can be raised to ~100% using a superacid treatment [81] (Fig. 26).

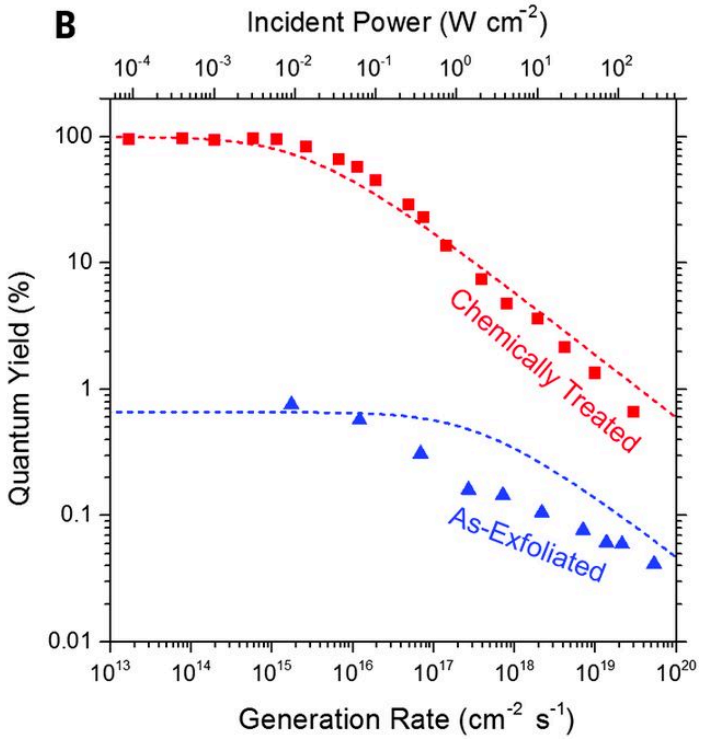

Figure 26. Quantum yield versus generation rate for as-exfoliated and superacid-treated MoS_2. Reproduced from [81].

3.2.1 Electrically-injected light-emitting devices

Electrically-injected TMDC LEDs in literature can be divided into two main types: lateral junction and vertical junction. Lateral junction LEDs were the first type demonstrated and the main focus of this work. In these devices, similar to TMDC field-effect transistors (FETs), the monolayer channel is formed laterally atop a gate dielectric, and gate voltage is used to electrostatically dope the channel P and N type near the two separate contacts (Fig. 27a). These have shown quantum efficiencies ranging from 0.01 – 1% [68–70]. More recently, vertical tunnel junction structures have also shown efficient light emission. In these structures, the TMDC is sandwiched between two tunnel barriers of hBN (~2 – 3 nm), and contacted on top and bottom by graphene electrodes (Fig. 27b). The tunnel barriers provide carrier and exciton confinement, and these structures have shown QEs of 1 – 5% [71, 82]. One disadvantage of this structure for electrical modulation is the high capacitance resulting from the very thin injection region (~5 nm), leading to large RC time.

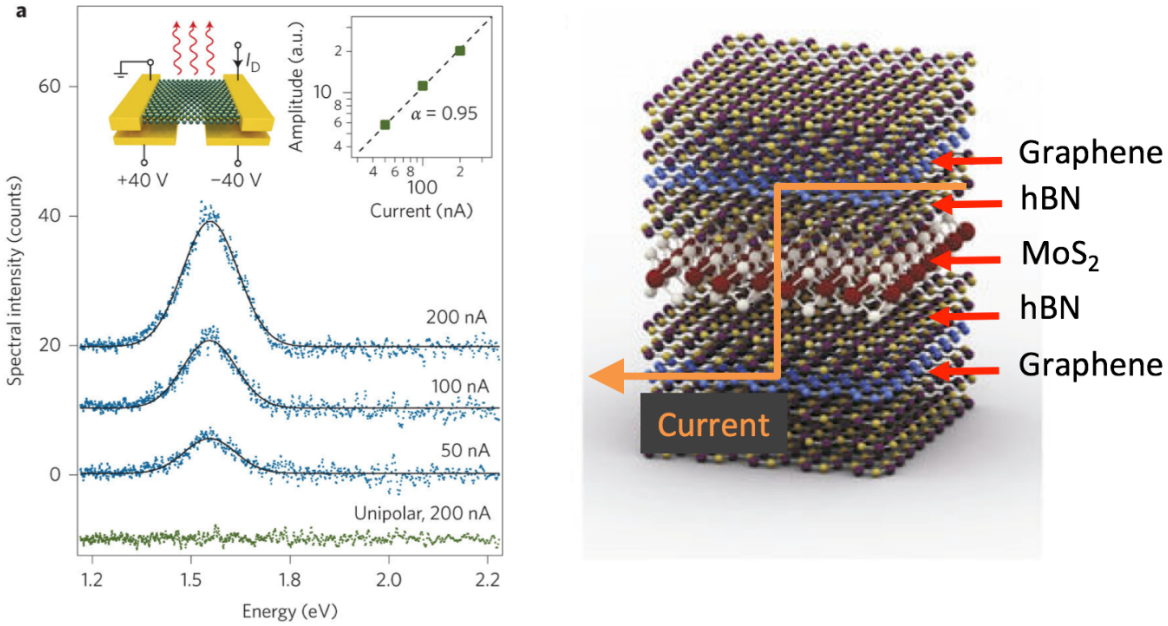

Figure 27. Left: schematic and electroluminescence spectra of lateral-junction LED. Separate voltages are applied to the split gates to electrostatically dope one side with holes and the other with electrons. Reproduced from [68]. Right: schematic of vertical-junction LED. Adapted from [71].

Recently, a new type of structure has also shown bright emission in TMDCs: the light-emitting capacitor (LEC) [83]. This device consists of a monolayer atop a gate oxide, contacted by a single contact (Fig. 28). By pulsing gate voltage between the two terminals, electrons and holes are injected in alternating cycles, and light is emitted near the contact. For efficient emission, the gate voltage must be pulsed quickly (ideally rise time of <~ns) to avoid carriers diffusing back into the contact before they can form excitons. Due to its ease of fabrication, and since it only requires one contact, this structure has been used for large-area (~mm) visible light emission with potential applications for displays [83].

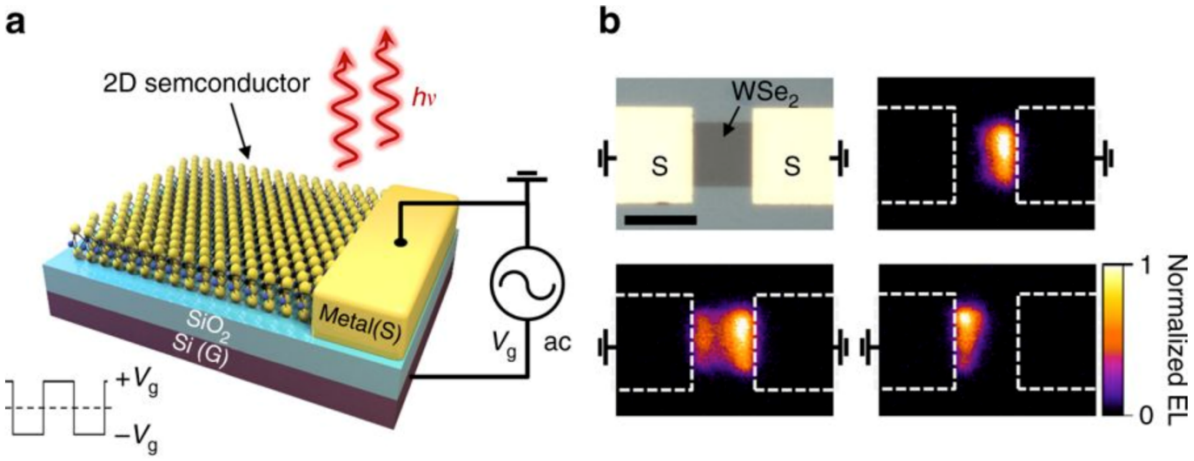

Figure 28. a) Schematic of light-emitting capacitor. b) EL image when one or both contacts are grounded while the gate is pulsed (the ungrounded contact is left floating). Reproduced from [83].

3.2.2 Optical cavity-coupled devices

There have been several reported demonstrations of TMDC monolayers coupled to optical cavities to enhance the light-matter interaction. Peak rate enhancements of >300x have been demonstrated using WSe_2 coupled to slot antennas [84]. Other examples include patch antennas, nanodisc arrays, and slot cavities [35, 36, 85]. Almost all of these devices are optically injected; to our knowledge, only one other demonstration has used electrical injection, with vertically-injected LEDs coupled to a photonic crystal cavity [33] (Fig. 29). This showed a relatively low enhancement of ~4x, and rise and fall times of ~400 ns, limited by the high capacitance of the vertical injection structure. We will discuss optical cavity coupling further in Chapters 5 and 6.

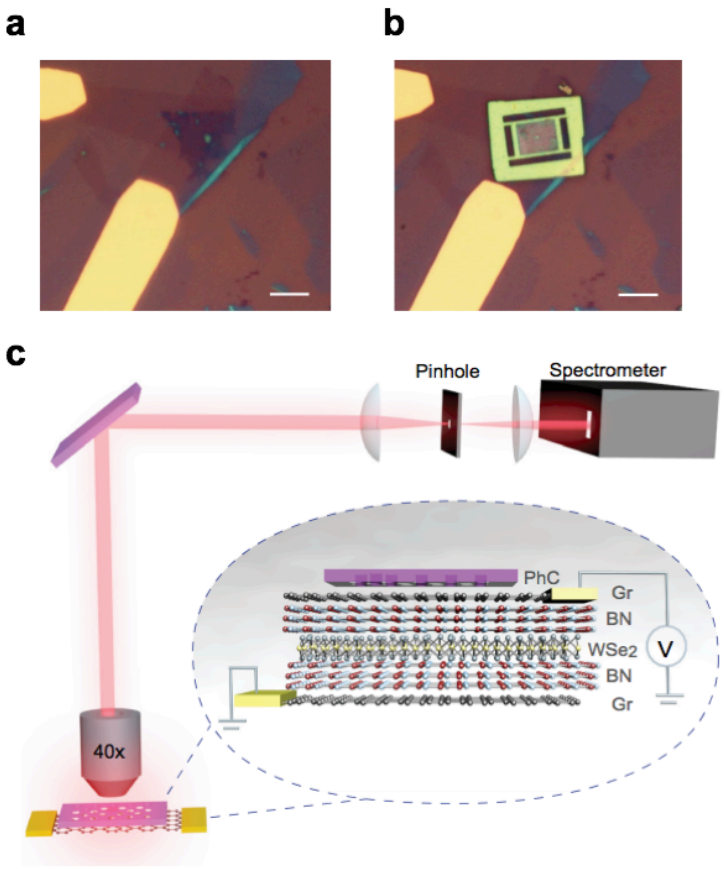

Figure 29. WSe_2 LED coupled to photonic crystal cavity. a) Optical image without cavity. b) Optical image with cavity. c) Schematic of device and measurement setup. Reproduced from [33].

3.3 Carrier and exciton dynamics

Now we discuss the carrier and exciton dynamics in TMDC monolayers, with an eye towards achieving high speed electrical modulation of light emission. Due to the high exciton binding energy, light emission in TMDC monolayers is dominated by excitons even at room temperature. Thus, to make a fast light emitting device, the exciton formation time as well as the exciton radiative lifetime must be made fast. Pump-probe studies show exciton formation time <1 ps for a variety of TMDCs and carrier densities [86–88]. For example, in [86], differential reflectance of a probe pulse with varying pump-probe delay is used as a sensitive measure of exciton and carrier density. A fast sub-ps delay in differential reflectance is observed at early times (Fig. 30a), which is attributed to exciton formation. Free carriers are more efficient than excitons at saturating the exciton oscillator strength [86], so differential reflectance drops as free carriers become excitons.

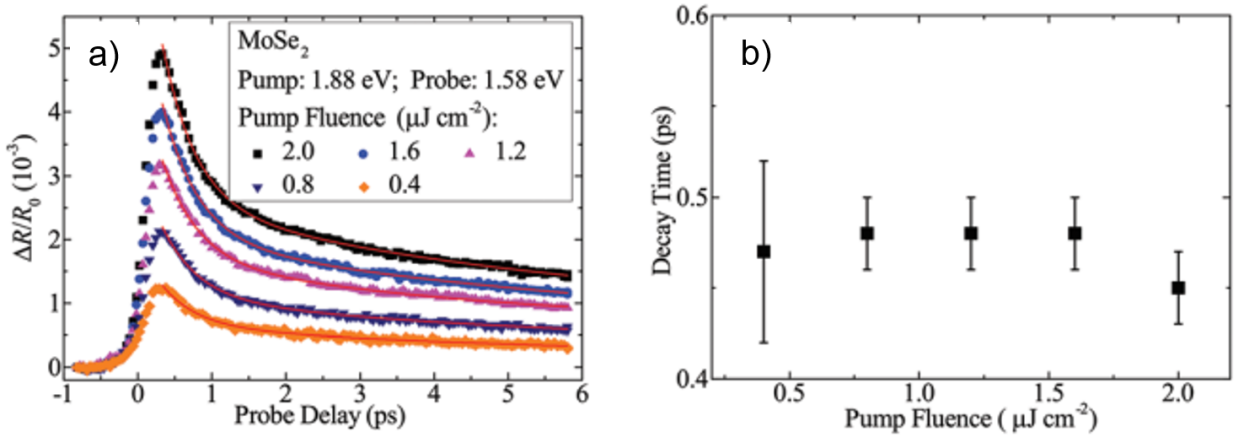

Figure 30. a) Differential reflectance $\Delta R/R_0$ versus probe delay for $MoSe_2$. b) Fast decay time versus pump fluence. Reproduced from [86].

Exciton formation in semiconductors can occur through two mechanisms [89]: (a) bimolecular ($B_{ex}n^2$) formation from electron and hole populations, or (b) direct (geminate) formation from an injected electron-hole pair through emission of longitudinal optical (LO) phonons [90], for which the rate is proportional to the injection density. Bimolecular formation has been observed in Si and the coefficient B_{ex} measured [91], while geminate formation has been observed in CdS [92]. For TMDCs, the constant decay time with respect to pump fluence in experiment suggests geminate formation [90]. In optical injection experiments, each photon creates a resonant electron-hole pair with matching momentum, which can then directly form an exciton. However, electrically injected carriers follow a thermal distribution, so we expect a bimolecular formation rate. The exciton formation coefficient B_{ex} has not been directly measured in experiment, although one report obtained a very high value ~10^4 cm^2/s in MoS_2 by fitting the photoluminescence (PL) quantum yield versus pump power to a rate equation model [81]. In III-V quantum wells, B_{ex} has been measured at low temperatures (2-10 K) to be ~5-15 cm^2/s [91, 93, 94]. Here, we adopt a conservative approach and derive it using the direct formation time τ_{ex}, in a similar manner as the standard derivation of spontaneous emission rate [17, 95]. We assume only electron-hole pairs with matching momentum can form an exciton, at the measured rate $1/\tau_{ex}$. We then sum over momentum states $k = (k_x, k_y)$, weighted by the electron and hole Fermi factors:

$$R = \frac{2}{\tau_{ex} A} \sum_k f(E_e - F_n)\left(1 - f\left(E_h - F_p\right)\right) \tag{39}$$

where R is the total exciton formation rate (cm^{-2} s^{-1}), A is the area of the crystal and $f(E)$ is the Fermi distribution function:

$$f(E) = \frac{1}{1 + e^{E/kT}} \tag{40}$$

and

$$E_e = E_c + \frac{\hbar^2 k^2}{2m_e^*} \tag{41}$$

$$E_h = E_v - \frac{\hbar^2 k^2}{2m_h^*} \tag{42}$$

The factor of 2 is for spin. Assuming a Boltzmann distribution for carriers:

$$\begin{aligned} n &= kT\rho_{2d}^{e} e^{(F_n - E_c)/kT} \\ p &= kT\rho_{2d}^{h} e^{(E_v - F_p)/kT} \end{aligned} \tag{43}$$

with the 2D density of states

$$\rho_{2D}^{e,h} = \frac{m_{e,h}^*}{\pi\hbar^2} \tag{44}$$

we arrive at the result:

$$R = \left(\frac{\pi\hbar^2}{kT(m_e^* + m_h^*)\tau_{ex}}\right) np \tag{45}$$

so the exciton formation coefficient is:

$$B_{ex} = \frac{\pi\hbar^2}{kT(m_e^* + m_h^*)\tau_{ex}} \tag{46}$$

This expression is very similar to the bulk (3D) radiative recombination coefficient $B_{rad,3D}$ [95]:

$$B_{rad,3D} = \frac{1}{2\tau_0}\left(\frac{2\pi\hbar^2}{kT(m_e^* + m_h^*)}\right)^{3/2} \tag{47}$$

where τ_0 is the lifetime from Fermi's golden rule. The 3/2 power arises for the bulk case. The $(m_e^* + m_h^*)$ in the denominator comes the Boltzmann distributions for electrons and holes contributing a factor of $1/\rho_{2d}^{e} \propto 1/m_e^*$ and $1/\rho_{2d}^{h} \propto 1/m_h^*$ respectively, while the integration over k gives a factor of reduced mass $m_r^* = (1/m_e^* + 1/m_h^*)^{-1}$, resulting in $m_r^*/m_e^* m_h^* = 1/(m_e^* + m_h^*)$. For $\tau_{ex} = 0.5$ ps, $m_e^* = m_h^* \cong 0.5\, m_0$ [96], we obtain $B_{ex} \cong 0.1$ cm^2/s at room temperature. This is a conservative estimate since we have neglected the interaction of electrons and holes with different momenta. We can compare this value to the radiative recombination coefficient of traditional semiconductors by multiplying by the monolayer thickness, to get $B_{ex,3D} \cong B_{ex} * 1\text{ nm} \cong 10^{-8}$ cm^3/s. In GaAs, the radiative recombination coefficient $B_{rad} \cong 10^{-10}$ cm^3/s. Thus, the effective exciton formation coefficient is much greater than the radiative recombination coefficient of traditional materials. This will act as a carrier confinement

mechanism and reduce carrier overflow even without carrier confinement layers, as we will investigate in Chapter 6.

Once excitons are formed, they will then recombine through radiative and non-radiative channels. A first-principles study predicts exciton radiative lifetimes of a few ps at 4 K, which increases linearly with temperature, rising to ~1 ns at 300 K [97]. This agrees with experimentally observed lifetimes [98–100], and is also similar to the lifetime of traditional semiconductors [101]. Thus, coupling to an optical cavity is necessary to achieve high modulation speeds >1 GHz.

Next, we consider some aspects of TMDC physics that may limit device efficiency: dark excitons, edge recombination, and exciton-exciton annihilation. Dark exciton states are present in all typical TMDC monolayers (WSe_2, MoS_2, etc.) [102]. The conduction and valence band edges are located at two inequivalent points in k-space, $\pm$K. Due to the lack of inversion symmetry and strong spin-orbit coupling, these valley degrees of freedom couple to spin (spin-valley coupling). Both the conduction and valence bands split into bands of opposite spin in each valley. The valence band splitting can be ~100s of meV, while the conduction band splitting is ~10s of meV [103]. For molybdenum-based TMDCs, electrons in the lowest conduction band have the same spin as holes in the highest valence band, and thus the lowest excitonic state is bright (since interaction with a photon cannot flip the spin). For tungsten-based TMDCs, the lowest conduction and highest valence bands have opposite spin, so the lowest exciton state is dark [103]. Fig. 31 illustrates the four basic exciton states. The lowest state is the A exciton, and can be bright or dark. Note that there are theoretically many other exciton states above the A exciton, but most of them are dark [97, 103].

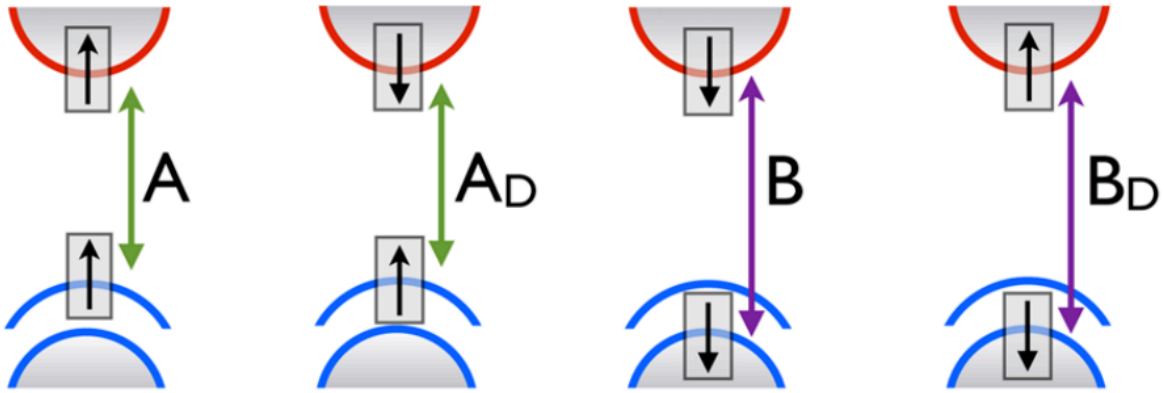

Figure 31. Schematic of basic exciton states in TMDCs: bright (A) and dark (A_D) A excitons, bright (B) and dark (B_D) B excitons. Conduction band spin splitting is not shown here. Reproduced from [97].

These dark exciton states will reduce the effect of antenna enhancement, since they do not get enhanced by the antenna and are only affected by non-radiative recombination mechanisms. The coupled rate equation for bright and dark excitons is [102]:

$$\frac{dN_b}{dt} = \frac{N_d}{\tau_{db}} - \frac{N_b}{\tau_{bd}} - \frac{N_b}{\tau} + B_b n^2 \quad (48)$$

$$\frac{dN_d}{dt} = \frac{N_b}{\tau_{bd}} - \frac{N_d}{\tau_{db}} - \frac{N_d}{\tau_{nr}} + B_d n^2 \quad (49)$$

where N_b and N_d are the bright and dark exciton densities, τ is the total lifetime, τ_{nr} is the non-radiative lifetime, τ_{db} and τ_{bd} are the scattering times from dark-to-bright and bright-to-dark excitons, and B_b and B_d are the exciton generation coefficients for bright and dark excitons. τ_{db} and τ_{bd} are related by $\tau_{db} = K\tau_{bd}$, where $K \equiv e^{\Delta E/kT}$, and $\Delta E = E_b - E_d$ is the bright-dark energy splitting. In photoluminescence experiments, only bright excitons are injected since only they couple to light. In electroluminescence experiments, we expect to inject bright and dark excitons following a thermal (Boltzmann) distribution; thus, we have $B_b = \frac{1}{K+1}B$ and $B_d = \frac{K}{K+1}B$, where $B = B_b + B_d$ is the total generation coefficient. We will solve these coupled rate equations and discuss the implications for modulation speed and efficiency in Chapter 6.

Although the surfaces of TMDC monolayers are in principle pristine, their edges contain dangling bonds that lead to non-radiative recombination. Just as with surface recombination in bulk materials, this can be described by an edge recombination velocity (ERV) v_e, defined using the boundary condition at the edge:

$$D\frac{dN}{dx}(x_{max}) = -v_e N(x_{max}) \quad (50)$$

at the +x boundary, for example. For devices smaller than the exciton diffusion length, this leads to an effective non-radiative lifetime

$$\tau_e \cong \frac{d}{2v_e} \quad (51)$$

where d is the smallest lateral size of the device. The ERV has been measured in WS_2 to be ~4×10^4 cm/s [104] (Fig. 32), comparable to passivated InGaAs [105]. Edge passivation techniques may be able to decrease the ERV, but as of today little work exists on this topic.

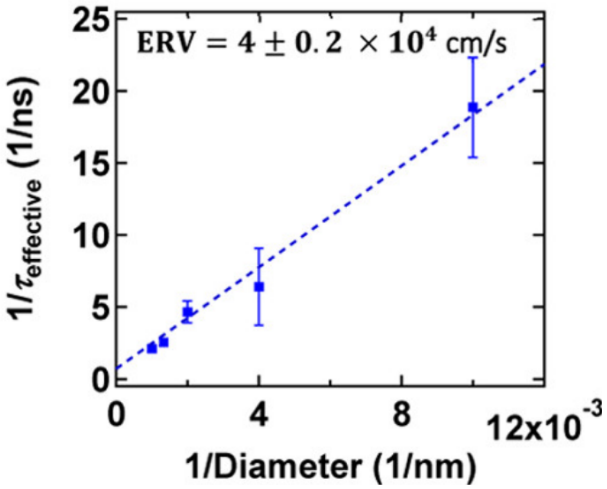

Figure 32. Exciton decay rate versus inverse disk diameter of etched WS_2 disks. Reproduced from [104].

For radiative recombination to overtake edge recombination, we require

$$\frac{\tau_{r0}}{F} \leq \frac{d}{2v_e} \tag{52}$$

where τ_{r0} is the unenhanced radiative lifetime (~1 ns) and F is the enhancement. The required enhancement versus d is plotted in Fig. 33 for $v_e = 4 \times 10^4$ cm/s. Good efficiency can be achieved even for very small device sizes. For an average enhancement of 100, the device size d need only be larger than ~8 nm for radiative recombination to dominate.

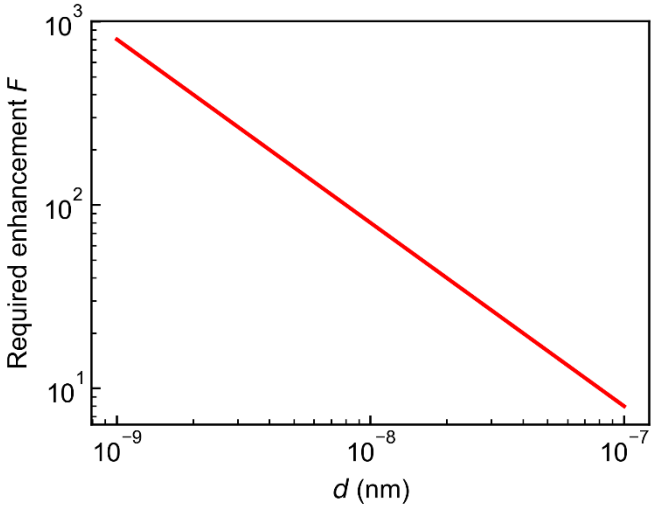

Figure 33. Required enhancement to overcome surface recombination, versus smallest dimension d.

Due to the strong coulomb interaction in TMDCs, excitons exhibit rich many-body interactions, the most important of which is exciton-exciton annihilation (EEA) [106, 107]. This can be included in the exciton rate equation as a $-CN^2$ term [99, 108]:

$$\frac{dN}{dt} = G - AN - CN^2 \tag{53}$$

where C is the EEA coefficient. Similar to Auger recombination in conventional materials, this will limit the device efficiency at high exciton densities, which ultimately limits the output power of the device. $C \sim 0.1$ cm^2/s in most substrate-supported TMDCs [106, 107], although WS_2 fully-encapsulated in hBN has notably shown much smaller $C \cong 6 \times 10^{-3}$ cm^2/s [106]. This shows that unlike the fixed Auger coefficient of traditional semiconductors, the EEA coefficient in TMDCs can be tuned by the environment. EEA will dominate over radiative recombination when $CN \cong A_r$. The output power is given by:

$$P_{out} = \eta_{ex}(\hbar\omega)A_r N a \tag{54}$$

where η_{ex} is the overall extraction efficiency, $\hbar\omega$ is the photon energy, A_r is the radiative rate, N is the exciton density, and a is the area of the device. For a highly scaled antenna-coupled device, we use $C = 0.1$ cm^2/s, $A_r = 1000/(1\ ns)$, $\hbar\omega = 1\ eV$, $a = (20\ nm) \times (200\ nm)$, $\eta_{ex} = 1$, and obtain $N = A_r/C = 10^{13}$ cm^{-2} and P_{out} = 6.4 μW. At a modulation rate of 40 Gbps, this is 1000 photons/bit, well above the quantum shot noise limit. Inefficiencies in waveguide coupling, waveguide loss, and detector sensitivity will raise the output power requirement, so strategies such as encapsulation to decrease the EEA coefficient should be further explored. The output power can also be increased by using multiple antenna devices in parallel, although the presence of multiple modes can hamper efficient waveguide coupling. We will discuss these issues further in Chapter 6.

4 Monolayer WSe_2 light-emitting diode

In this chapter, we will study what limits the efficiency and stability of large-area (~1-10μm) electrically-injected lateral-junction WSe_2 light-emitting diodes. This must be understood before shrinking the device area to the nanoscale, as is eventually desired. We show that lateral-junction WSe_2 LEDs suffer from severe decay in current at constant bias in ambient conditions. We will demonstrate that pulsed voltage operation can overcome this problem and result in greatly stabilized light emission over time. Quantum efficiency of EL matches that of PL, indicating efficient exciton generation with injected carriers. We demonstrate ~15 ns EL rise and fall times, a record modulation speed for TMDC LEDs. We will discuss the causes of the current decay in our devices and show that hole traps are responsible for current decay even in vacuum conditions, while atmospheric moisture contributes to both hole and electron current decay in ambient conditions.

4.1 Device design and fabrication

Our device design (Fig. 34) is a back-gated WSe_2 FET structure operated as a p-n diode. This is similar to previous lateral-junction structures [68–70], but with only a single gate rather than dual gates with separate gate voltages applied. This sacrifices the ability to control doping level independently of the source-drain bias, but we will show that high quantum efficiency can still be achieved. Also, this simpler fabrication process allows a smooth gate oxide (thermally grown SiO_2 on Si in our case) to be used. Fabrication of split gates usually involves first depositing the two metal gates, then depositing the oxide. If this is done using standard atomic-layer deposition (ALD) or chemical vapor deposition (CVD), the surface roughness of the metal gates is transmitted through the oxide, resulting in a rough monolayer/oxide interface that may degrade device performance [109].

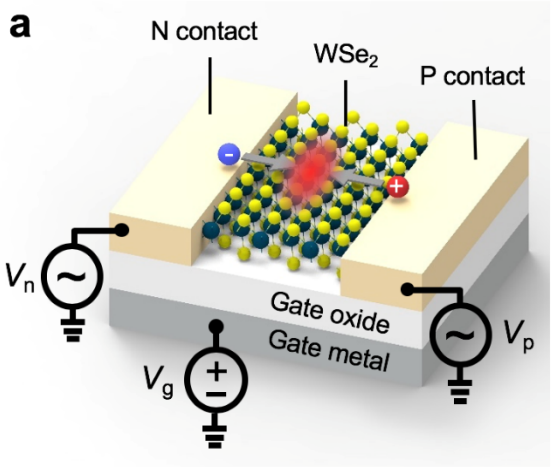

Figure 34. Schematic of WSe_2 lateral-junction LED.

Our gate stack is either thermally grown 50 nm SiO_2 on a p++ Si substrate, or 20 nm Al_2O_3 deposited by ALD on an ITO (280 nm)/glass substrate. Devices on both substrates showed bright light emission.

The thickness of the oxide greatly affects the light outcoupling efficiency due to constructive or destructive interference from the substrate [110] (Fig. 35). The optimal thickness of SiO_2 on Si for maximum outcoupling at 750 nm is ~100 nm, but a lower thickness is desired for efficient gating of the device. Since the source-drain voltage is not controlled separately from the gating voltages, a larger source-drain voltage is needed for a thicker gate oxide, which will increase power consumption and degrade energy efficiency. Thus, we chose 50 nm SiO_2 as a compromise between thinner for better gating and thicker for better outcoupling. The light outcoupling efficiency for 50 nm SiO_2 on Si is calculated from FDTD simulation to be 10% for the emission wavelength of 750 nm. For the devices on Al_2O_3, the substrate materials are nearly transparent, so interference effects are not as severe, and the oxide can be made thinner. FDTD simulation predicts a 7% outcoupling efficiency for this substrate. For optimal outcoupling efficiency, metal back mirrors or distributed Bragg reflectors (DBRs) can be used [111], but in this study we are primarily interested in the internal quantum efficiency of light emission.

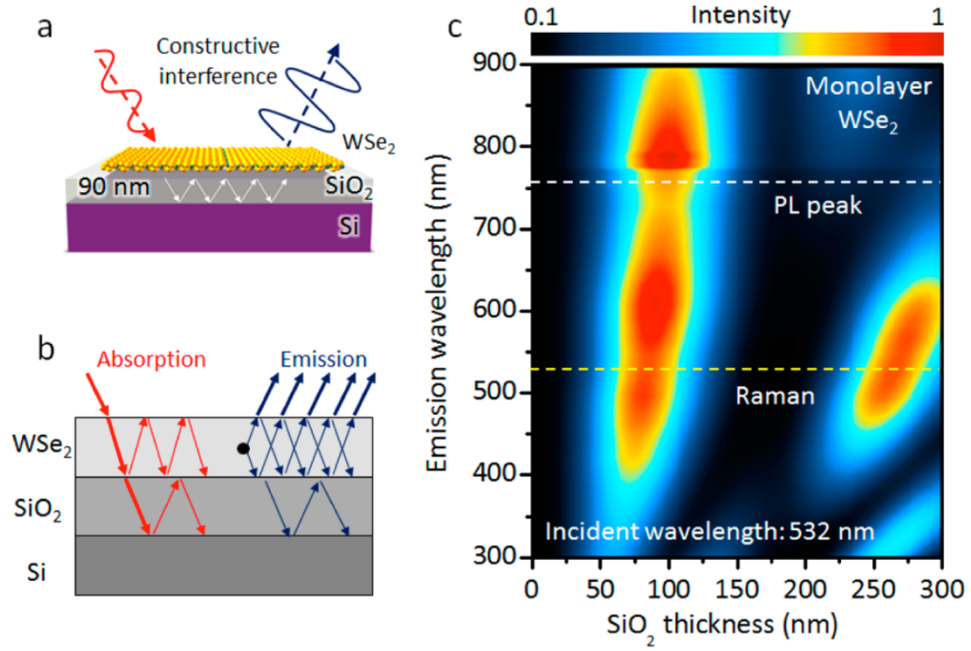

Figure 35. a, b) Interference effects for light absorption or emission of WSe_2 on SiO_2/Si substrate. c) Map of outcoupled intensity versus SiO_2 thickness and emission wavelength. Reproduced from [110].

For the active material, WSe_2 was chosen due to its ambipolar nature [112], required for bipolar carrier injection. In addition, WSe_2 shows higher unprocessed quantum yield than most other TMDCs, particularly the most commonly-studied MoS_2 (Fig. 36).

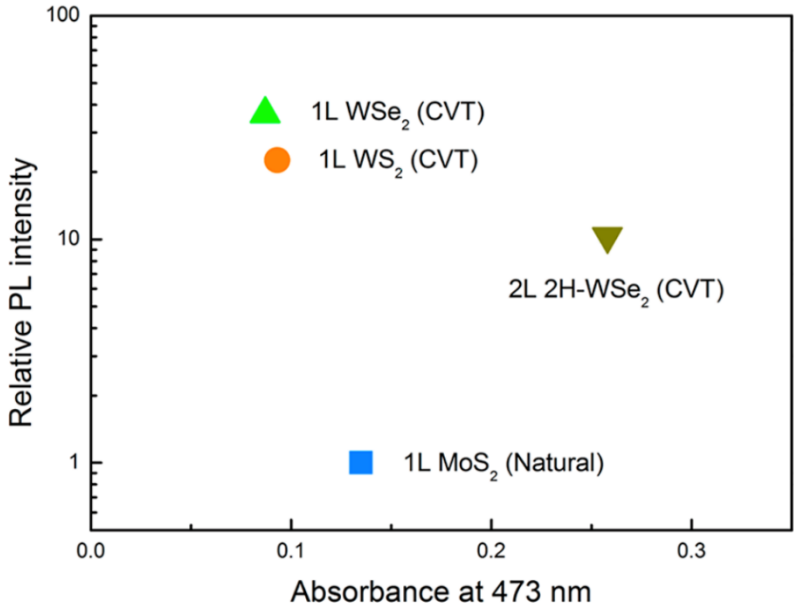

Figure 36. Relative PL intensity and absorbance of various 2D materials. Reproduced from [113].

After preparing the gate stack, CVD-grown WSe_2 is transferred using a pick-and-place method. Monolayer WSe_2 flakes ~50-100 µm in size are grown on a quartz substrate [114]. For transfer, a thick (>5 µm) poly(methyl methacrylate) (PMMA) film is first spun on an SiO_2 substrate, then ~100x100 µm slabs are cut out and placed atop the flakes on the growth substrate. This is then heated to 160 C for 3 min to adhere the PMMA slabs to the flakes. The slabs are then picked up and placed on the target surface, followed by another heating cycle at 160 C for 3 min to adhere the flakes to the target substrate. Finally, the PMMA is removed using dichloromethane (DCM) for 5 min. DCM was found to give better adhesion of the flakes after transfer compared to acetone. The target substrate is then placed in acetone for ~5 min to clean any remaining PMMA residue.

For SiO_2/Si substrates, acetone also releases strain in the monolayer. Residual tensile strain can greatly reduce the PL intensity and redshift the spectrum [114], and a >30x boost in the PL intensity was observed after this acetone treatment (Fig. 37a) [115]. The strain is released in the first few seconds of immersion in acetone [115]. However, note that the acetone treatment does not work on all substrates. Fig. 37b,c show the results of acetone treatment on WSe_2 transferred on Al_2O_3/Si and HfO_2/Si substrates respectively. The highest PL enhancement is measured on as-grown flakes (on quartz) and transferred flakes on SiO_2. Flakes on HfO_2 showed a small (~2x) enhancement, and on Al_2O_3 show no enhancement or small decrease. The reason is not known but is likely related to surface roughness or different surface adhesion forces. The RMS

roughnesses were 5Å for SiO_2/Si, 14Å for Al_2O_3/Si, and 10Å for HfO_2/Si, measured using atomic force microscopy (AFM).

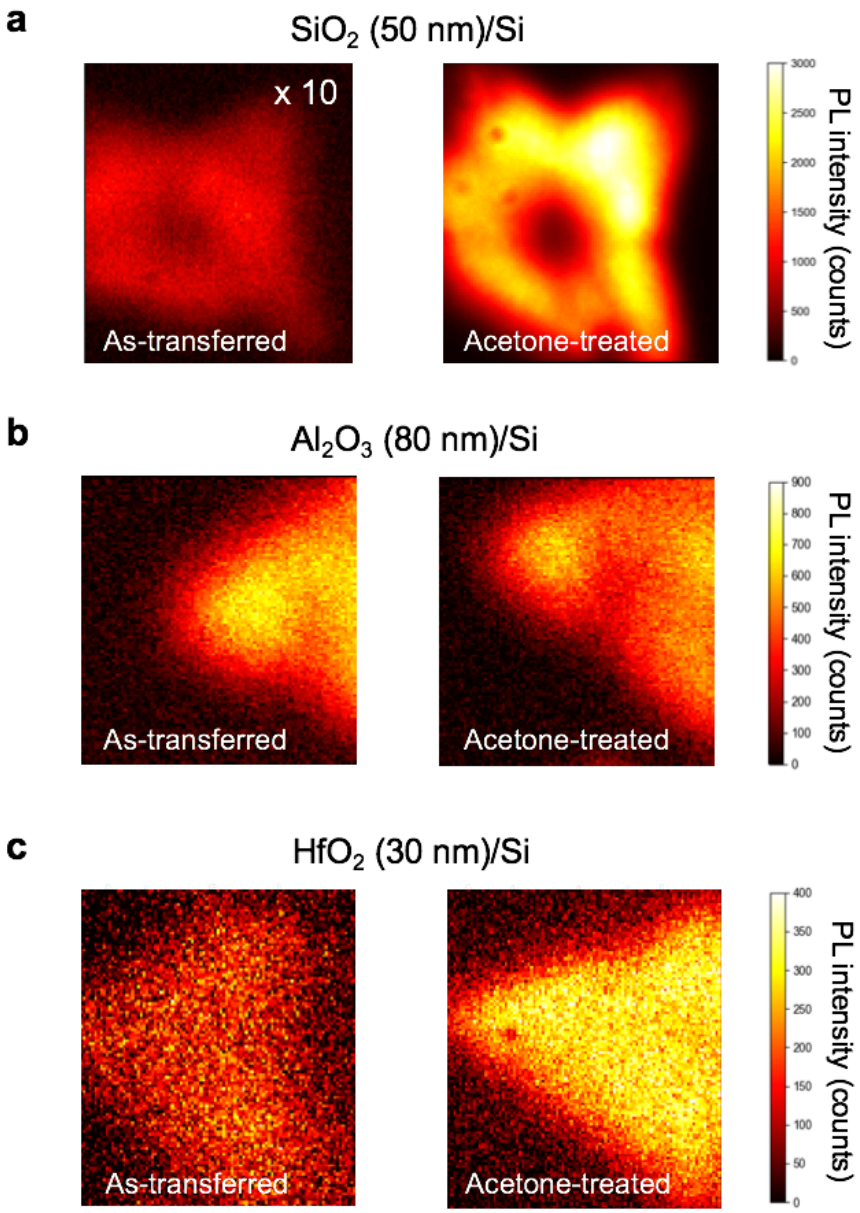

Figure 37. Spatial PL maps of monolayer WSe_2 after transfer on various substrates, before (left) and after (right) immersion in acetone. a) SiO_2 (50 nm)/Si, b) Al_2O_3 (80 nm)/Si, c) HfO_2 (30 nm)/Si.

After transfer, contacts are patterned using electron-beam lithography (EBL) followed by thermal evaporation of Ni (15 nm) and liftoff for 30 min in acetone. Electron-beam evaporation was found to severely damage the monolayer, even without any lithography beforehand. A decrease in PL intensity of ~15x was observed (Fig. 38). This is presumably due to X-ray

radiation or free electron radiation from the electron beam striking the metal target. Backscattered electrons have been shown to cause resist blistering and peeling during e-beam evaporation in a high-electron mobility transistor (HEMT) process [116]. Thermal evaporation only resulted in a minor decrease in PL intensity (Fig. 38).

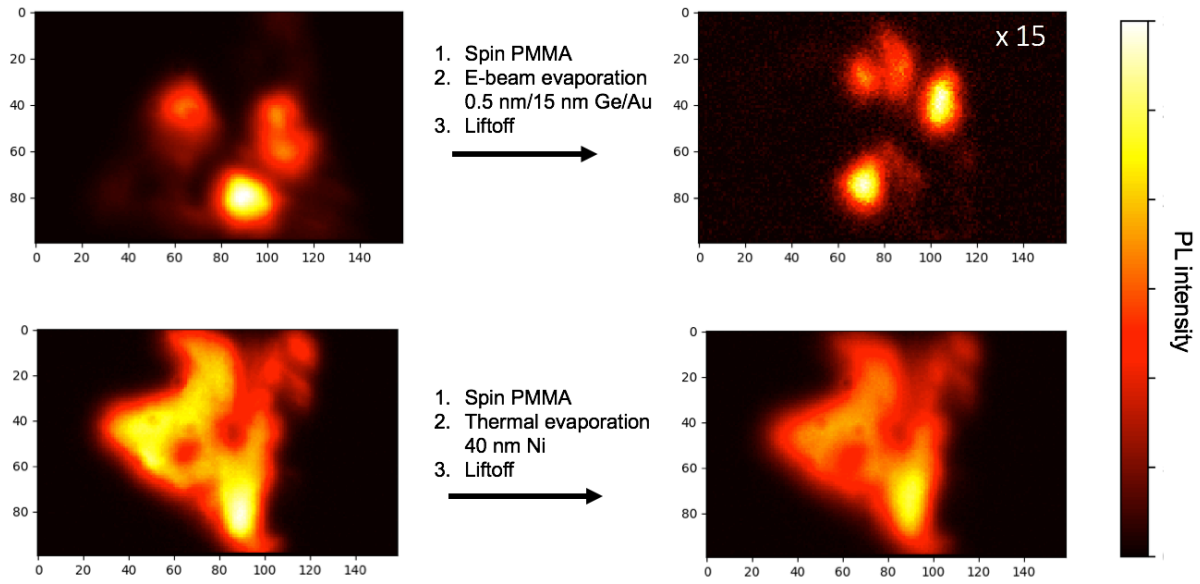

Figure 38. Spatial PL maps before and after e-beam (top) and thermal (bottom) evaporation. No lithography was done, and the metal film was completely removed during liftoff.

4.2 Setup efficiency calibration

In order to accurately assess the internal quantum efficiency of the device using the measured light at the detector, it is important to take all optical loss mechanisms into account from the device to the detector. For electroluminescence measurements, these include the light outcoupling efficiency out of the device, the collection efficiency of the objective, the transmission efficiency of the optics, and the efficiency of the detector. For photoluminescence, this also includes the absorption efficiency of the pump light. As mentioned above, the simulated light outcoupling efficiency is ~10% for the device on SiO_2 and ~7% for the device on Al_2O_3. Schematics of the EL and PL measurement setups are shown in Fig. 39. The beamsplitter for EL is only used to couple white light from a lamp for imaging the sample; this lamp is turned off during EL measurement.

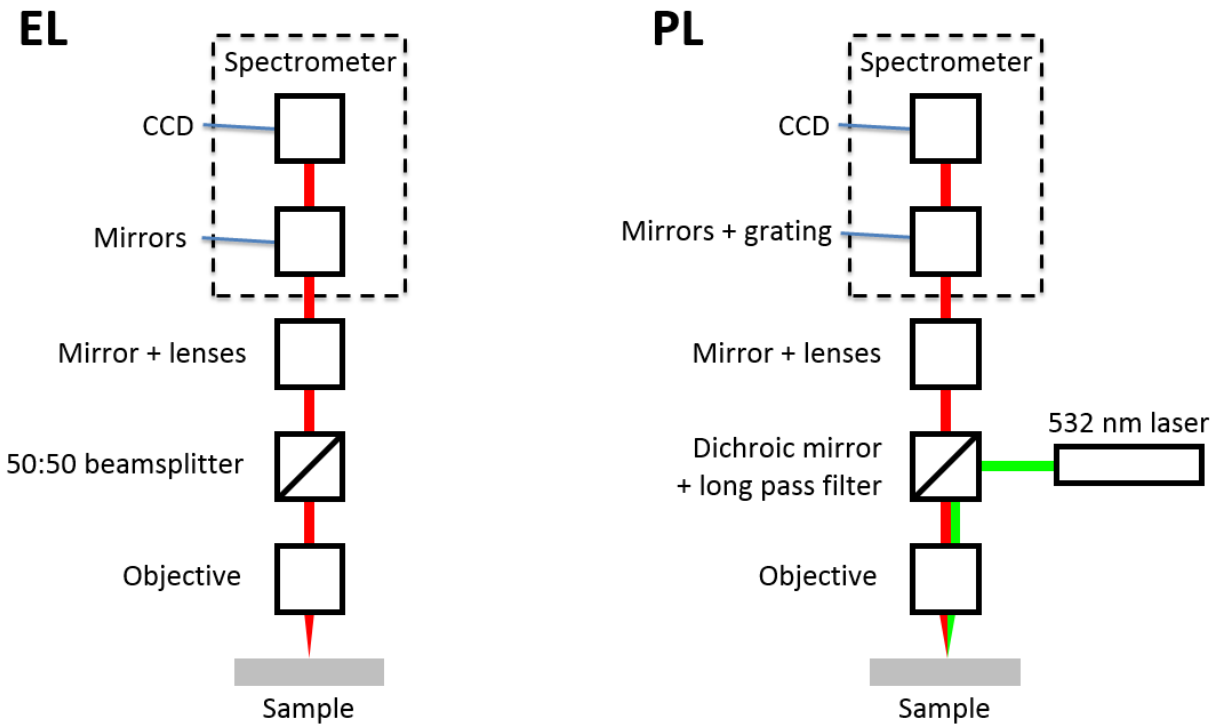

Figure 39. Schematic of electroluminescence measurement setup (left) and photoluminescence measurement setup (right). The spectrometer is enclosed and includes mirrors, grating, and CCD.

To find the efficiency of the setup, including objective, mirrors, lenses, and CCD, we use the 532 nm laser incident on a Spectralon sample, which simulates an ideal Lambertian scatterer, and measure the ratio of incident power to collected power on the CCD. The setup is shown in Fig. 40.

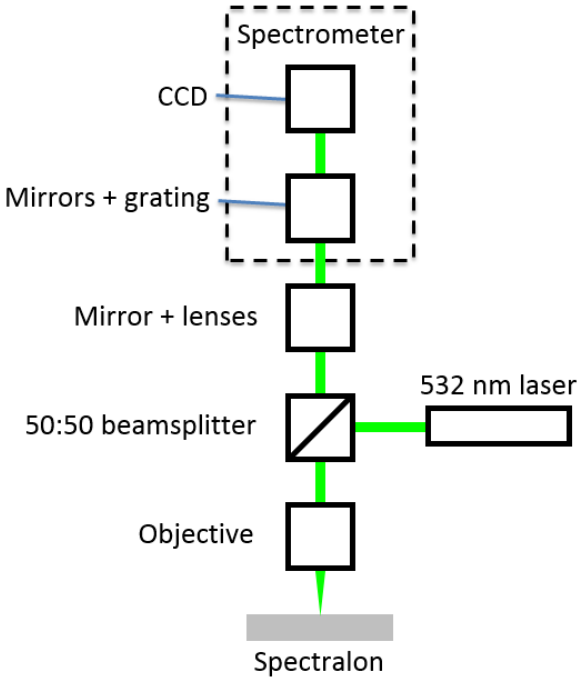

Figure 40. Schematic for measuring absolute setup efficiency at 532 nm.

A Lambertian scatterer is one in which scattered intensity scales as the cosine of the angle from the normal, regardless of the incident angle of the light. This is necessary since the actual LED will have wide angle emission. However, the LED emission pattern will only be approximately Lambertian. Fig. 41 shows the simulated far field pattern of a dipole placed on the 50 nm SiO_2/Si substrate (a, b) as well as the 20 nm Al_2O_3/280 nm ITO/glass substrate (c, d), for angular slices parallel and perpendicular to the dipole. In fact, for SiO_2/Si, both the parallel and perpendicular patterns are very close to a "dipolar" $I \propto \cos^2(\theta)$ emission pattern rather than $I \propto \cos(\theta)$. For Al_2O_3/ITO, both are in between $\cos^2(\theta)$ and $\cos(\theta)$. We can find the theoretical collection efficiency for a given numerical aperture in each case. For Lambertian emission, it is given by

$$\eta_L = \frac{\int_0^{\theta_0} \cos(\theta)\sin(\theta)\,d\theta}{\int_0^{\pi/2} \cos(\theta)\sin(\theta)\,d\theta} = \frac{1}{2}(1-\cos(2\theta_0)) = (NA)^2 \tag{55}$$

where $NA = \sin(\theta_0)$ is the numerical aperture. For "dipolar" emission, it is:

$$\eta_D = \frac{\int_0^{\theta_0} \cos^2(\theta)\sin(\theta)\,d\theta}{\int_0^{\pi/2} \cos^2(\theta)\sin(\theta)\,d\theta} = 1-\cos^3(\theta_0) = 1-(1-NA^2)^{3/2} \tag{56}$$

For our 20x objective, NA = 0.42, giving $\eta_L = 17.6\%$ and $\eta_D = 25.3\%$, which are fairly close. Surface roughness in real devices may cause multiple reflections and make the emission pattern closer to Lambertian [117]. The SiO_2 surface and SiO_2/Si interface are very smooth here (~nm), so this is not expected to play a significant role.

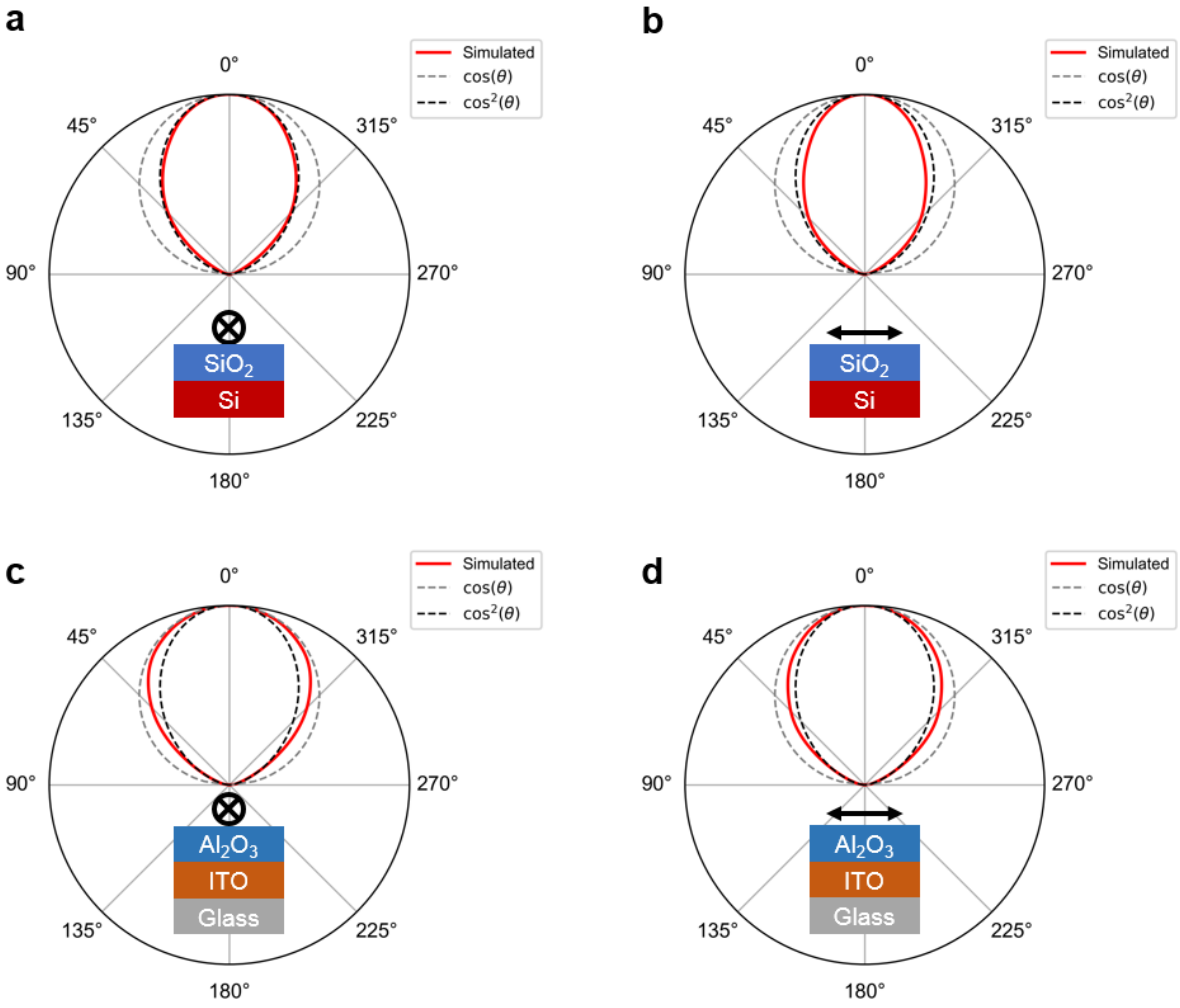

Figure 41. Simulated far field intensity patterns for dipole on SiO_2/Si substrate and Al_2O_3/ITO/glass substrate. a) SiO_2 substrate, perpendicular to dipole. b) SiO_2 substrate, parallel to dipole. c) Al_2O_3 substrate, perpendicular to dipole. d) Al_2O_3 substrate, parallel to dipole.

First, to confirm that the Spectralon is operating as expected, we compare the relative scattered power from the Spectralon and the gold mirror. The gold mirror is a near-ideal reflector, so the reflected angle equals the incident angle and all light should be collected by the objective. We measure a ratio of 16.8%, very close to the ideal 17.6%.

For the setup efficiency, we must also divide by the transmission of the beamsplitter, which will not be present in PL measurements. The beamsplitter transmission spectrum is shown in Fig. 42, along with the transmission of the dichroic mirror and long pass filter used in PL. The beamsplitter has ~45% transmission at 532 nm. We finally obtain $\eta_{setup} = 3.6 \times 10^{-3}$ at 532 nm using this method.

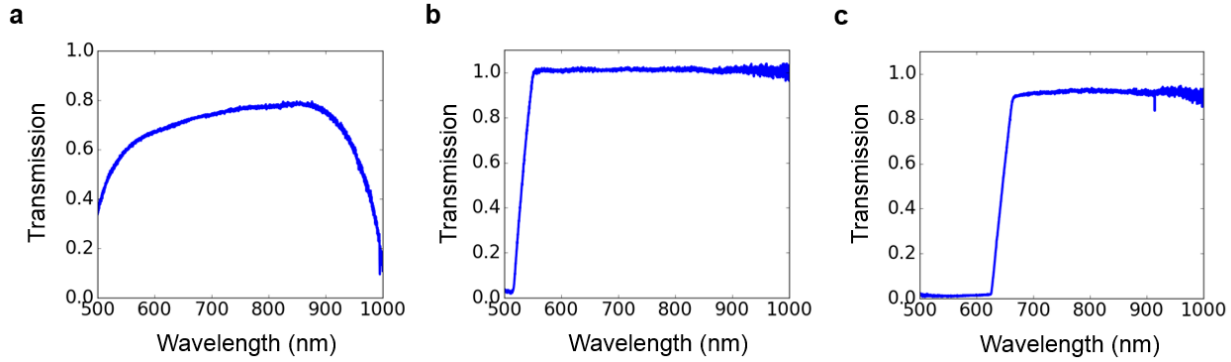

Figure 42. Transmission efficiency spectra of various components. a) 50:50 beamsplitter, b) 532 nm dichroic mirror, c) 645 nm long pass filter.

Next, to find the setup efficiency at other wavelengths, we use a blackbody source with a known spectrum to find the relative efficiency spectrum, and use the absolute efficiency at 532 nm to fix the final spectrum. The setup is shown in Fig. 43a, along with the blackbody spectrum from the datasheet (Fig. 43b), and the final efficiency spectrum (Fig. 43c).

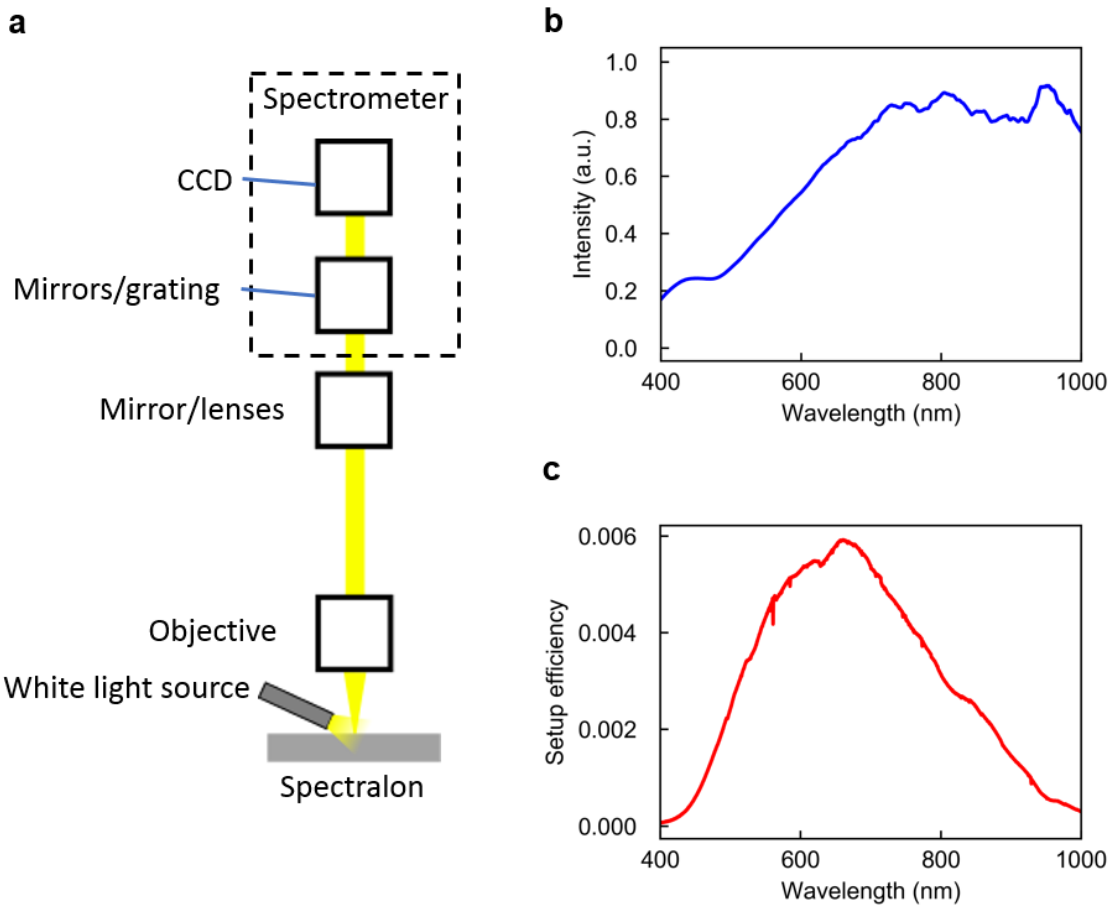

Figure 43. a) Schematic for measuring relativity spectral efficiency using a blackbody source. b) Emission spectrum of blackbody source from datasheet [118]. c) Final absolute setup efficiency spectrum.

The final spectrum in Fig. 43c does not include the beamsplitter, dichroic mirror, or long pass filter. For EL (Fig. 39a), we can multiply by the beamsplitter transmission (Fig. 42a), and for PL (Fig. 39b), we multiply by the dichroic and long pass filter transmission (Fig. 42b, c).

To find PL IQE, we also need the absorbance of the monolayer WSe_2. For a monolayer on a transparent substrate, it is possible to calculate absorbance from a differential reflectance measurement, using the formula [113]:

$$\delta_R(\lambda) = \frac{4}{n_{sub}^2 - 1} A(\lambda) \tag{57}$$

where $\delta_R(\lambda)$ is the differential reflectance, $A(\lambda)$ is the absorbance, and n_{sub} is the refractive index of the substrate. $\delta_R(\lambda)$ is given by

$$\delta_R(\lambda) \equiv 1 - R_{WSe2}/R_{sub} \tag{58}$$

where R_{WSe2} is the reflectance of the monolayer on the substrate and R_{sub} is the reflectance of the bare substrate. To measure reflectance, a white light source was shone on the sample and the reflected light was spatially filtered and passed into a grating spectrometer. The measured differential reflectance of as-grown CVD WSe_2 on quartz is shown in Fig. 44a, along with the literature values for exfoliated flakes. The peak at 750 nm in the literature and 780 nm here is due to the A exciton resonance. It is redshifted here due to strain in as-grown CVD flakes, as mentioned above. At 532 nm, the pump wavelength, the result agrees reasonably well with literature. The calculated absorbance is shown in Fig. 44b. We have also plotted the FDTD simulated absorbance using literature values for the complex refractive index (n, k) of monolayer WSe_2 [119], and see a good agreement at 532 nm. The lack of peaks in the simulated absorbance is due to limitations of the simulation software, which must model the dielectric constant using a finite-order fitting scheme.

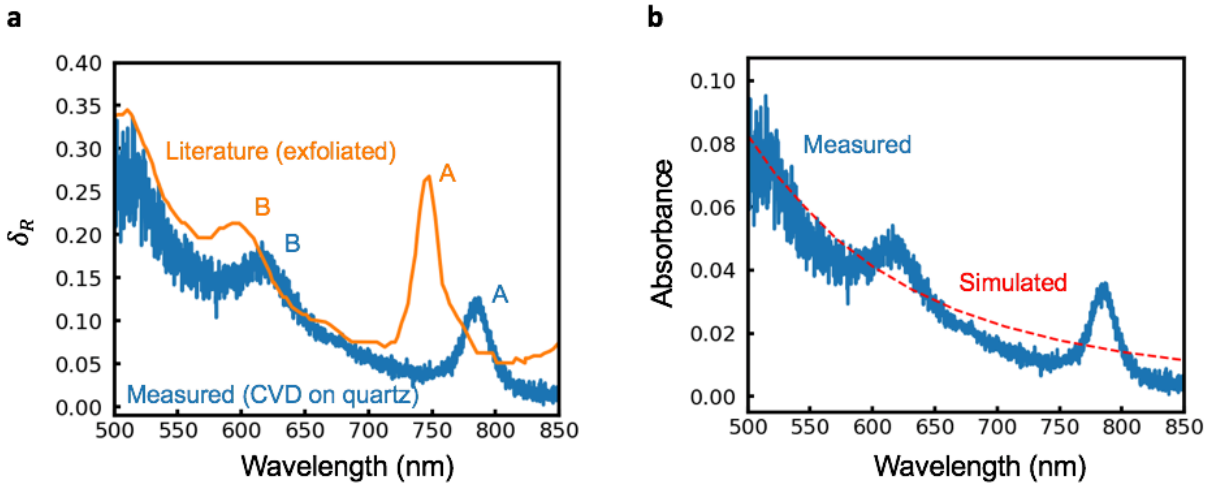

Figure 44. a) Differential reflectance for CVD WSe_2 on quartz (blue) and literature values for exfoliated flakes (orange). b) Calculated absorbance from measured reflectance (blue) and FDTD simulated values (red).

For non-transparent substrates such as our gate stacks of interest, there is no simple formula for the absorbance in terms of the reflectance. However, due to the good agreement of the FDTD results with the calculated absorbance above, we can use FDTD simulation to find the absorbance in these other cases. We obtain an absorbance at 532 nm of 13.7% on SiO_2/Si and 6.12% on Al_2O_3/ITO/glass.

4.3 Measurement results

Now that we have described the design and fabrication process as well as the measurement setup and efficiency calculation, we turn to the measurement results. First, to confirm the ambipolar nature of the monolayers, I_d-V_g measurements are taken with the devices operated in FET mode. Indeed, most devices were ambipolar or slightly p-type in their I_d-V_g characteristics (Fig. 45, left). Identical structures using monolayer MoS_2 showed only n-type I_d-V_g and no light emission (Fig. 45, right). For diode operation, one contact is designated as the P contact with alternating voltage between V_p and V_g. The other (N) contact alternates between V_n and V_g, with $V_n < 0$ (Fig. 46a). Light is emitted only during the on period t_{on}. Fig. 46b shows the EL spectrum of the device overlaid with the PL spectrum of the same device. The clear peak at ~1.65 eV shows that EL and PL are both due to the usual recombination of A excitons, and confirms the monolayer nature of the flakes. Fig. 46c shows the light emission overlaid on an image of the device, confirming emission comes from the channel region.

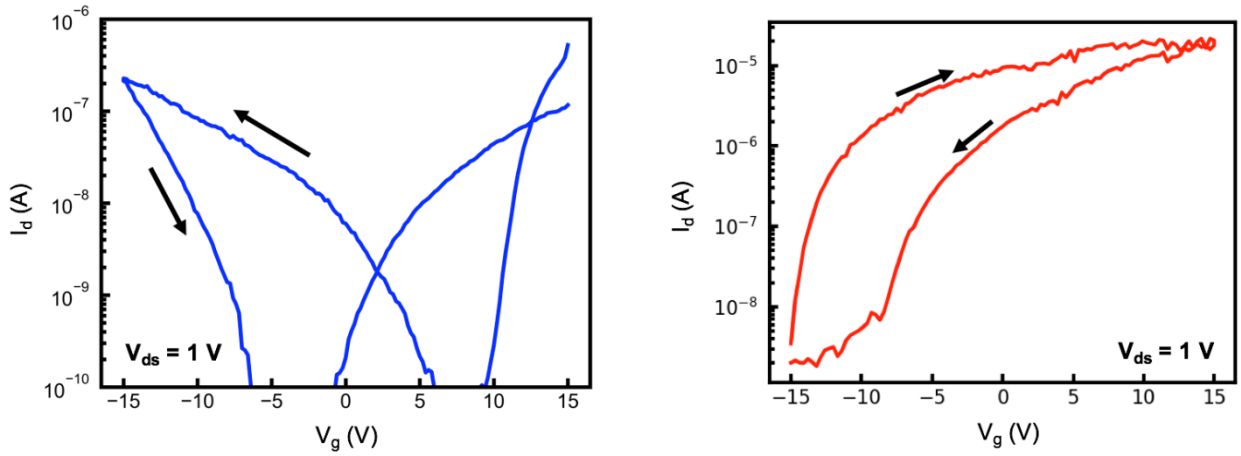

Figure 45. I_d-V_g curves at V_d = 1V for WSe_2 (left) and MoS_2 (right) FETs in ambient conditions.

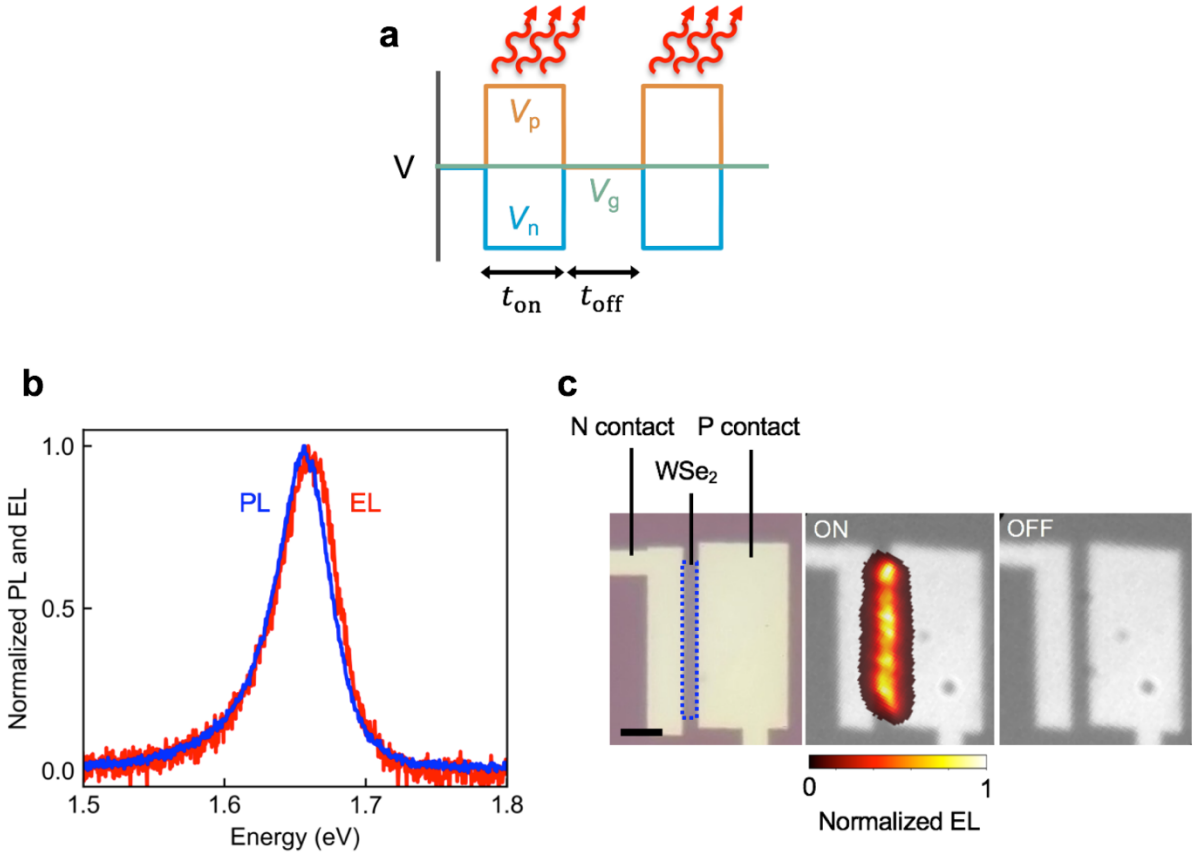

Figure 46. a) Schematic of pulsing scheme. b) EL and PL spectra. c) Optical micrograph and EL spatial map of device on Al_2O_3 when device is on (voltage applied) and off (no voltage applied).

To illustrate the need for pulsed bias, we measure EL versus time and current versus time for both DC (step) voltage and pulsed voltage at 5 kHz. Bright emission is observed under both DC and pulsed bias. Note that the emission mechanism in our devices is clearly distinct from the pulsed light-emitting capacitor reported previously [83], since continuous light emission is seen on a scale of ~seconds, as opposed to the ~10 ns pulses that only occur during voltage transitions. However, under DC bias, both emission and current rapidly decay by orders of magnitude within a few seconds (Fig. 47a, b). Past reports on current decay in MoS_2 FETs show roughly comparable time constants ~10 s [61, 63]. We will return to the cause of this current decay later.

The ratio of light emission to current, which is proportional to the efficiency, remains roughly constant over time, showing that the decay in current is responsible for the decay in light emission. In contrast, pulsed bias yields extremely stable light emission and current over >1000s (Fig. 47c, d). Most devices under pulsed bias showed no decrease or small decrease (<2x) in light emission in the first few minutes, then stayed stable for the remaining duration of the applied bias, with the longest test performed being >3 hours (Fig. 48).

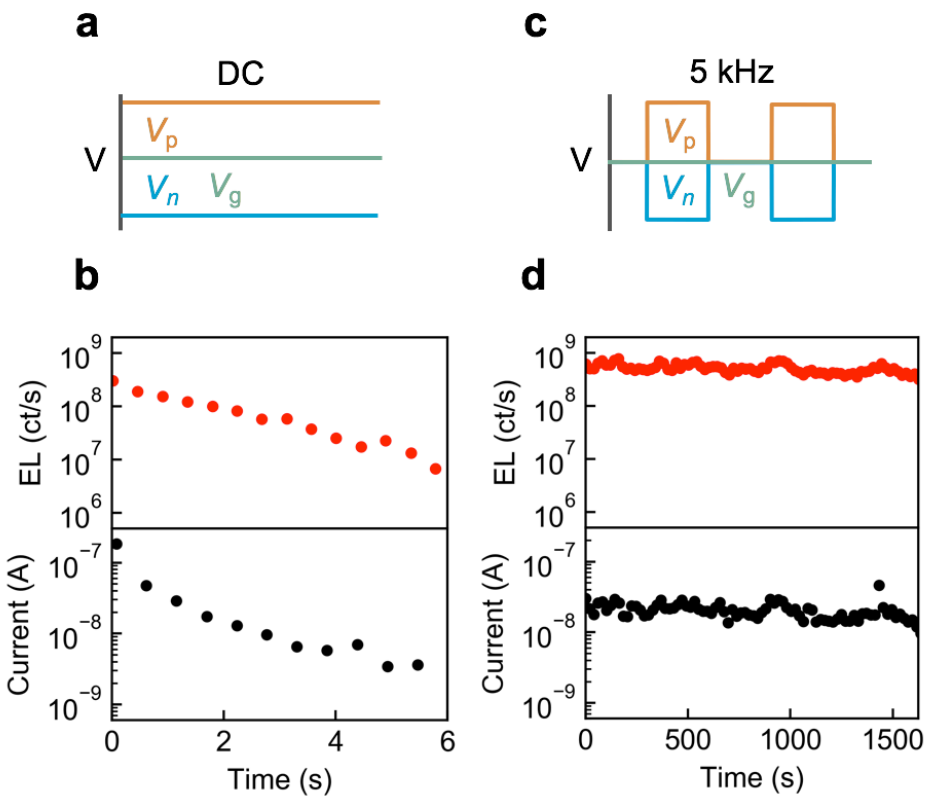

Figure 47. a) DC bias scheme, with $V_p = -V_n = 4$ V. b) EL (top) and current (bottom) under DC bias.

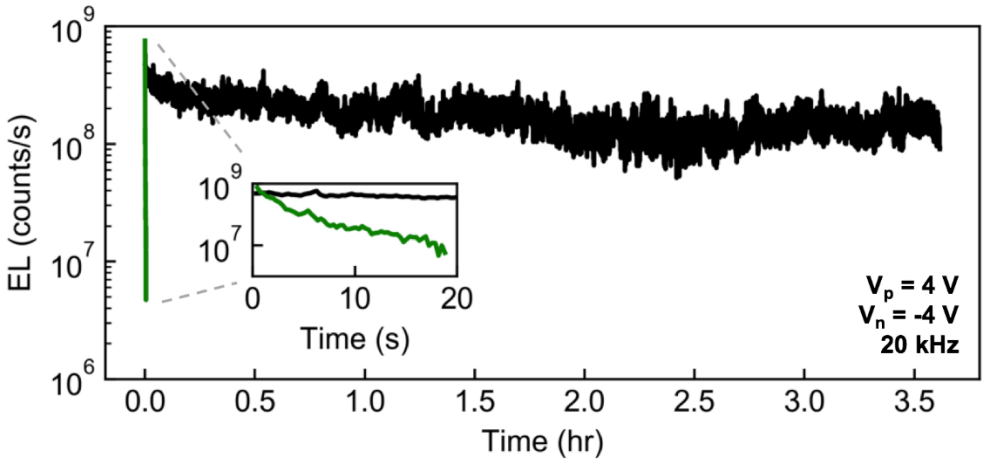

Figure 48. Emission intensity over longer duration, for device on Al2O3 substrate. Black: pulsing at 20 kHz. Green: DC bias. Inset: close up of DC bias.

The frequency response is shown in Fig. 49. Here, emission intensity is defined as the average intensity over 10s, starting 5s after the pulsed bias is applied. Above ~1 kHz, emission intensity is relatively stable with frequency, while below ~1 kHz, current decay causes EL to drop very quickly. However, note that the stability also depends on duty cycle, which is fixed at 50% here. For very low duty cycle (long t_{off}), emission intensity can still be stable at low frequencies ~1 Hz (Fig. 50).

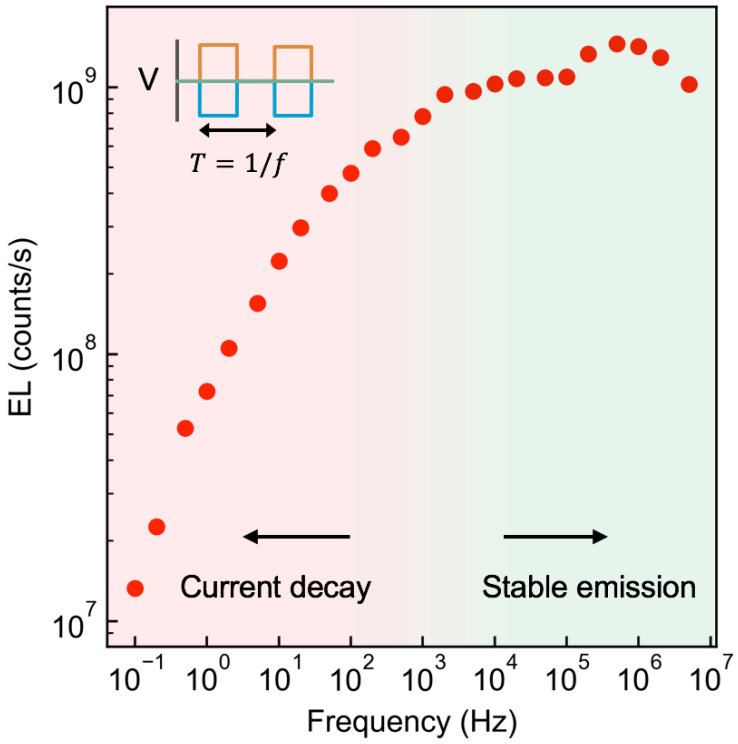

Figure 49. Frequency response of device on Al_2O_3 under pulsed bias with 50% duty cycle, V_p = -V_n = 4.5 V. EL is defined as the average intensity over 10s, starting 5s from when the pulse is applied.

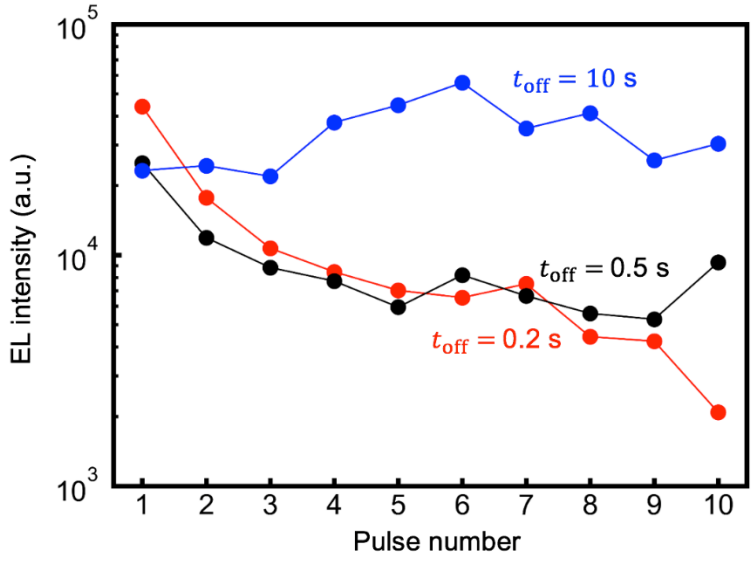

Figure 50. EL intensity during a series of pulses, with fixed t_{on} = 0.5 and varying t_{off}. For t_{off} > 10s, emission intensity fluctuates but does not decrease overall.

Next, we study the emission characteristics under varying bias to extract the optimal bias condition. The relative injection level of electrons and holes, and thus the exciton formation efficiency, depends on the voltages $(V_p - V_g)$ and $(V_n - V_g)$ applied to the contacts. If $|V_p - V_g| \gg |V_n - V_g|$, holes will be predominantly injected and will simply diffuse across the channel to the opposite contact without forming excitons, and vice versa for $|V_p - V_g| \ll |V_n - V_g|$ (Fig. 51a). We determine the optimal bias condition by keeping $(V_p - V_n)$ constant and sweeping V_g from V_n to V_p while tracking the EL and current.

Fig. 51b shows the EL intensity of a device on SiO_2 versus gate voltage, where V_p and V_n are fixed at $V_p = 5\ V$ and $V_n = -5\ V$, along with the current and EL efficiency. Each point corresponds to one on period $t_{on} = 0.5$s, and current and emission intensity are defined as the time-average during the on period. An off time of t_{off} = 10s is used to recover the device between pulses, as shown in Fig. 50. The relatively long on period is chosen due to the ease of measuring current at low frequencies. The brightest emission occurs near V_g = 0 V, where both holes and electrons are injected. The minimum current point at $V_g \cong 1.8$ V corresponds to the most bipolar injection, and coincides with the highest internal quantum efficiency ~1%. $|V_p - V_g| < |V_n - V_g|$ at this point, indicating slightly p-type characteristics typical of monolayer WSe_2. We obtain an L-I curve at optimal bias conditions by first setting $V_g = 1.25$ V, approximately the point of maximum efficiency above, where current is also not too low. Then we increase the source-drain bias while keeping $|V_p - V_g|/|V_n - V_g|$ constant at ~0.6. For comparison, we also take an L-I curve with V_g = 0 (i.e. equal $|V_p - V_g|$ and $|V_n - V_g|$). L-I and IQE are plotted in Fig. 51c, along with the corresponding PL L-L curves. PL shows a roughly constant IQE of ~1.6%, while EL at

optimal bias shows a peak of ~1.3% at low current and decreases slightly at higher currents, possibly due to variation in optimal bias condition with voltage. In contrast, EL at equal P and N bias is low (~0.3%) at low current and stays below ~0.8% throughout.

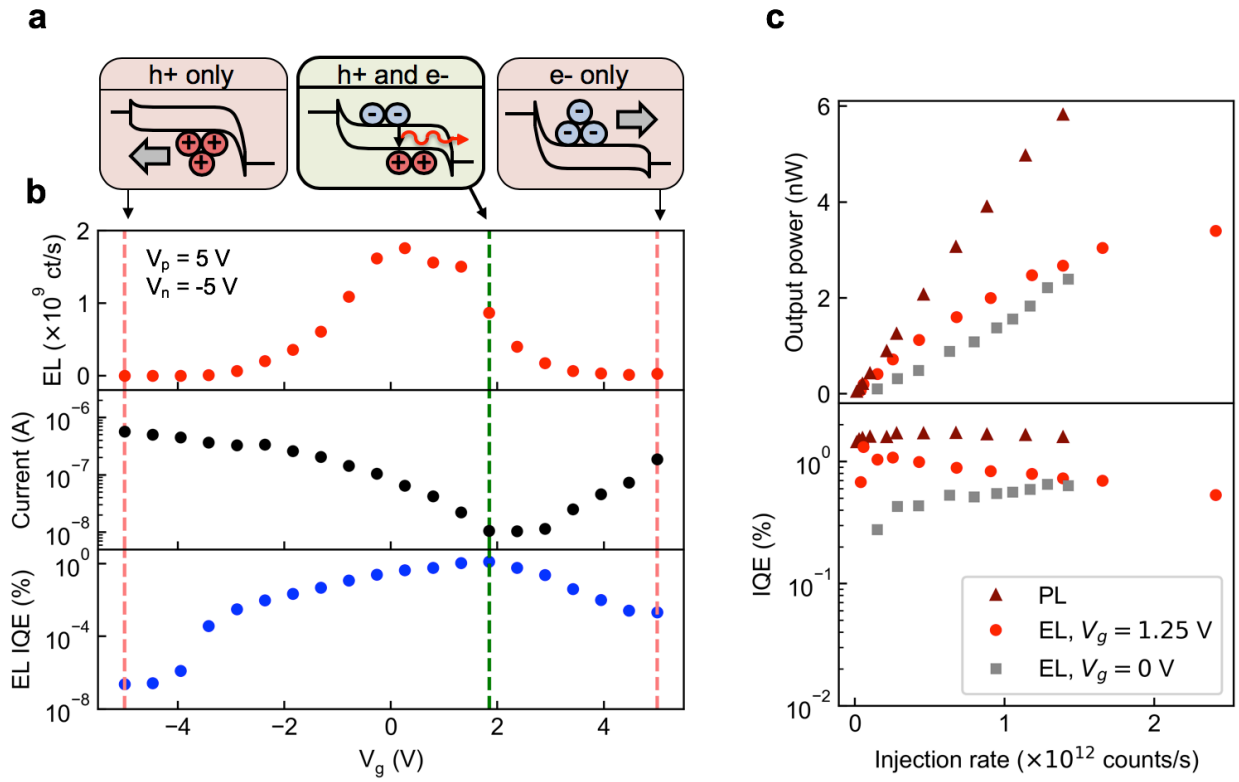

Figure 51. a) Operating regimes: hole injection only (left), bipolar injection and light emission (center), and electron injection only (right). b) EL intensity, current, and EL IQE versus gate voltage, for constant $V_p = -V_n = 5$ V. c) Output power (top) and IQE (bottom) versus injection rate, for PL and EL at two different bias conditions.

Next, we study the modulation speed of the device by performing time-resolved measurements using time-correlated single-photon counting (TCSPC). Fig. 52 shows the measurement setup. Devices on the transparent Al_2O_3 substrate are used since our TCSPC setup requires backside emission. The device is excited using two synchronized function generators that also output a trigger pulse going to the TCSPC electronics. Emission is collected through a 20x objective and focused onto a silicon avalanche photodiode (APD), which is also connected to the TCSPC electronics. It is important that the emission is dimmed enough that only a maximum of one photon per pulse is collected by the APD. From the delay between the trigger pulse and the APD signal, a histogram of photon counts over time is built up. The instrument response is measured using a Ti:Sapphire femtosecond laser to be ~40 ps, well under the relevant times measured here.

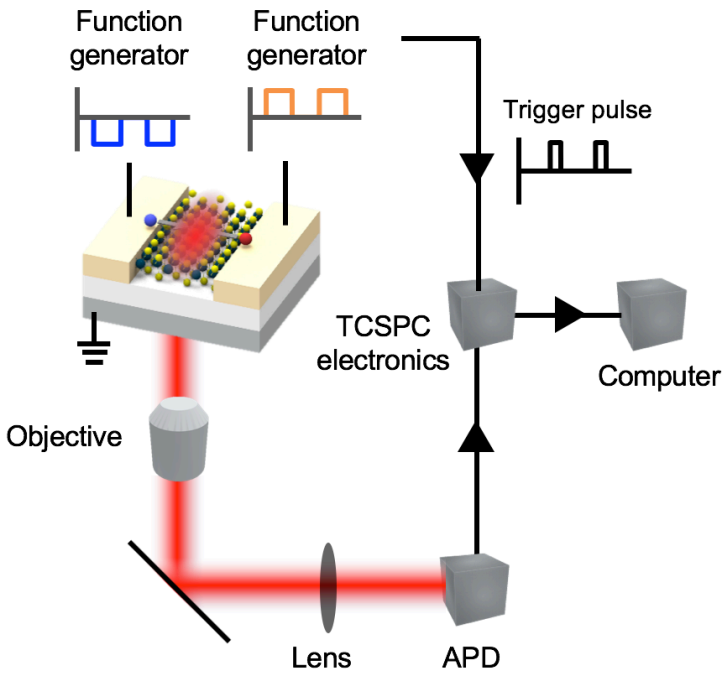

Figure 52. Schematic of TCSPC setup.

Fig. 53 shows time-resolved electroluminescence at 1 MHz, together with the P and N voltage pulses measured on an oscilloscope. The pulses are offset so that part of the period is hole injection only, part is electron injection only, and part is bipolar injection. Indeed, emission only occurs when both P and N voltage are applied, confirming that bipolar carrier injection is required for light emission. The emission intensity is nearly constant during the entire P/N voltage overlap period. The rise and fall times shown in the inset are ~12 ns and ~18 ns respectively. We note that this rise/fall time is ~20x faster than monolayer LEDs using vertical tunnel injection heterostructures [33], which is likely due to the lower capacitance of the lateral injection scheme used here. To our knowledge, this is the fastest direct modulation speed reported for TMDC LEDs.

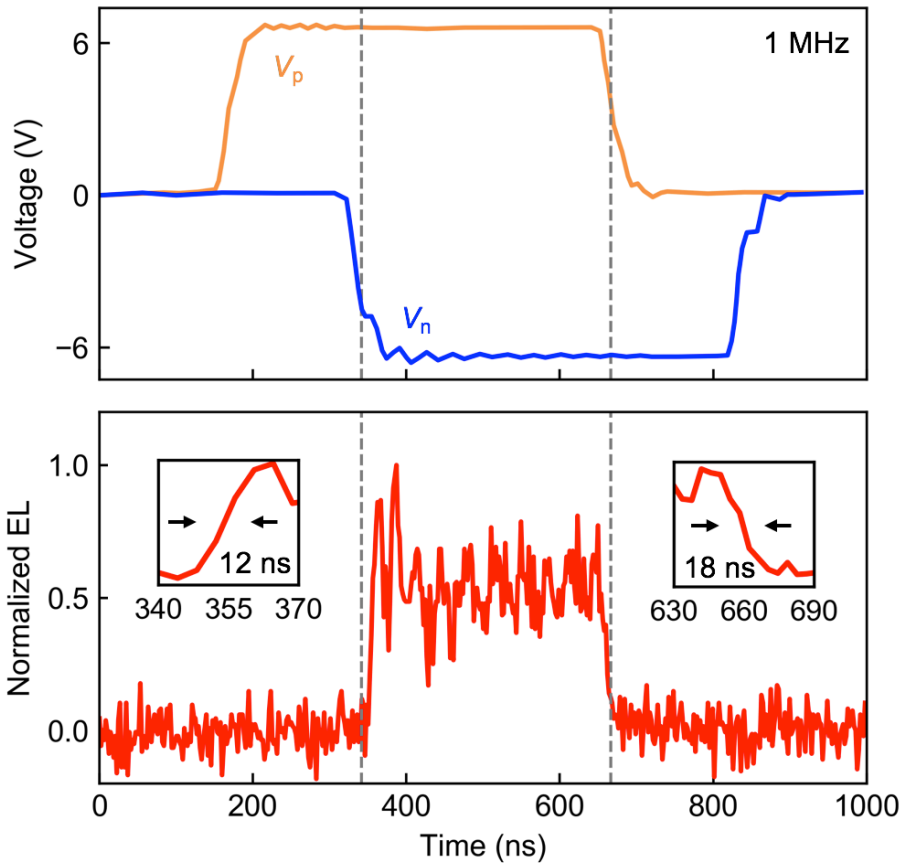

Figure 53. Time-resolved electroluminescence at 1 MHz. Top: P and N voltage pulses. Bottom: Normalized EL. Insets: rise and fall times.

4.4 Causes of current decay

We have shown that pulsed bias effectively overcomes current decay in ambient conditions, resulting in stable EL with good quantum efficiency. We now study the causes of this current decay. As mentioned before, current decay at fixed bias is related to hysteresis in I_d/V_g sweeps. Indeed, sweeping the gate voltage faster also reduces hysteresis in our devices (Fig. 54). Although few reports directly study current decay, there has been extensive work on hysteresis in TMDC FETs,

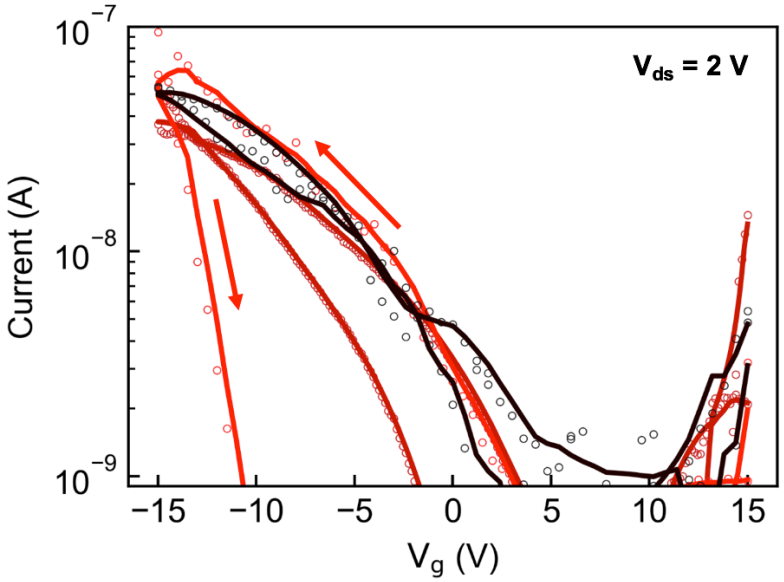

Figure 54. I_d-V_g curves for monolayer WSe_2 FET for various sweep rates. From red to black: 1.8 V/s, 8.9 V/s, 163 V/s.

To distinguish between environmental causes of current decay we studied the device in vacuum ($3x10^{-5}$ Torr) and after annealing at 140 C for 2 hours to remove adsorbates, followed by cooling back to room temperature. The current under electron injection (V_{ds} = 1V, V_g = 8V) becomes highly stable while the hole current (V_{ds} = 1V, V_g = -10V) still decays (Fig. 55a). In ambient conditions for the same device, both electron and hole currents decay similarly (Fig. 55b). In addition, the I_d/V_g curve shows decreased hysteresis in vacuum, and a shift in threshold voltage for electrons but not for holes (Fig. 56). Therefore, we attribute the current decay in ambient to both adsorbed molecules on the surface of the monolayer, as well as additional hole traps that remain after removing adsorbates, possibly due to interface traps or intrinsic defects [64, 120].

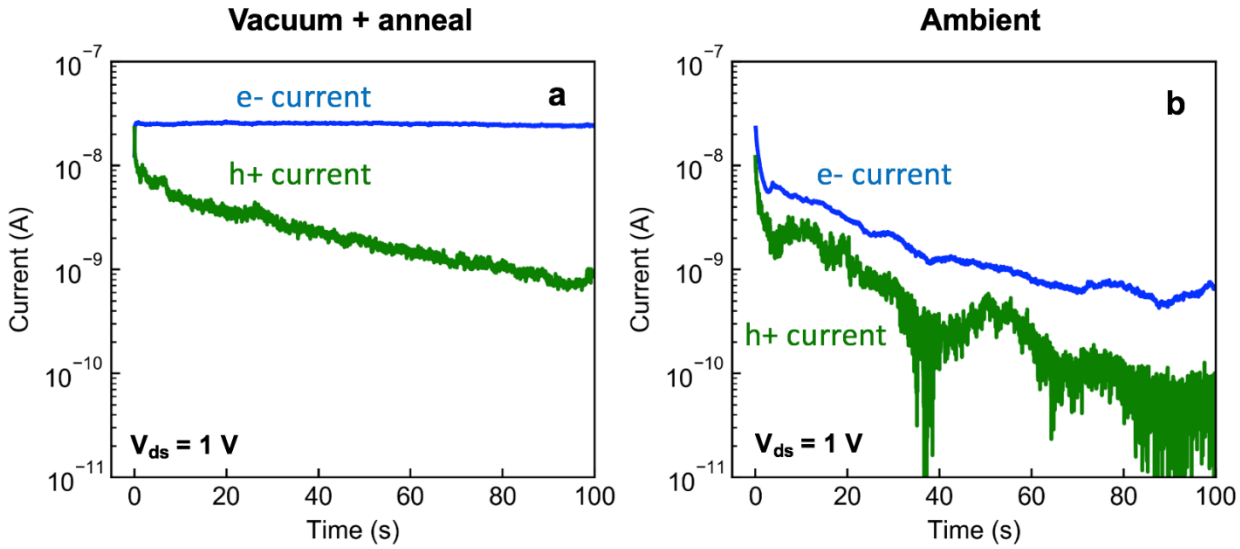

Figure 55. (a) Current decay in vacuum (10^{-5} Torr) and after annealing (140 C), for electrons (blue) and holes (green). (b) Current decay in ambient conditions, for electrons (blue) and holes (green).

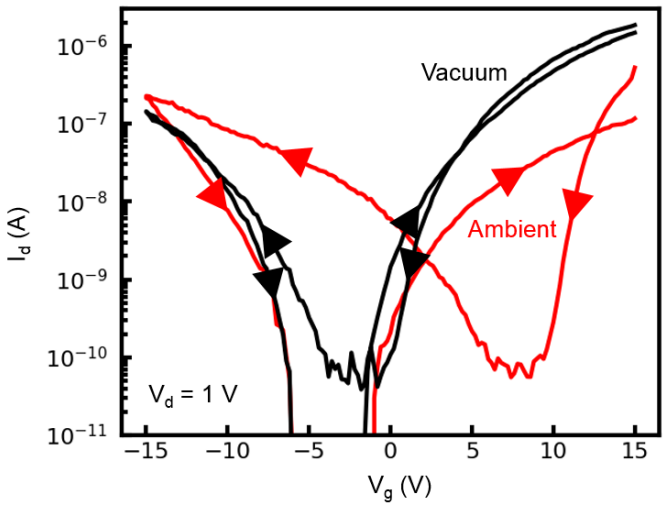

Figure 56. I_d-V_g curve in vacuum and ambient conditions.

This shows that pulsing is still necessary in vacuum to obtain stable bipolar current injection. In air, H_2O and O_2 are the primary constituents possibly responsible for current decay. To test the relative contributions of H_2O and O_2 on the device, we measured hysteresis in ambient air, dry air (21% O_2, 79% N_2), and pure N_2 (Fig. 57). The hysteresis for both electrons and holes is higher in ambient than the other cases, while almost identical for dry air and pure N_2. Therefore, adsorbed water is likely the primary factor affecting the device in ambient conditions, similar to MoS_2 FETs [61, 62].

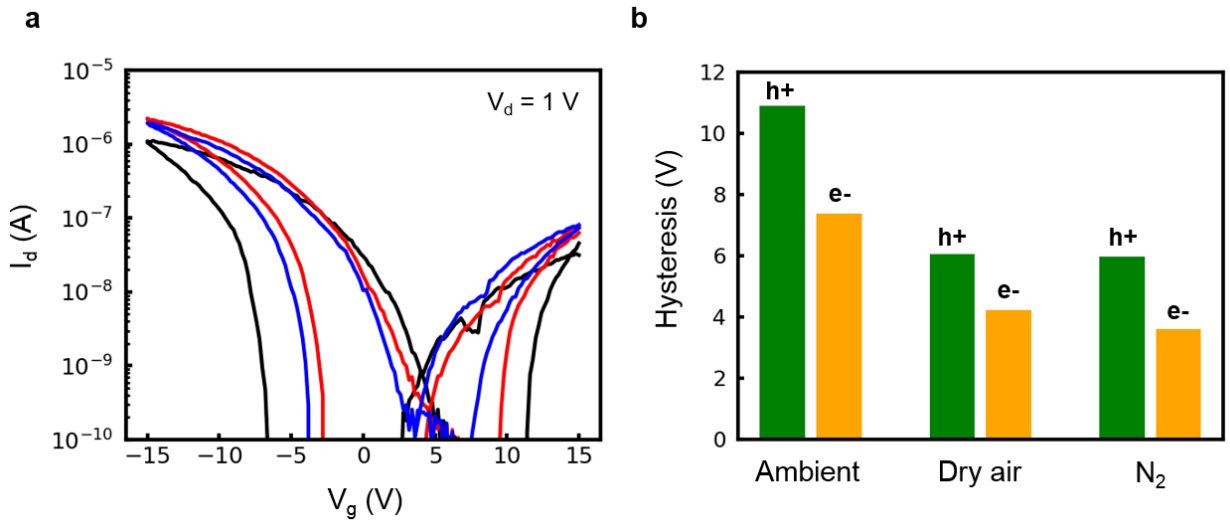

Figure 57. Hysteresis in ambient conditions, dry air (79% N_2, 21% O_2), and pure N_2. (a) I_d-V_g curves. Black: ambient, red: dry air, blue: N_2. (b) Hysteresis voltage between upsweep and downsweep, for holes (h+) and electrons (e-). Hysteresis is measured at I_d = 1 nA.

In conclusion, we have shown that the hysteresis and current decay commonly seen in TMDC transistors also play an important role in light-emitting diodes. Pulsed injection is an effective way to circumvent this issue, yielding bright and stable EL using a simple back-gated FET structure, with efficiency near that of PL. We show how to extract the optimal bias condition for efficient bipolar injection, and study the high frequency behavior of light emission. A fast ~15 ns rise/fall time is observed, indicating strong potential for high speed light modulation. Pulsed emission is stable over hours of operation. Further improvements in efficiency will come from contact optimization to enable lower voltage operation, as well as advances in CVD growth to improve intrinsic material quality. Higher speed can be obtained by coupling to an optical cavity to enhance spontaneous emission rate [33, 36, 85, 121].

5 Electrically-injected antenna coupled WSe_2 emitters

Now we turn to antenna coupling of electrically-injected light emitting devices. We first present results on coupling large-area devices to isolated bowtie antennas. Some evidence of enhancement is observed, but enhancement is difficult to quantify due to the small area fill factor of the antenna feedgap compared to the total monolayer size. This motivates the switch to antenna arrays with higher fill factor. We demonstrate slot antenna arrays coupled to electrically injected WSe_2 light-emitting capacitors, with very high polarization ratios >30x. Finally, to achieve high efficiency together with high enhancement, we combine the pulsed single-gate light-emitting diode presented in Chapter 4 with nanosquare antenna arrays, and show >10x higher intensity for antenna-coupled devices.

5.1 Double-gate LED with bowtie antennas

As mentioned in Chapter 2, one common structure for electroluminescence in TMDCs is the double-gate LED, with two separate back gates for electrostatic doping of P and N to form a P-I-N junction. We can easily incorporate antennas into the intrinsic region of this structure by including them in the same metal deposition step as the gates. Fig. 58a shows the device operating mechanism. A negative voltage V_{gp} on the P back gate dopes the P side, while a positive voltage V_{gn} on the N back gate dopes the N side. In the off state, the source-drain voltage $V_{ds} = 0$, while in the on state a positive V_{ds} injects electrons and holes into the center "intrinsic" region where light is emitted. Fig. 58b shows the schematic of the antenna-coupled device. We use hexagonal boron nitride (hBN) as an atomically smooth gate dielectric atop gold back gates. Pt and Ni are used for P and N contacts respectively. Bowtie antennas are deposited between the back gates in the same deposition step. An aluminum back mirror provides additional light directivity.

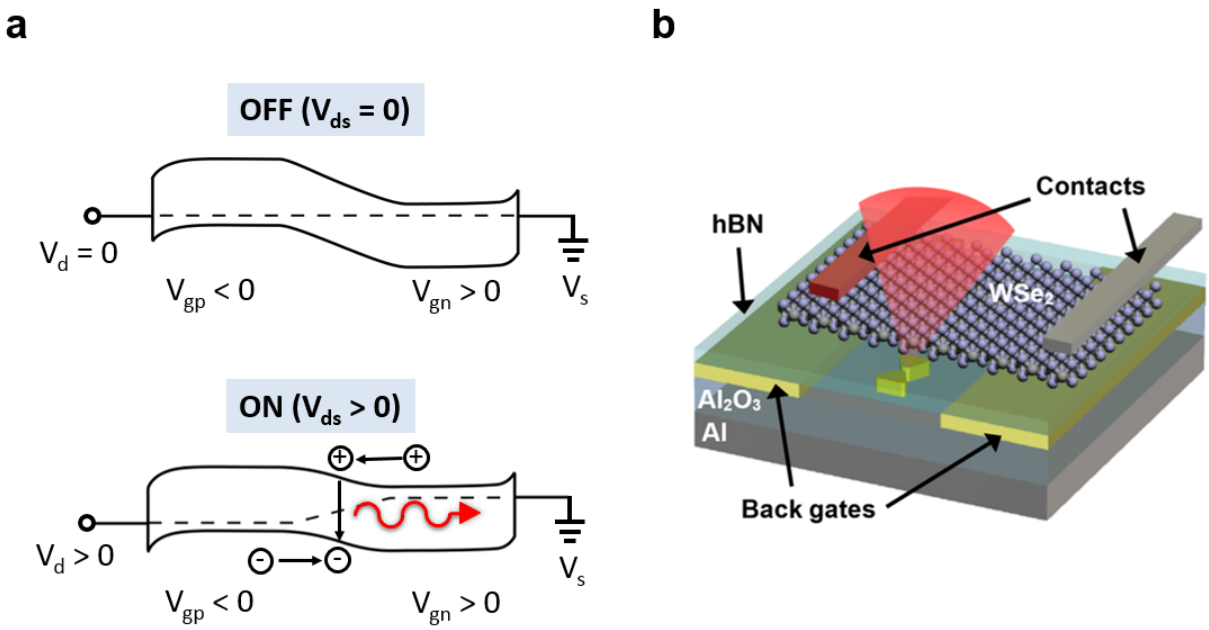

Figure 58. a) Device band diagram in off state ($V_{ds} = 0$) and on state ($V_{ds} > 0$). b) Device schematic with bowtie antennas between back gates.

The fabrication flow is as follows. First, 60 nm Al is evaporated onto a Si substrate, followed by 100 nm Al_2O_3 deposited using ALD. 15 nm Au back gates and bowtie antennas and patterned and evaporated using e-beam evaporation. 6 nm hBN is transferred atop the gates using the dry transfer process described in Chapter 4, followed by the WSe_2 monolayer. Finally, Pt hole contacts are patterned and evaporated, and Ni electron contacts are also patterned and evaporated. Fig. 59 shows an image after the WSe_2 transfer step. The WSe_2 shows very little contrast with the substrate so is not easily visible. Four bowtie antennas were placed between the gates and are visible in the microscope image.

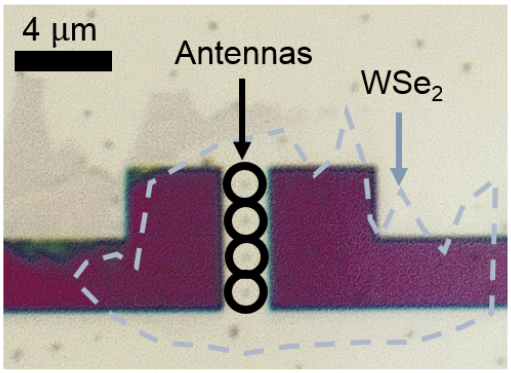

Figure 59. Optical microscope image of double-gate antenna device after transfer of WSe_2.

Bowtie antennas are simulated using FDTD to find theoretical rate enhancement for both polarizations. Fig. 60a shows the emission rate enhancement at resonance for both antenna and

perpendicular polarizations. A peak enhancement of ~100x is found at the hotspot. In addition, enhancement exists at the sharp edges of the bowtie, for both antenna and perpendicular polarization. Thus, bowties may be more promising than dipoles if enhancement at both polarizations is desired. Fig. 60b shows scanning electron micrographs of the fabricated bowties. Gap widths of ~10 nm are achieved.

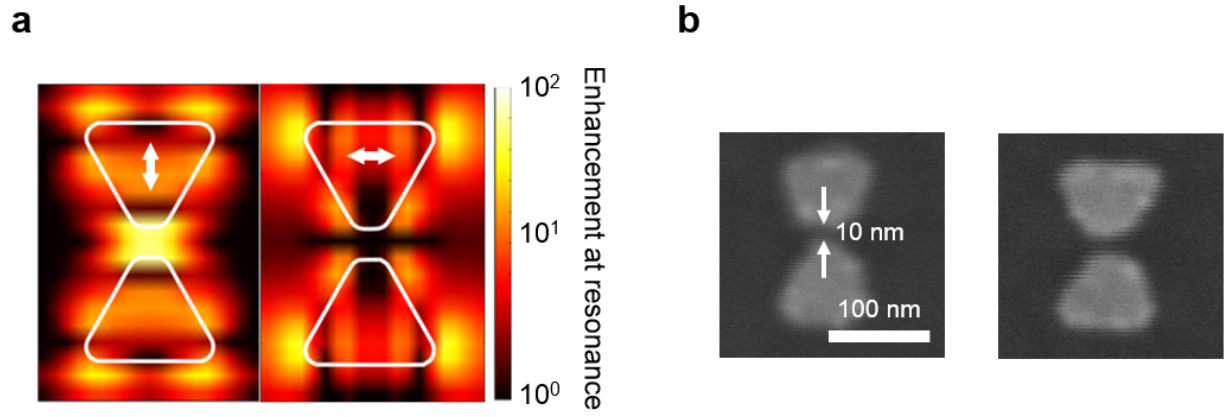

Figure 60. a) Simulated emission rate enhancement spatial map for antenna (left) and perpendicular (right) polarizations. b) SEM of fabricated antennas.

Dark field scattering was performed on the antennas to verify their resonance properties. The dark field setup is shown in Fig. 16. White light from a halogen lamp is incident on a patch stop to block the center of the beam, and reflected onto the sample. Reflected light is then filtered so that only scattered light passes through the linear polarizer to the Si spectrometer. To correct for the scattering from the bare substrate, the spectra are then processed using the formula:

$$S_{norm}(\lambda) = \frac{S_{ant}(\lambda) - S_{bg}(\lambda)}{S_{white}(\lambda) - S_{off}(\lambda)} \tag{59}$$

where S_{norm} is the final normalized spectrum, S_{ant} is the measured scattering from the antenna, S_{bg} is the scattering from the substrate, S_{white} is the scattering from an ideal Lambertian scatterer (white paper used in this case), and S_{off} is the scattering when the light source is off. Fig. 61 shows the normalized spectra for four sample bowtie antennas, for both antenna polarization (blue solid lines) and perpendicular polarization (red dashed lines). A broad resonance peak is observed in most cases, with matching resonance wavelength for both polarizations. Note that the perpendicular polarization also shows significant scattering comparable to the antenna polarization, in general agreement with simulation (Fig. 61). The peak is centered around 700 – 750 nm, close to the target luminescence wavelength of 750 nm.

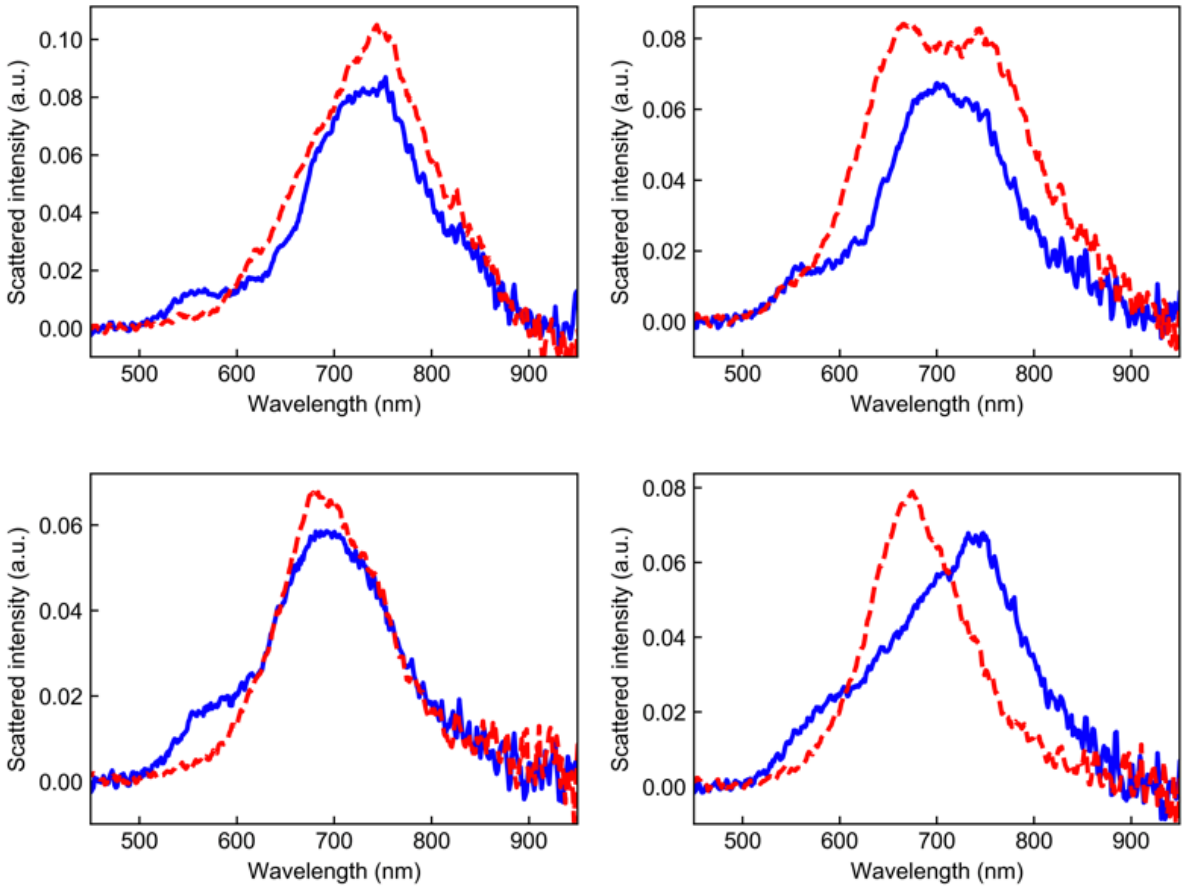

Figure 61. Scattering spectra for four different bowtie antennas, in antenna polarization (blue solid lines) and perpendicular polarization (red dashed lines).

Light emission is observed when the device is biased at >100 nA. The L-I curve is shown in Fig. 62. EL intensity is very weak for low current, and grows exponentially with current. Note that the device was not pulsed here, so light emission is weak and decays rapidly. Fig. 63 shows a 2D map of light emission versus position along the width of the channel (vertical axis) and wavelength (horizontal axis). Three distinct peaks are observed with the same positional spacing (1.5 μm) as the antennas. Thus, we attribute this light emission to antenna enhancement. The extracted peaks are plotted on the right, and occur at the typical A exciton wavelength of 750 nm.

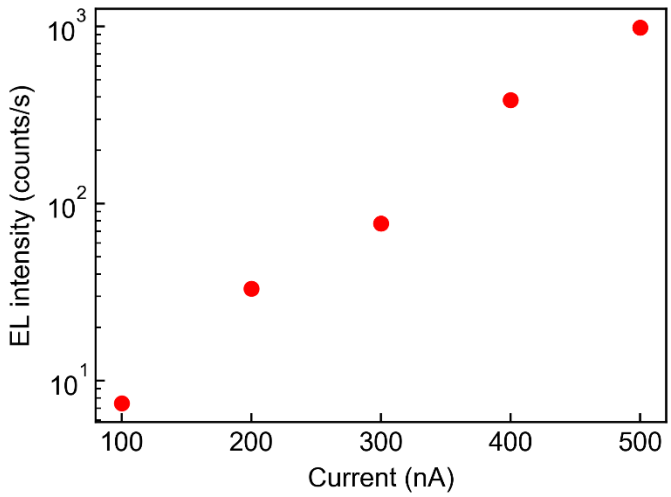

Figure 62. L-I curve for double-gate device.

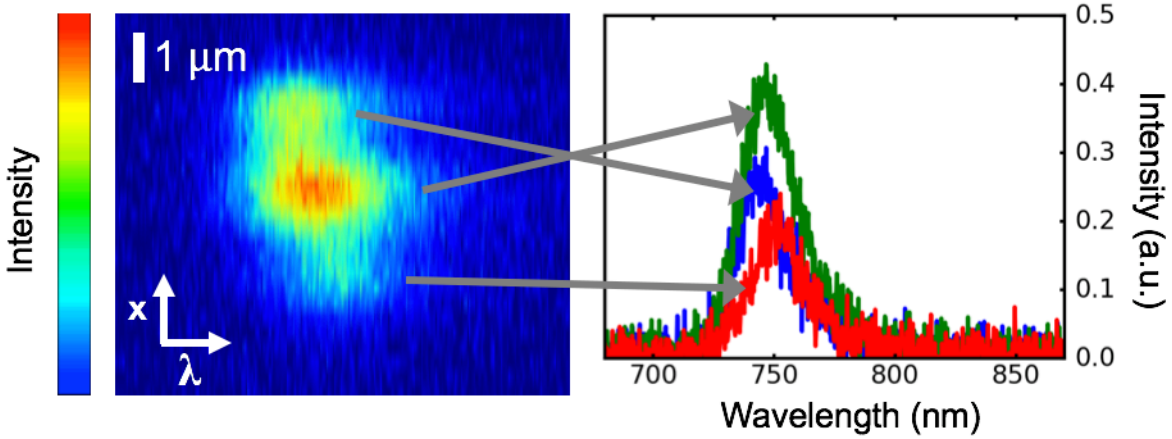

Figure 63. Left: 2D map of EL intensity versus position (vertical axis) and wavelength (horizontal axis). Right: extracted spectra.

Although some indications of antenna enhancement were observed, it is difficult to quantify the enhancement due to the small areal fill factor of the antennas and the optical resolution limit. Assuming the feedgap of each antenna is ~20 nm x 40 nm = 800 nm^2, and the size of the intrinsic region is 1 μm x 4 μm = 4 μm^2, the fill factor is a mere 0.08%. Thus, to quantify rate enhancement, it is important to either shrink the device to the size of a single antenna, or use dense antenna arrays with high fill factor.

5.2 Light-emitting capacitor with slot antenna array

The light-emitting capacitor was introduced in Chapter 2 as a simple way to achieve electroluminescence in TMDCs. By applying pulsed voltage to a capacitor structure, electrons

and holes are injected in alternating cycles and recombine to emit light. One way to integrate this structure with an antenna array is by embedding slot antennas in the contact, as in Fig. 64. By a self-aligned etching process that removes the WSe_2 not covered by the contact, the emission is confined under the contact and should only occur in the antenna feedgaps. Upon applying pulsed bias, light is emitted downward through the Al_2O_3 gate oxide and the ITO back gate.

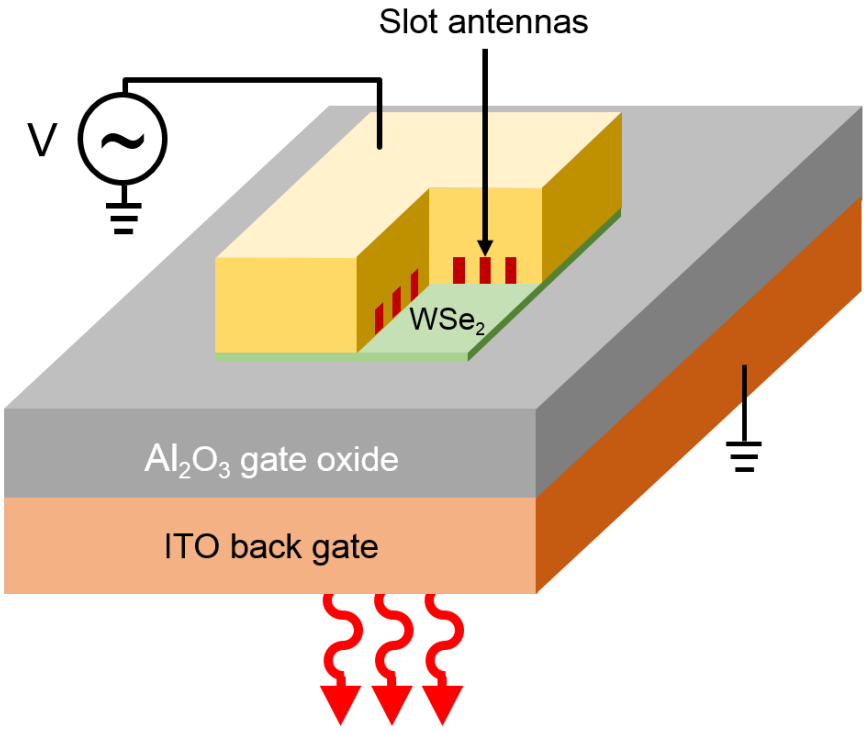

Figure 64. Schematic of light emitting capacitor with slot antenna array.

To fabricate the slot antennas, it is desirable to avoid electron-beam lithography directly on the monolayer, since the electron beam can damage 2D materials [122]. This is especially important since the lithography is done directly where the active region lies, in the feedgap of the antennas. Therefore, we fabricate the contacts separately and then transfer them on top of the material. Transferred metal contacts have shown nearly ideal contact behavior free of Fermi-level pinning in MoS_2 [123]. To investigate the contact quality for monolayer WSe_2, we fabricate FETs using transferred gold contacts (without antennas) and measured I_d-V_g and pulsed EL characteristics. Au was chosen since it is chemically inert, so is not susceptible to oxidation during the transfer process. The Au contacts were patterned and deposited on an SiO_2/Si substrate, followed by liftoff in acetone. No adhesion layer was used. The Au adhesion was found to be sufficient to allow successful liftoff, while poor enough to allow transfer using the same pick-and-place process for monolayers, described in Chapter 4. After the transfer, the device is annealed for 2 hours at 130 C in a 200 Torr Ar atmosphere to improve contact adhesion. An image of the fabricated device is shown in Fig. 65a. The I_d-V_g curve is shown in Fig. 65b, with V_d = 1 V. The device showed p-type characteristics, with the magnitude of the current similar to contacts fabricated using conventional e-beam lithography and thermal evaporation (Fig. 54). Fig. 65c

shows a spatial map of EL when only the top contact is pulsed, with the bottom contact left floating. EL occurs around the edges of the contact, as expected.

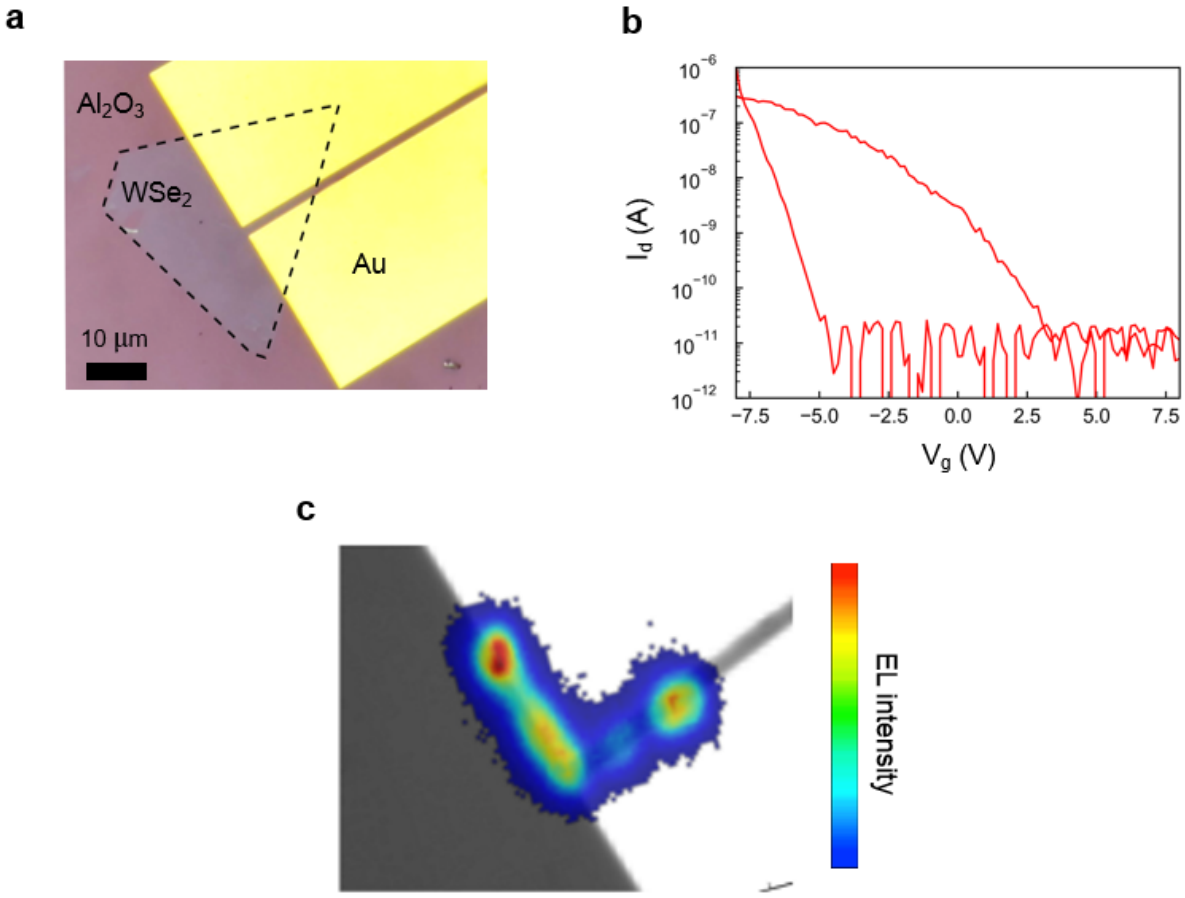

Figure 65. a) Optical microscope image of WSe_2 FET with transferred contacts. b) I_d-V_g characteristics with V_d = 1 V. c) Spatial EL map using pulsed injection with bias on top contact. The bottom contact is left floating, so no light is emitted next to it.

For the antenna devices, the slot antenna dimensions as designed were 240 x 20 nm, and the array spacing was 420 x 240 nm. Note that since the array spacing is subwavelength in both dimensions, no scattering is expected, due to the grating equation:

$$dn\sin(\theta) = m\lambda \tag{60}$$

where d is the array spacing, n is the refractive index of the substrate, m is the grating order and λ is the free-space wavelength. For d = 420 nm, n = 1.65, and λ = 750 nm, this gives $\sin(\theta) = 1.08$ for the first-order scattered wave. Thus, only the (0, 0) order scattering can be excited, i.e. reflection.

Slots are patterned with e-beam lithography using PMMA as a negative resist [124]. PMMA is typically a positive resist, but at very high doses it becomes relatively insoluble and can be used as a negative resist. Sub-20 nm features are easily achieved with negative PMMA (Fig. 66). Development is done using acetone at 70 C for 10 min. Heated development helps to reduce residue, as shown in Fig. 66.

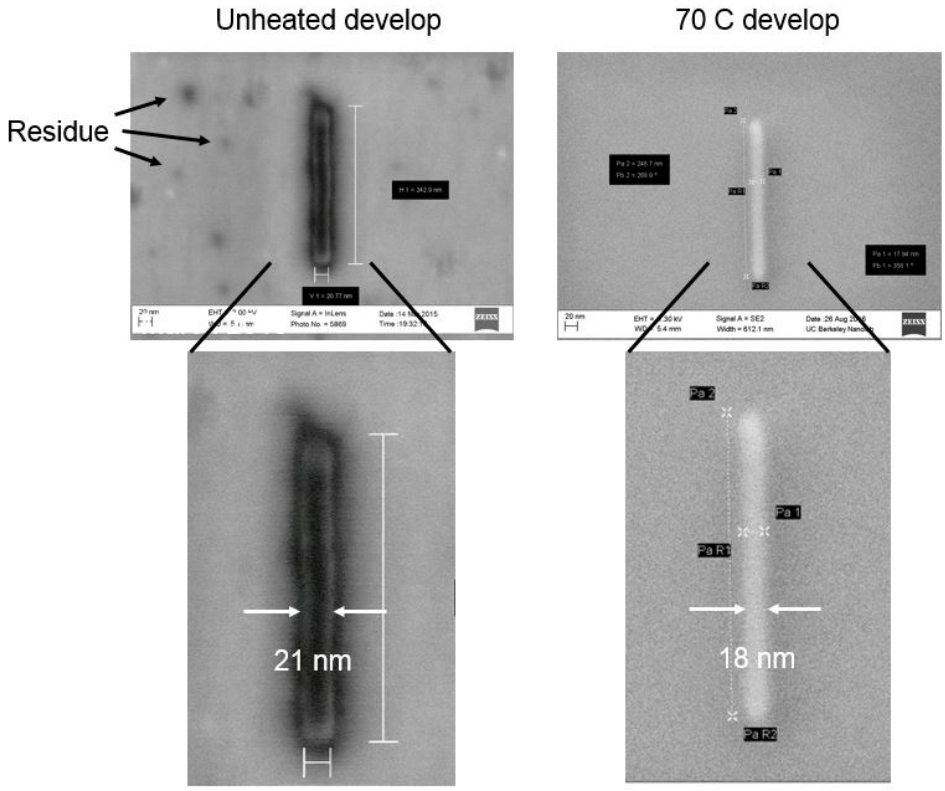

Figure 66. Scanning electron micrographs of PMMA ridges patterned using negative PMMA process. Left: unheated development in acetone, with visible residue near slot. Right: heated development at 70 C, with no visible residue.

After development, contacts are patterned on the array using e-beam lithography and gold is evaporated using angled evaporation to conformally cover the slots, followed by liftoff. Separately, CVD-grown WSe_2 on quartz is transferred onto a Al_2O_3/ITO gate stack identical to that used in Chapter 4. The slot antenna arrays are then transferred on top of the WSe_2 using the same transfer process. EL is measured under pulsed voltage before and after etching, for both antenna and perpendicular polarizations. Fig. 67a,b shows EL spatial maps under pulsed voltage of 4.5 V at 5 MHz. Before etching, emission occurs mainly in the region adjacent to the contact for both polarizations. The polarization ratio $P = I_{ant} / I_{perp}$ is 2.5, likely due to scattering from the edge of the metal contact. The spectra for both polarizations is also identical (Fig. 67c).

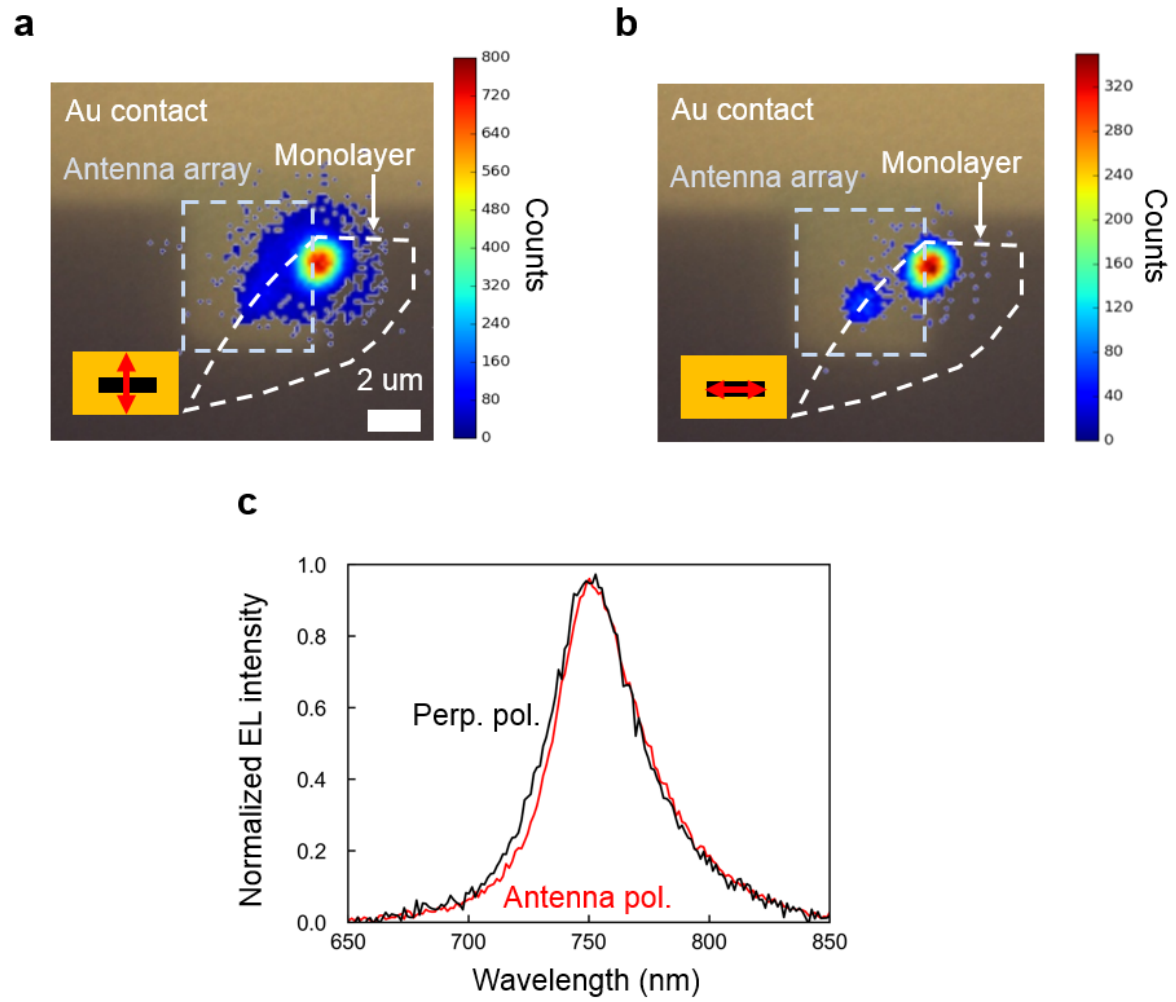

Figure 67. EL before etching. a, b) EL spatial map overlaid on optical image of device, for antenna polarization (a) and perpendicular polarization (b). c) Normalized EL intensity for both polarizations.

After this, the WSe_2 not covered by the array is etched using vapor XeF_2, completing the fabrication. Fig. 68a,b shows the EL spatial maps for both polarizations after the etch, under pulsed bias of 6.5 V at 5 MHz. Bright EL is observed in the antenna polarization, while the EL in the perpendicular polarization is below the noise floor (note scale bar in Fig. 68b). Thus, we estimate a polarization ratio of >30x. Fig. 68c shows the EL spectra in the antenna polarization before and after the etch. A clear peak shift is observed, showing that the antenna is modulating the emission spectrum of EL.

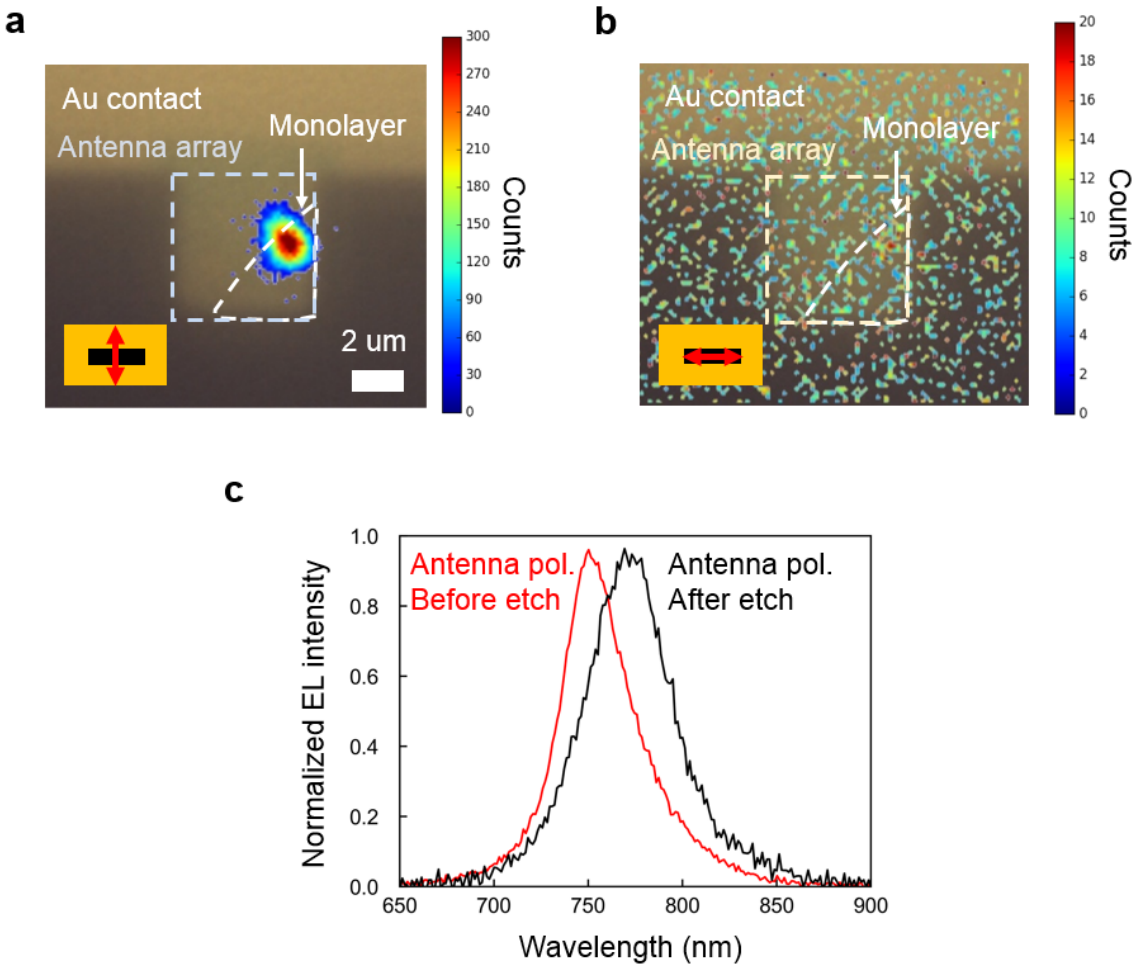

Figure 68. EL after XeF_2 etching. a, b) EL spatial map overlaid on optical image of device, for antenna polarization (a) and perpendicular polarization (b). c) Normalized EL intensity for antenna polarization before and after etch.

These results show that the slot antenna array integrated with light-emitting capacitor is effective for injecting carriers mainly inside the antenna feedgap and significantly enhancing the spontaneous emission rate, as shown by the extremely high polarization ratio. However, due to the small active region and the unipolar injection mechanism of the LEC, most of the injected carriers diffuse back into the contact quickly before recombining, so the device efficiency is rather poor. A high voltage (6.5 V) is needed to observe significant light emission, and the device dimmed quickly after ~10 min measurement, likely due to device heating. For higher efficiency and more controllable electrical modulation, bipolar injection using light-emitting diodes is still needed. Therefore, we now discuss integrating antenna arrays with the pulsed LEDs introduced in Chapter 4.

5.3 Single-gate LED with square antenna array

Integrating an antenna array with an electrically-injected device while preserving high efficiency presents some challenges. First, as mentioned in the previous section, it is not desirable to have metal directly contacting the monolayer, since that will cause loss of carriers into the metal. An insulator is needed to separate the antenna from the monolayer. This insulator should be thick enough to suppress leakage if a field is applied across it, such as in a gate dielectric. At the same time, close proximity to the metal is desired for high antenna enhancement. Thus, there is a tradeoff between high antenna enhancement using a thin oxide, and low leakage using a thick oxide. Fig. 69a shows the simulated enhancement spectra for a cavity-backed slot antenna with varying thickness of an Al_2O_3 spacer above the feedgap. The spectrum redshifts slightly with higher spacer thickness due to higher effective index surrounding the antenna. More importantly, enhancement decreases rapidly with oxide thickness, as shown in Fig. 69b.

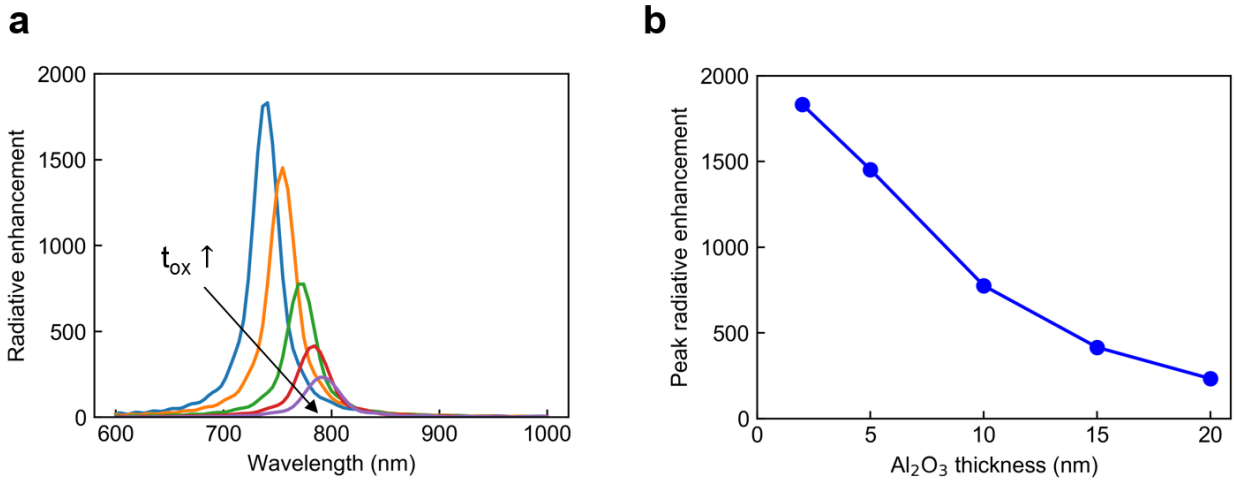

Figure 69. a) Simulated radiative rate enhancement for a cavity-backed slot antenna with varying spacer thickness t_{ox} between the feedgap and the dipole. b) Extracted peak enhancement versus spacer thickness.

On the other hand, thin gate oxides suffer from leakage at high voltage. Due to the Schottky contacts in our LEDs, high voltage across the channel (V_{ds} ~ 8 V) is still required to overcome the Schottky barrier and allow sufficient current injection. Fig. 70a plots the leakage current density of a metal-insulator-metal (MIM) capacitor using a Ni/Al_2O_3 (5 nm)/ITO stack. Reasonable agreement is found with literature values for 6 nm Al_2O_3 grown on GaAs [125]. WSe_2 diodes using this gate oxide were fabricated alongside the capacitors, with the standard structure presented in Chapter 4 (Fig. 34). Although the leakage current is relatively low in a single-sweep measurement of Fig. 70a, it was found that in the LED devices, applying $V_{ox} > 2$ V caused oxide breakdown after a few measurements. However, the maximum current for $V_p = 2$ V and $V_n = -2$ V was only ~1 nA (Fig. 70b).

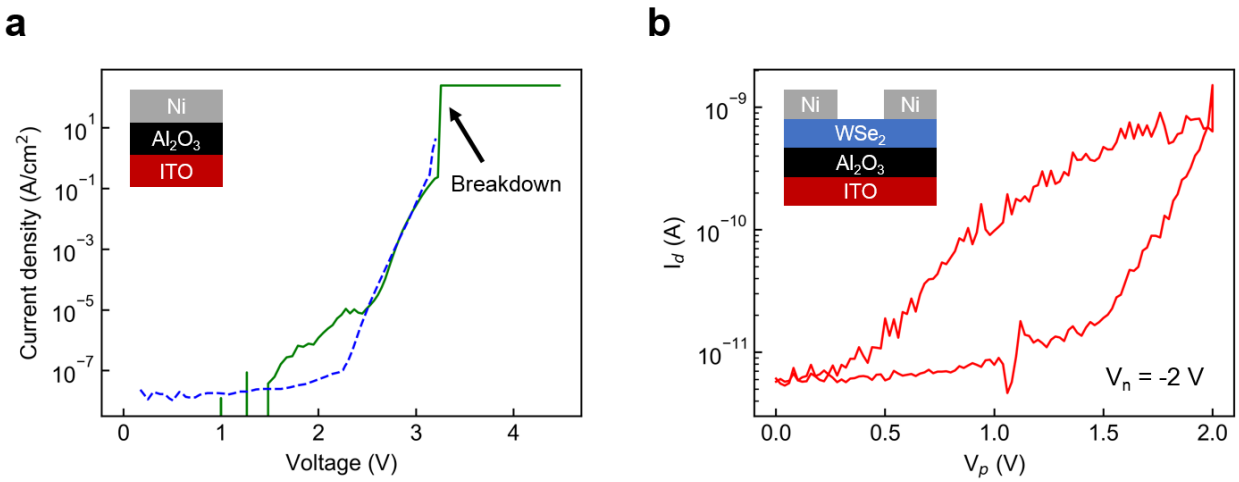

Figure 70. a) I-V curve of fabricated Ni/Al_2O_3 (5 nm)/ITO MIM capacitors (green solid line) with comparison to [125] (blue dashed line). b) I_d versus V_p of WSe_2 LED device using the same gate oxide, with V_n = -2 V.

Therefore, either contact optimization is needed to enable low voltage operation, or the source-drain voltage must be separated from the gate voltage. As discussed in Chapter 3, although many doping methods exist for monolayers, it is challenging to make good P and N contacts simultaneously to the same material in the same device. One simple way to separate V_{ds} from V_g is by separating the antenna layer from the gate by a capacitive divider (Fig. 71a). The antenna array consists of electrically isolated metal regions and is covered by a thin gate oxide. The antenna metal and gate metal form a vertical capacitive divider with the voltage dropped as $V_{top}/t_{top} = V_g/t_g$, where V_{top} is the voltage across the top oxide, t_{top} is the thickness of the top oxide, V_g is the voltage across the gate oxide, and t_g is the thickness of the gate oxide (Fig. 71b). For a thick gate oxide and thin top oxide, the top voltage V_{top} is now low while the total source-drain voltage V_{ds} can be high. Note that this requires the antennas to be electrically isolated at least once along the channel, or the antenna array will form a continuous gate itself and the structure would be the same as using a thin gate oxide.

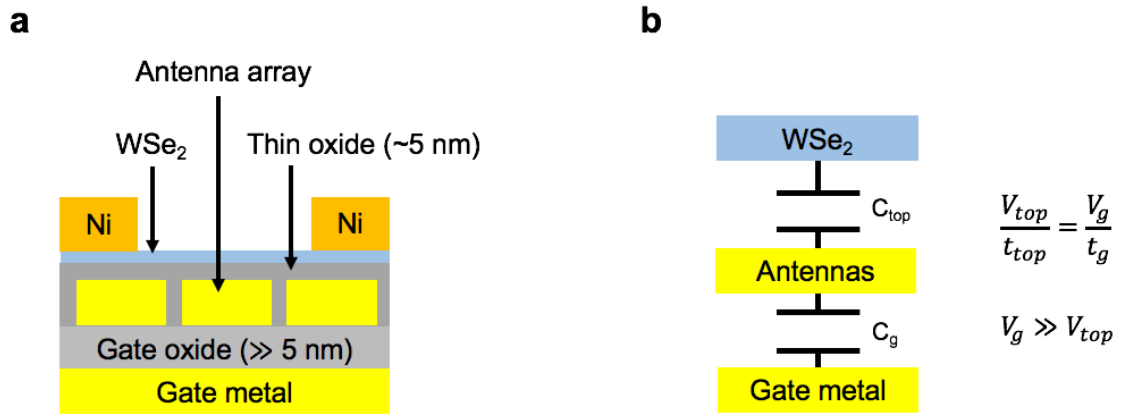

Figure 71. a) Schematic of antenna-coupled LED design with low gate leakage and high enhancement. b) Capacitive divider to avoid high voltage across thin top oxide.

We implement this design using a nanosquare array, shown in Fig. 72. The primary antenna mode occurs in the gaps of the array, and by varying the pitch and antenna gap the resonance wavelength can be tuned. The antenna mode is either a dipole-like mode when the pitch is small, or a 3rd-order slot-like mode when the pitch is large (Fig. 73a,b). Due to the close proximity of the antennas, the mode couples to adjacent antennas, spreading out the mode and decreasing enhancement. However, the fill factor is much higher than isolated antennas: ~26% for the as-designed 210 nm pitch array with 30 nm gaps. The power radiated into the top half-space by a dipole in the antenna gap relative to a dipole on the bare substrate reaches ~20 for the 1st order mode and ~17 for the 3rd order mode (Fig. 73c).

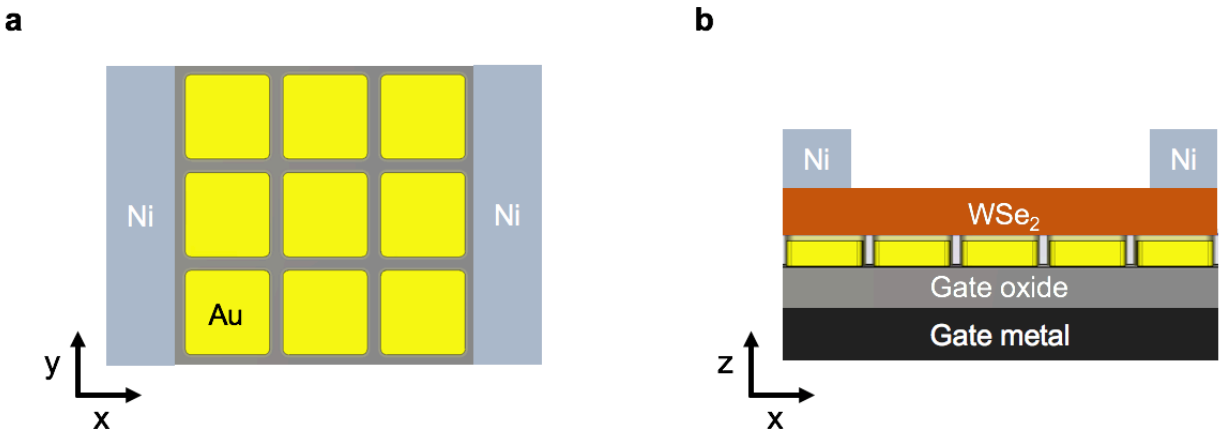

Figure 72. Schematic of nanosquare antenna array device. a) Top view. b) Side view.

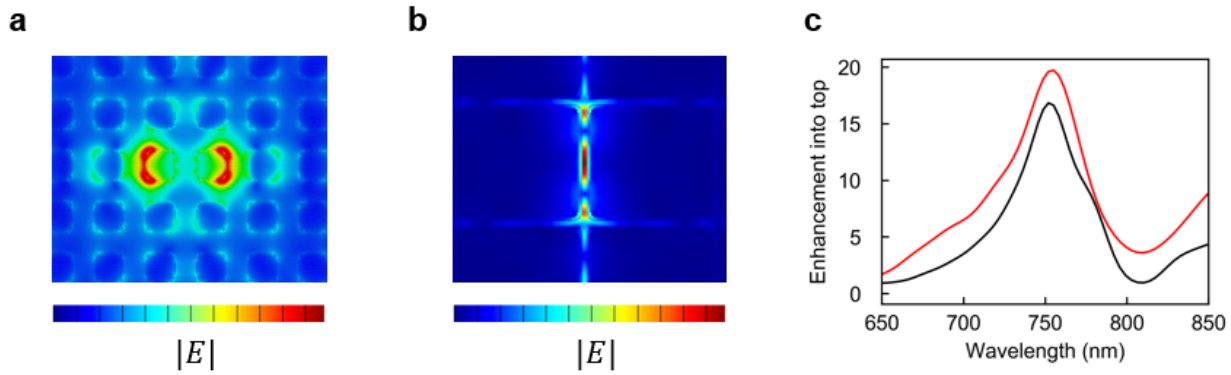

Figure 73. a) Mode profile of square array with 75 nm pitch at 1st order resonance ($\lambda = 750$ nm). b) Mode profile of square array with 210 nm pitch at 3rd order resonance. c) Enhancement into top half-space relative to bare substrate, for mode in (a) (red) and mode in (b) (black).

The fabrication process starts with the Al_2O_3 (20 nm)/ITO (280 nm)/glass gate stack used in the previous section. The antennas are patterned using e-beam lithography followed by e-beam evaporation of Ge (0.3 nm)/Au (20 nm) and liftoff. WSe_2 is then transferred atop the antennas, and Ni contacts (15 nm) are patterned and deposited with thermal evaporation.

To estimate rate enhancement, we compare the EL intensity for an antenna-coupled device with the intensity for a detuned array with the same fill factor. The detuned array is scaled up by 3x in each dimension (630 nm pitch with 90 nm gap). Fig. 74a, c shows optical images of the detuned and on-resonance arrays respectively, after WSe_2 transfer but before contact deposition. Fig. 74b, d show spatial maps of EL for both arrays.

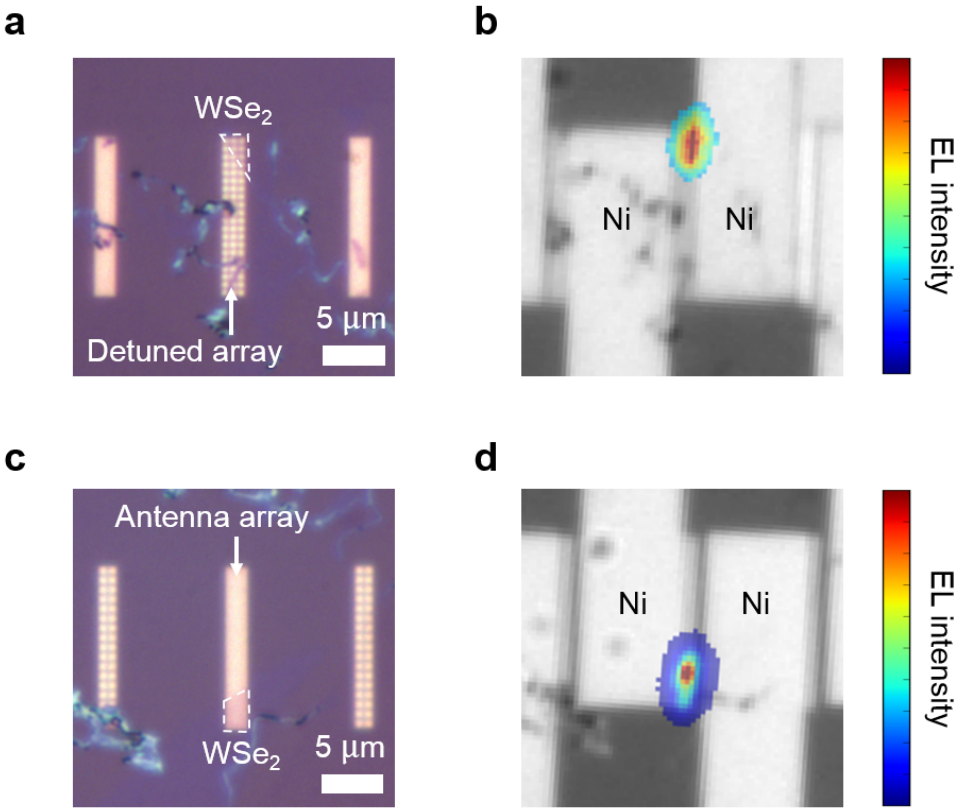

Figure 74. a,c) Optical microscope images of WSe_2 on detuned antenna array and on-resonance antenna array. b,d) Spatial EL maps for both arrays.

Both devices show bright light emission. However, the EL IQE for the on-resonance array is ~1%, while the IQE for the detuned array is ~0.1%. This IQE is similar to that observed with previous devices on the bare Al_2O_3 substrate, since acetone treatment has no effect on this substrate (Fig. 37) resulting in ~10x lower observed QY. The spectra normalized to injection current are compared in Fig. 75. We attribute the ~11x brighter emission of the on-resonance array to antenna enhancement. This high-fill-factor array structure thus provides effective spatially-averaged enhancement for large-area devices, and is an important step in realizing efficient electrically-injected nanoLEDs.

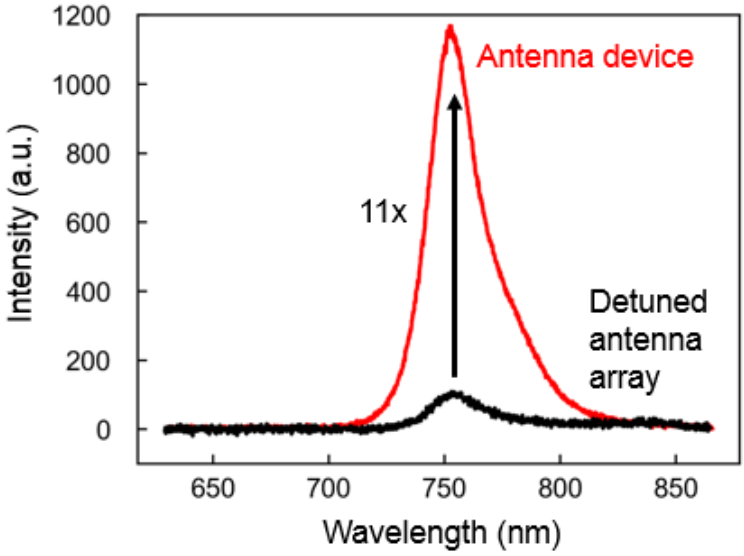

Figure 75. Comparison of emission spectra normalized to injection current for on-resonance array (red) and off-resonance (detuned) array (black).

6 High-speed modulation of TMDC nanoLEDs

In this chapter we discuss the challenges of achieving high-speed and high efficiency TMDC nanoLEDs, building on what we have discussed in past chapters. As mentioned in Chapter 3, the intrinsic radiative lifetime of excitons is ~1 ns at room temperature, so the modulation speed is limited to <1 GHz. Thus, to achieve speeds in the 10s to 100s of GHz, coupling to an optical antenna with high rate enhancement is required. The first consideration is whether to use an antenna array or a single antenna. The main tradeoffs are as follows:

1) **Waveguide coupling efficiency.** Using a single-mode waveguide is desirable since typical silicon photonic multimode waveguides suffer from high modal dispersion [126], ultimately limiting bandwidth. However, it is not possible to perfectly couple the multiple modes of an antenna array into a single mode due to the second law of thermodynamics; in fact, the maximum coupling efficiency from N modes to 1 mode is simply $1/N$ [127].
2) **Mutual antenna coupling.** The mutual coupling between closely spaced antennas will spread out each antenna mode and greatly decrease peak enhancement, as we have seen in Chapter 5.
3) **Carrier confinement.** The main challenge of using a single antenna is carrier and exciton confinement in a small active region. If the active region is made larger than the antenna, the fill factor is poor and average enhancement is low. For small active regions, carrier overshoot, exciton edge recombination, and exciton dissociation all decrease efficiency.

Due to the first two issues with using an antenna array, in this chapter, we focus on the single antenna device and investigate whether high efficiency can still be achieved with a small device size and high antenna enhancement. We perform device simulations to study exciton formation efficiency, and use a spatially-dependent rate equation model to study exciton diffusion and recombination. We also experimentally measure PL and EL efficiency of devices with varying channel length to verify some aspects of our model.

The general device design we simulate is shown in Fig. 76. The TMDC flake sits atop a single Ag cavity-backed slot antenna, separated by a thin back gate oxide. For concreteness in the simulations, we take it to be 5 nm Al_2O_3, although hBN may be more desirable as it is atomically smooth to reduce disorder. The antenna designed below is optimized for WSe_2 (~750 nm) since this is the most well-studied TMDC for bipolar devices. However, other TMDCs may be preferred, e.g. $MoTe_2$, which emits in the infrared (~1150 nm) and has a lowest exciton state which is bright [102]. The TMDC is contacted by graphene or metal electrodes (graphene shown here). The channel length L_c and the channel width W_c are varied in our design.

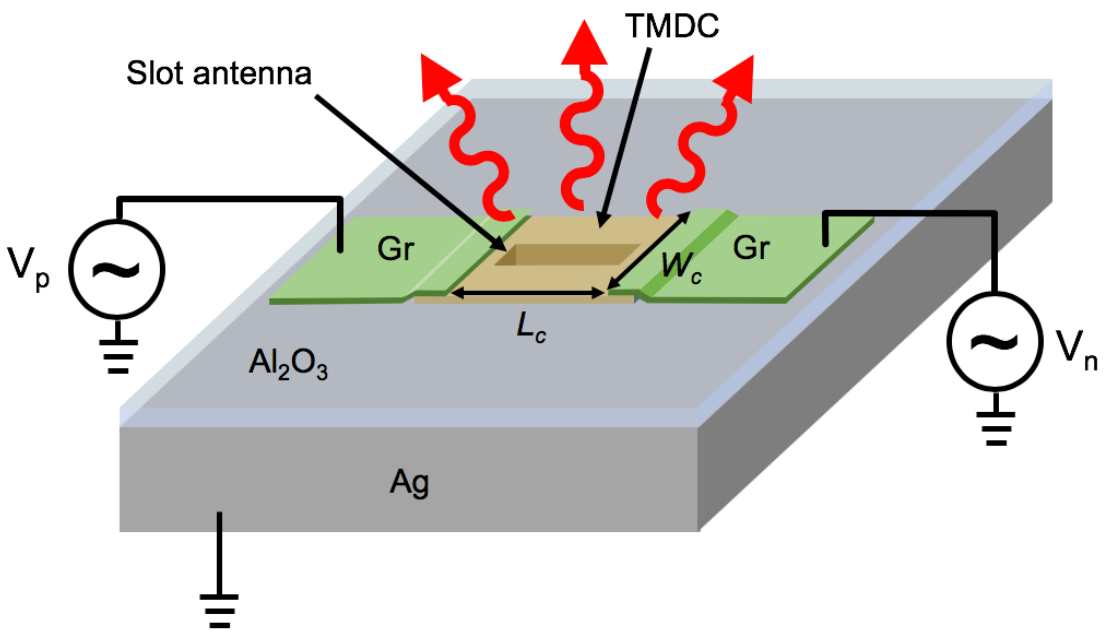

Figure 76. Schematic of TMDC nanoLED coupled to single slot antenna. The TMDC is separated from the Ag antenna by an Al_2O_3 back gate oxide.

The optimized cavity-backed slot antenna studied here is 140 nm x 20 nm in size with a depth of 96 nm. Simulation shows good resonance overlap with the intrinsic PL spectrum of WSe_2 (Fig. 77a). The peak radiative enhancement is ~1500 and peak non-radiative enhancement is ~1000, for a total of ~2500 peak rate enhancement (Fig. 77b), for a dipole at the center of the slot. Radiative enhancement is defined as the total enhancement times the fraction of power coupled to free space, while non-radiative enhancement is the fraction of power lost in metal. Thus, the antenna efficiency is ~60%.

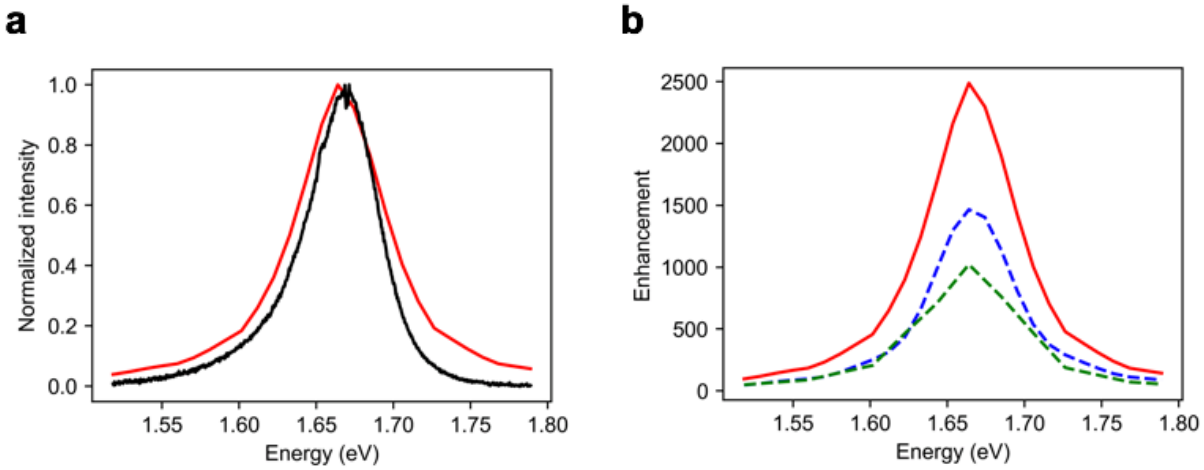

Figure 77. a) Normalized antenna enhancement spectrum (red) and PL spectrum of WSe_2 (black). Dipole is at the center of the slot with optimal polarization. b) Radiative enhancement

(blue dashed line), non-radiative enhancement (green dashed line) and total enhancement (red solid line).

As shown in Chapter 1, the overall enhancement is given by the weighted average over the intrinsic emission spectrum:

$$F_{avg} = \frac{\int R_0(E)F(E)dE}{\int R_0(E)dE} \tag{61}$$

This brings the enhancement down from ~2500x to ~1700x. An additional factor of 2 for polarization gives a final enhancement of 850x.

Light emission in TMDCs comprises two steps: exciton formation and exciton radiative recombination. We first study exciton formation using device simulations with varying channel length and material parameters. For small channel lengths, carrier overflow to the opposite contact is the main concern that limits exciton formation efficiency at low current density. At high current density, the $B_{ex}n^2$ exciton formation term dominates and efficiency is high.

After excitons are formed, exciton diffusion plays a central role in determining device efficiency and modulation speed. We introduce a spatially-dependent rate equation model for excitons and solve it for varying channel length and width.

Finally, we experimentally study the effect of channel length on PL and EL efficiency. We fit our data to an exciton diffusion model, and also perform photocurrent measurements to study the effect of exciton dissociation.

6.1 Exciton formation rate and efficiency

Exciton formation in TMDCs is extremely rapid due to the strong Coulomb interaction, with sub-ps exciton formation times measured in pump-probe studies. We derived the bimolecular exciton formation coefficient B_{ex} using the measured exciton formation time in Chapter 3, and obtained a conservative estimate of $B_{ex} \cong 0.1$ cm^2/s. Exciton formation competes with carrier overflow to the opposite contact, defining the injection efficiency:

$$\eta_{inj} = 1 - \frac{escaped\ carriers}{injected\ carriers} = 1 - \frac{|I_{pn}| + |I_{np}|}{|I_{pp}| + |I_{nn}|} \tag{62}$$

where I_{pn} is the p current on the n contact, I_{pp} is the p current on the p contact, etc. We perform 2D device simulations using Sentaurus TCAD to estimate the injection efficiency versus current density for various channel lengths L_c. In addition, we vary the Schottky barrier heights for the contacts, using either ϕ_b = 1 eV on both sides (ambipolar contacts, since E_g = 2 eV), or ϕ_b = 0

eV on both sides (Ohmic contacts). These are the worst-case and best-case scenarios respectively. The device schematic is shown in Fig. 79a. WSe_2 is contacted on the sides by voltages V_p and V_n, and gated by a 5 nm thick Al_2O_3 gate oxide. The material parameters are given in Table 1. Since reported mobilities for TMDCs vary widely (~1-100s cm^2/Vs), we test both 10 cm^2/Vs and 100 cm^2/Vs for both carriers.

First, we compare our model to measured I_d-V_g characteristics of WSe_2 FETs. We simulate a channel length of 1 μm and Al_2O_3 thickness of 20 nm to match our fabricated devices on ITO. We assume ambipolar contacts (ϕ_b = 1 eV). The result is shown in Fig. 78. The absolute on-current and degree of ambipolar behavior of measured devices varies widely depending on fabrication imperfections, but we observe reasonable agreement with simulation for our highest on-current devices (Fig. 78, black curve). The simulated mobility was found to have a negligible effect on current (1 vs 10 cm^2/Vs tested) since the current is limited by tunneling over the Schottky barriers. Thus, the magnitude of the current in our simulation seems to be generally realistic.

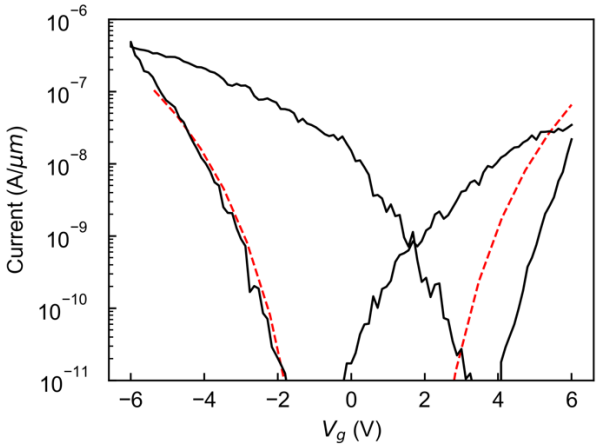

Figure 78. I_d-V_g characteristics for measured (black) and simulated (red) WSe_2 FETs, with V_{ds} = 1 V.

Next, we return to our device of interest, the nanoLED. The simulated band diagram for V_p = 3 V and V_n = -3 V is plotted in Fig. 79b, for ϕ_b = 1 eV and channel length of 160 nm. The field is strongest near the contacts due to the thinning of the Schottky barrier from the gate, with a relatively uniform field throughout the rest of the channel. The exciton formation rate is plotted in Fig. 79c. Most excitons are formed in the center of the channel, as expected. Although excitons are neutral particles, they may dissociate under high fields ~20 V/μm [128]. Fig. 79d plots the electric field for the same device. While the field is relatively uniform and small in the channel, the field near the contacts can easily exceed this value. Once the excitons dissociate, the high field near the P contact will quickly cause electrons to escape into the contact, and vice versa for the N contact. This is essentially another form of carrier overshoot that will greatly reduce the efficiency, as our experimental results will show.

Table 1. Material parameters for exciton formation simulation.

Parameter	Description	Value
E_g	Bandgap	2 eV [129]
m_e^*	Electron effective mass	0.5 m_0 [96]
m_h^*	Hole effective mass	0.5 m_0
B_{ex}	Exciton formation coefficient	0.1 cm^2/s
μ_h	Hole mobility	10 cm^2/Vs OR 100 cm^2/Vs
μ_e	Electron mobility	10 cm^2/Vs OR 100 cm^2/Vs
t_{ox}	Oxide thickness	5 nm

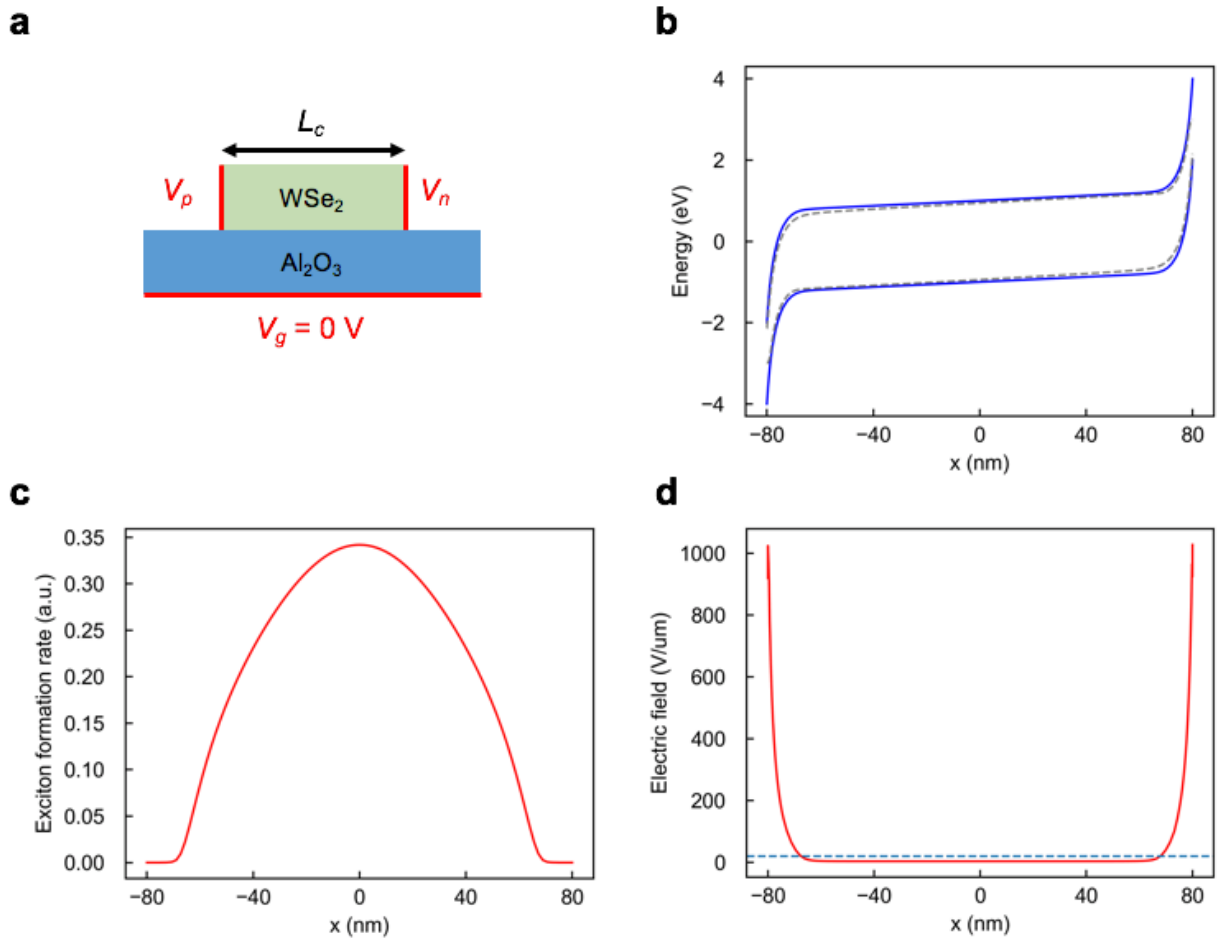

Figure 79. a) Device schematic for TCAD simulation. Red lines denote contacts. b) Simulated band diagram for a 160 nm device with 1 eV Schottky barriers, with V_p = 3 V, V_n = -3 V. c) Exciton formation rate for the same device. d) Electric field for the same device. Dashed line: exciton dissociation threshold.

The exciton formation efficiency versus current is plotted in Fig. 80 for different channel lengths. We test the effect of 10 cm^2/Vs mobility (a,b) and 100 cm^2/Vs (c,d) as well as ohmic (a,c) and Schottky (b,d) contacts. Both parameters have a large effect on injection efficiency. Highest efficiency is obtained with low mobility and ohmic contacts. Ohmic contacts help since the voltage and field are lower for a given current, so the carrier density is higher ($J_n = \mu_n n \frac{dF_n}{dx}, J_p = \mu_p p \frac{dF_p}{dx}$). For a typical channel width of ~100 nm and current of ~1 µA, the current density is ~10 µA/µm. The 100 nm long device has decent efficiency >40% at this current density for all models except (100 cm^2/Vs, $\phi_b = 1$ eV). Thus, it may be desirable to decrease mobility, by choosing an oxide with high charged impurity density for example [54]. However, care must be taken to not introduce extra trap states that cause increased non-radiative recombination.

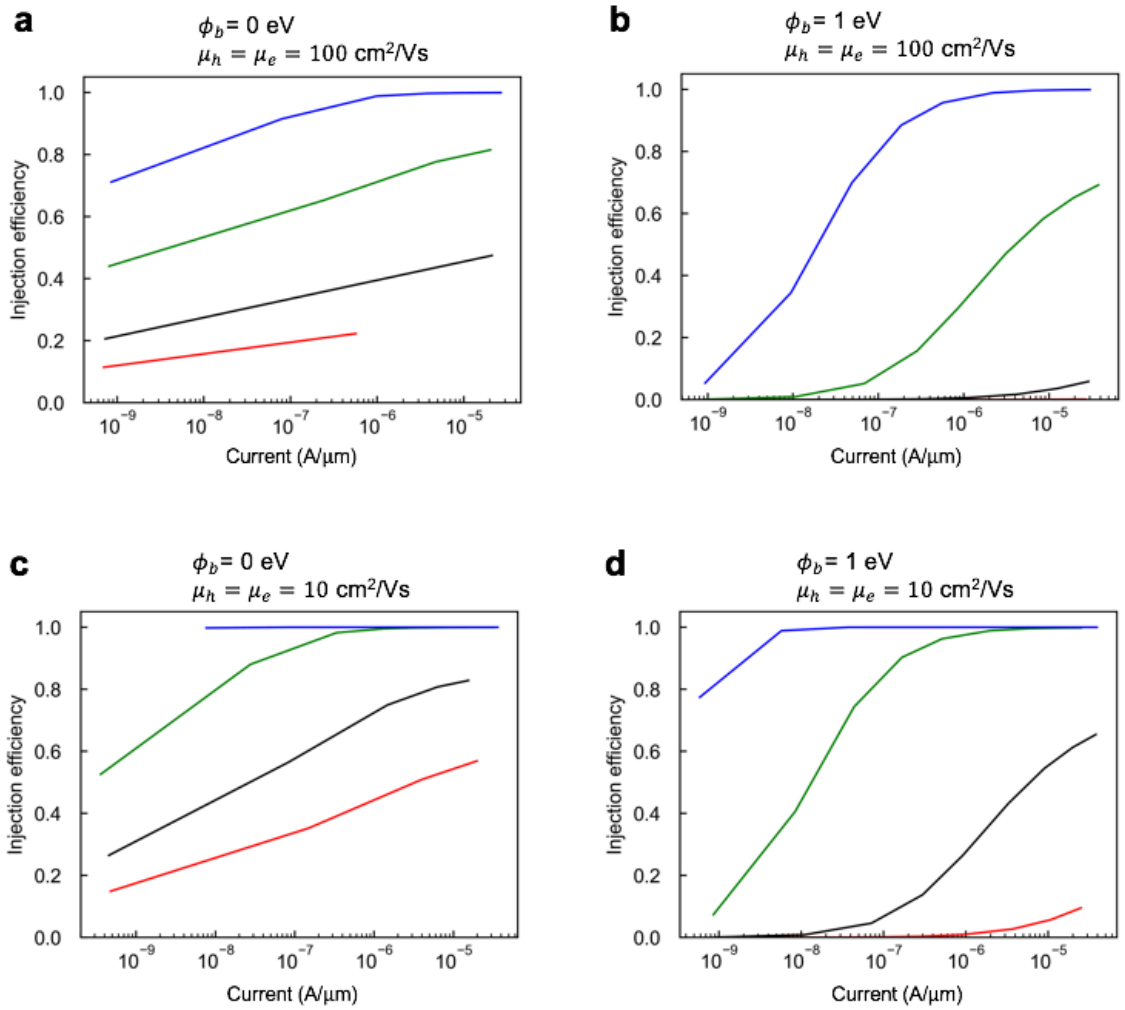

Figure 80. Injection efficiency versus current, for 100 cm^2/Vs mobility (a,b) and 10 cm^2/Vs (c,d) as well as ohmic (a,c) and Schottky (b,d) contacts. Red: L_c = 50 nm. Black: L_c = 100 nm. Green: L_c = 300 nm. Blue: 1 µm.

6.2 Spatially-dependent exciton rate equation model

Once excitons are formed, they do not experience a force under an electric field (except under high field conditions, as mentioned above). Thus, the dominant transport mechanism for excitons is diffusion. For a spatially inhomogeneous device where the antenna feedgap may not occupy the entire area, it is important to account for the spatial exciton distribution. The full rate equations, including diffusion, bright and dark excitons, and exciton-exciton annihilation (EEA), are [102]:

$$\frac{dN_b}{dt} = \frac{N_d}{K\tau_{bd}} - \frac{N_b}{\tau_{bd}} - \frac{N_b}{\tau_r} - CN_b^2 + G_b + D\nabla^2 N_b \tag{63}$$

$$\frac{dN_d}{dt} = \frac{N_b}{\tau_{bd}} - \frac{N_d}{K\tau_{bd}} - CN_d^2 + KG_b + D\nabla^2 N_d \tag{64}$$

where N_b, N_d are the bright and dark exciton densities, τ_{bd} is the bright-to-dark scattering lifetime, $K = e^{(E_b - E_d)/kT}$ is the Boltzmann factor for the bright-dark energy splitting, τ_r is the radiative lifetime, G_b is the generation rate for bright excitons, D is the exciton diffusion coefficient, and C is the EEA coefficient. We assume there are no non-radiative recombination mechanisms aside from edge recombination. Note that τ_r and G_b depend on position. To solve these coupled non-linear differential equations, we first ignore EEA and linearize the equations in the frequency domain, $d/dt = i\omega$. This lets us find the spatial exciton distribution $N_{b,d}(x, y, \omega)$ versus frequency. We can then calculate the modulation efficiency, defined as the total radiative recombination divided by the total generation:

$$\eta(\omega) = \frac{\int dA\, A_r(x,y)|N_b(x,y,\omega)|}{\int dA\, G(x,y)} \tag{65}$$

where $G \equiv (1 + K)G_b$ is the total generation rate. The rate equations become:

$$\begin{pmatrix} -D\nabla^2 + \frac{1}{\tau_{bd}} + \frac{1}{\tau_r} + i\omega & -\frac{1}{K\tau_{bd}} \\ -\frac{1}{\tau_{bd}} & -D\nabla^2 + \frac{1}{K\tau_{bd}} + i\omega \end{pmatrix} \begin{pmatrix} N_b \\ N_d \end{pmatrix} = \begin{pmatrix} G_b \\ KG_b \end{pmatrix} \tag{66}$$

Edge recombination is implemented as the boundary condition:

$$D\left(\nabla N_{b,d} \cdot \hat{n}\right) = -v_e N_{b,d} \tag{67}$$

where v_e is the edge recombination velocity and $\hat{n}$ is the outward-pointing unit normal (parallel to the monolayer). We take v_e at the sides of the channel as 4 x 10^4 cm/s [104]. On the other hand, we found the field near the contacts can far exceed the required field for exciton dissociation. Therefore, we assume the worst case effective edge recombination velocity equal to the thermal velocity, $v_t \sim 10^7$ cm/s. The material parameters used are listed in Table 2.

Table 2. Material parameters for exciton diffusion simulation.

Parameter	**Description**	**Value**
D	Exciton diffusion coefficient	1 cm^2/s [130]
τ_{bd}	Bright-to-dark scattering time	100 fs [102]
v_{ee}	Edge recombination velocity at exposed edges	4 x 10^4 cm/s [104]
v_{ec}	Effective edge recombination velocity at contacts	10^7 cm/s

We discretize the equations on a spatial grid and solve them numerically using a sparse matrix solver. First, we simulate an example 200 x 200 nm device with and without antenna. The antenna enhancement is taken as a cos(y) variation along the slot (Fig. 81a). We also neglect dark excitons for now. The exciton density is plotted with and without antenna in Fig. 81b and 81c respectively. Clearly, the antenna acts as an exciton sink and lowers the exciton density substantially. The modulation efficiency is plotted in Fig. 81d with (black) and without (red) antenna. The antenna enhances both efficiency and speed. However, since the area fill factor is still low, the speed enhancement is modest, with a 3dB frequency of 16 GHz compared to 8 GHz without antenna. (3dB frequency is defined as the frequency where the modulation efficiency reaches half of its DC value.) Even without the antenna, the speed is boosted due to the enhanced non-radiative rate from edge recombination. However, this of course comes at a sharp cost in efficiency. The DC efficiency is 32% and 2.8% with and without antenna respectively.

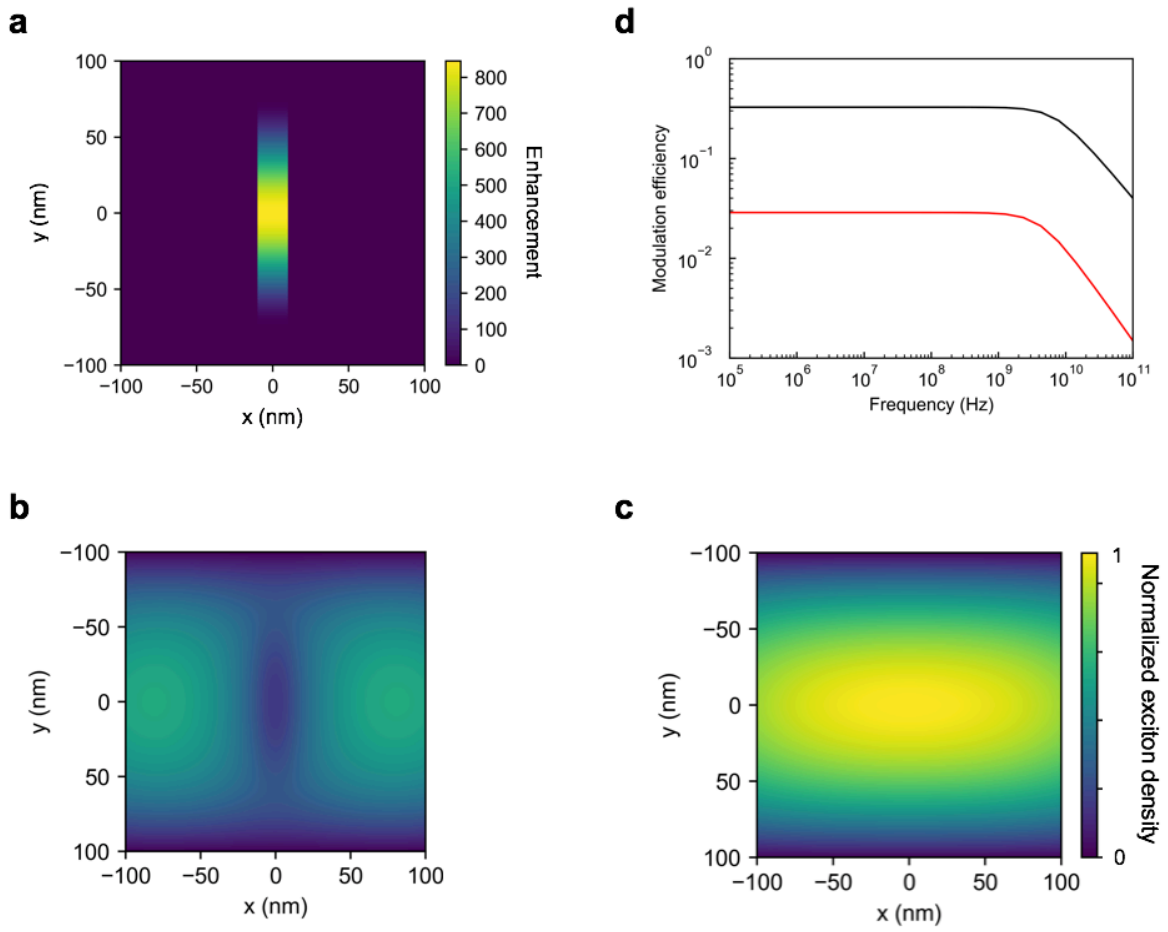

Figure 81. a) Rate enhancement map for 200 x 200 nm^2 antenna-coupled device. b) Simulated exciton density for antenna device. c) Simulated exciton density without antenna. d) Modulation efficiency for antenna device (black) and no antenna device (red).

We then sweep the channel length L_c from 20 nm to 200 nm, and channel width W_c from 20 nm to 200 nm. The 3dB frequency is plotted in Fig. 82a, and DC efficiency is plotted in Fig. 82b. We see that both f_{3dB} and efficiency improve with shrinking channel width, due to increasing fill factor in the antenna. Shrinking channel length improves efficiency up to a point, until it becomes smaller than the high enhancement portion of the antenna (~100 nm), then edge recombination decreases efficiency. The 100 x 20 nm^2 device achieves an f_{3dB} of 240 GHz and efficiency of 70%.

Next, we include the effect of dark excitons. Fig. 82c,d show f_{3dB} and efficiency versus L_c and W_c for a bright-dark energy splitting of $\Delta E = E_b - E_d = -30$ meV, similar to some literature values for $MoTe_2$ [102]. The lowest energy state is still bright, but there is a small decrease in efficiency and 3dB frequency. For the same device, the DC efficiency is 66% and f_{3dB} = 195 GHz. Fig. 82e,f show f_{3dB} and efficiency versus L_c and W_c for a bright-dark energy splitting of $\Delta E = E_b - E_d = 30$ meV, similar to literature values for WSe_2 [102]. In this case, the lowest

energy state is dark, which leads to a significant decrease in speed and efficiency, since the dark excitons are not affected by the antenna enhancement. The 100 x 20 nm^2 device now has efficiency of 44%, and the 3dB frequency is reduced to 86 GHz.

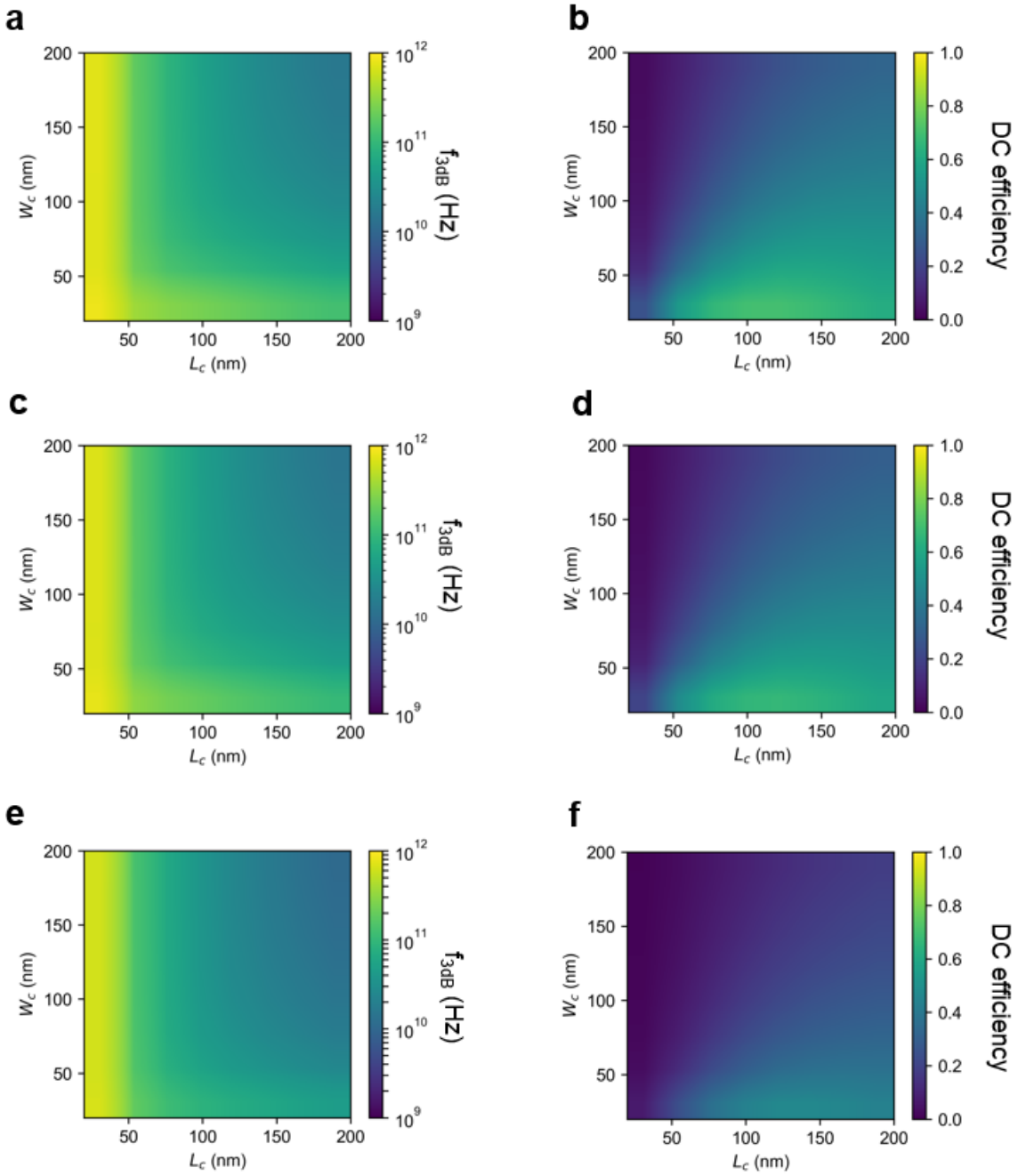

Figure 82. a,c,e) 3dB frequency versus channel length L_c and channel width W_c, without EEA. b,d,f) DC efficiency. a,b) No dark excitons ($\Delta E = E_b - E_d \to -\infty$). c,d) Lowest energy state is bright, $\Delta E = -30$ meV. e,f) Lowest energy state is dark, $\Delta E = 30$ meV.

Finally, we include the effect of exciton-exciton annihilation. Our approach is to summarize the parameters extracted above into the (non-spatially-dependent) rate equation:

$$\frac{dN}{dt} = \frac{I\eta_{inj}}{qa} - \frac{N}{\tau_r} - \frac{N}{\tau_{nr}} - CN^2 \tag{68}$$

where N is the exciton density, I is the current, η_{inj} is the injection efficiency, a is the device area, τ_r is the effective radiative lifetime, τ_{nr} is the effective non-radiative lifetime, and C is the EEA coefficient. τ_r and τ_{nr} are justified as follows. The spatially-dependent analysis above showed that the frequency response is nearly a single-pole function (Fig. 81d). Therefore, we may extract an averaged radiative lifetime τ_r and non-radiative lifetime (due to edge recombination) τ_{nr}, determined by:

$$\eta_{DC,0} = \frac{\tau_{nr}}{\tau_r + \tau_{nr}} \tag{69}$$

$$f_0 = \frac{1}{2\pi}\left(\frac{1}{\tau_r} + \frac{1}{\tau_{nr}}\right) \tag{70}$$

where $\eta_{DC,0}$ is the simulated DC efficiency without EEA and f_0 is the simulated corner frequency where modulation efficiency $\eta(f_0) = 1/\sqrt{2}$. These are defined so that the frequency response of the rate equation without EEA matches the response of the spatially-dependent model above. We solve the rate equation for (L_c, W_c) = (100 nm, 20 nm). The steady-state radiative efficiency, including edge recombination and EEA, can be shown to be:

$$\eta_{rad} = 2\left(\frac{\tau_{nr}}{\tau_r + \tau_{nr}}\right)\left(1 + \sqrt{1 + \frac{4I\eta_{inj}C}{qaA^2}}\right)^{-1} \tag{71}$$

where $A = 1/\tau_r + 1/\tau_{nr}$. The radiative efficiency is plotted in Fig. 83 versus injected current $I\eta_{inj}$, for no dark excitons (red), $\Delta E = -30\ meV$ (black), and $\Delta E = 30\ meV$ (blue). We assume C = 0.1 cm^2/s. EEA starts to decrease efficiency at ~200 nA for the worst case (lowest dark state) device, and around ~1 μA for the other two cases. The higher enhancement decreases the steady state exciton density, allowing for higher injection rates before EEA dominates.

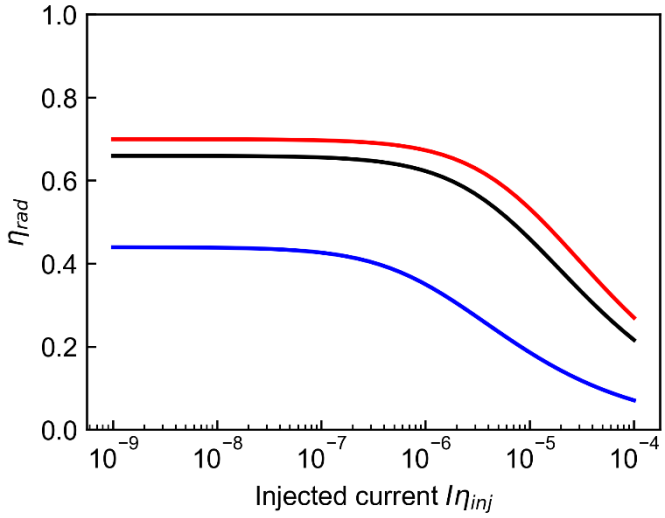

Figure 83. Radiative efficiency η_{rad} versus injected current $I\eta_{inj}$ for no dark excitons (red), $\Delta E = -30\ meV$ (black), and $\Delta E = 30\ meV$ (blue).

To summarize, given sufficient currents ~0.1-1 μA, exciton formation efficiencies >40% can be achieved, with exciton radiative efficiencies of ~40-70%. At low currents, the bimolecular exciton formation rate is not high enough to overcome carrier overshoot, while at high currents EEA dominates. The optimal device size in our simulations for high speed with decent efficiency is ~100 x 20 nm. The 3dB frequency can be as high as ~80-200 GHz. The channel width can be shrunk to the size of the antenna, since high enhancement can overcome the relatively low ERV at the sides. However, assuming worst-case effective ERV at the contacts, the channel length should be longer to avoid edge recombination there.

6.3 Efficiency versus channel length of large-area devices

Finally, we experimentally study the effect of varying channel length on EL and PL efficiency in order to confirm some aspects of our model. Devices (without antenna) were fabricated on the same Al_2O_3/ITO substrate as above. Four different flakes were tested, each with 6 devices of channel length 5, 3, 1, 0.5, 0.3, 0.1 μm. The channel width was ~10 μm. The flakes were etched using XeF_2 vapor after contact deposition to confine the current in the channel. First, we measure relative PL efficiency versus channel length. Fig. 84a shows a close up optical image of part of one flake with different channel length. Fig. 84b shows the corresponding PL map with color scale magnified to show the weakest emission (at L_c = 0.3 μm). No detectable emission was observed at L_c = 0.1 μm.

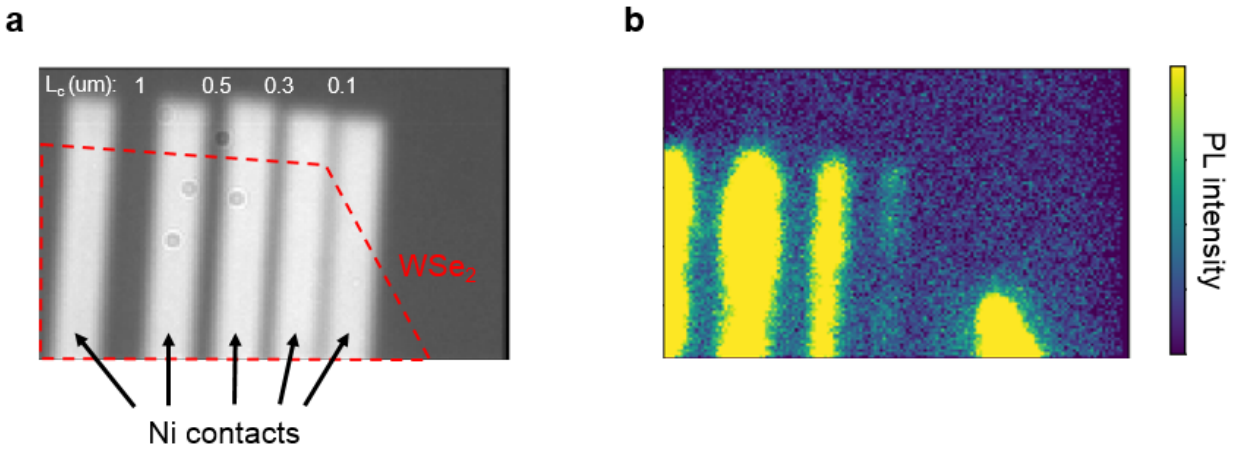

Figure 84. a) Optical image of devices with varying channel lengths. b) PL map with magnified color scale to show emission of 0.3 μm device.

Since the channel length can be below the diffraction limit, the measured PL is spread over a larger area than the channel length. Therefore, the relative PL efficiency is calculated as:

$$\eta_r = K \frac{integrated\ counts\ near\ channel}{(channel\ width\ integrated\ over)(channel\ length)} \tag{72}$$

where K is a normalization factor. Since the channel width is larger than the field of view, PL images were taken at different locations and the results are averaged for each flake. The results are plotted in Fig. 85a for the four different flakes. The relative PL QE stays roughly constant for 0.5 – 5 μm channel lengths, but drops sharply (~10x) for 0.3 μm channels. The EL QE was also measured for all devices. Since the efficiency depends on bias condition, a V_g sweep was performed with fixed V_p and V_n using the same procedure as in Chapter 4, and the peak QE was found for each sweep. In addition, the source-drain bias $V_p - V_n$ was varied between 6 - 14 V. For each device, the current was found to stop increasing after a certain bias. Also, small channel lengths exhibited much higher current at the same bias. Generally, the highest efficiency was found for the highest injected current. The EL internal quantum efficiency (IQE) is plotted in Fig. 85b for all flakes, as well as the current at peak EL IQE in Fig. 85c. Contrary to the PL QE, we see a sharp decrease at 0.5 μm, in addition to the decrease at 0.3 μm. No EL was observed for the 0.1 μm channel, with the exception of one flake.

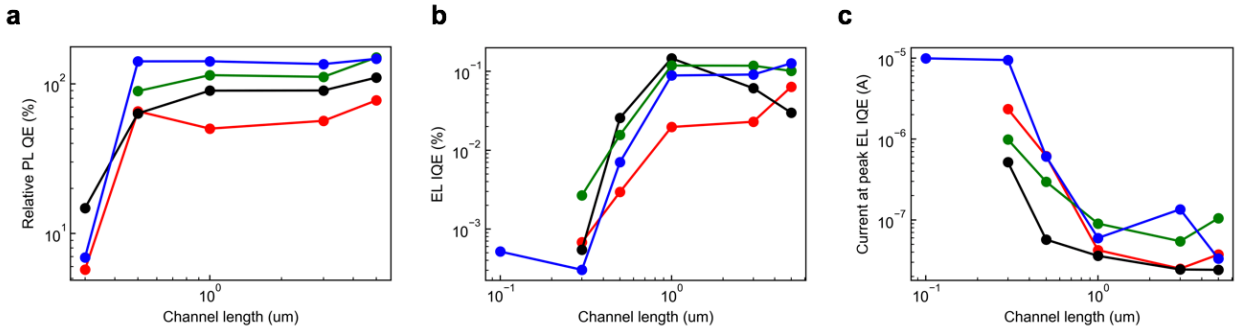

Figure 85. a) Relative PL QE versus channel length for the 4 flakes. b) EL IQE versus channel length. c) Current at peak EL IQE versus channel length.

Both the PL and EL QEs do not follow simple models for edge recombination, which predict $\eta \propto L_c$ or $\eta \propto L_c^2$ depending on the diffusion coefficient. However, the data shows a faster decrease in efficiency closer to $\eta \propto L_c^3$. The 1D diffusion equation for excitons is:

$$\frac{dN}{dt} = G - (A_r + A_{nr})N + D\frac{d^2N}{dx^2} \tag{73}$$

For a uniform generation rate $G = G_0$, this can be solved exactly with the edge recombination boundary condition above, yielding:

$$\eta = \frac{A_r}{A} - \frac{2v_e A_r}{L_c A^2}\left(\frac{\sinh\left(\sqrt{A/D}\,L_c/2\right)}{\sinh\left(\sqrt{A/D}\,L_c/2\right) + \frac{v_e}{\sqrt{AD}}\cosh\left(\sqrt{A/D}\,L_c/2\right)}\right) \tag{74}$$

where v_e is ERV and $A = A_r + A_{nr}$. For fast diffusion, $D \gg v_e^2/A$ and $D \gg AL_c^2/4$, this reduces to:

$$\eta = \frac{A_r}{A + 2v_e/L_c} \tag{75}$$

as expected. For small channel lengths $L_c \ll 2v_e/A$, this gives

$$\eta \cong \frac{A_r}{2v_e}L_c \tag{76}$$

On the other hand, if diffusion is slow, $D \ll v_e^2/A$, and at small channel length, $L_c \ll 2\sqrt{D/A}$ and $L_c \ll 2v_e/A$, we obtain to leading order:

$$\eta \cong \frac{A_r}{8D}L_c^2 \tag{77}$$

For non-uniform exciton generation such as a delta function distribution in the center, the efficiency is scaled but the channel length dependence remains the same.

A possible explanation is anomalous diffusion due to disorder in the system caused by the substrate supporting the monolayer. Under normal diffusion from a point source, the mean squared deviation (MSD) increases linearly with time as $\langle x^2 \rangle = 2Dt$. For an exciton generated at the center, this gives an expected time to reach the edge as $\tau = L_c^2/8D$, in agreement with the analysis above. However, recent work [131] on monolayer WSe_2 on SiO_2 has shown anomalous diffusion of excitons, $\langle x^2 \rangle = \Gamma t^{\alpha}$, where Γ and α are known as the transport factor and anomalous coefficient respectively [132]. This anomalous diffusion is well-known in other disordered systems [132]. For normal diffusion, $\alpha = 1$ and $\Gamma = 2D$. In the sub-diffusive regime, $\alpha < 1$. In [131], WSe_2 on SiO_2 showed $\alpha = 0.785$ and $\Gamma = 0.2$ $\mu m^2/ns^{\alpha}$. The effective diffusion coefficient is now time dependent [131]:

$$D(t) = \frac{1}{2}\frac{d\langle x^2 \rangle}{dt} = \frac{1}{2}\Gamma\alpha t^{\alpha-1} \tag{78}$$

We fit our measured PL and EL QE data to a simple model based on this anomalous diffusion. Assume excitons are generated in the center of the channel. The expected time to reach the edge is now $\tau = (L_c^2/4\Gamma)^{1/\alpha}$. Once an exciton reaches the edge, it encounters an effective linear density of traps N_{st} (1/cm) with capture cross-section σ_s (cm). The probability of capture is $P_r \sim N_{st}\sigma_s$. This agrees with the conventional definition of surface recombination velocity [133]:

$$v_s = N_{st} v_{th} \sigma_s \tag{79}$$

If the entire edge (or surface) is taken up by traps, $P_r = 1$ and v_s becomes the thermal velocity. The lifetime is scaled by this probability, giving $\tau = (L_c^2/4\Gamma)^{1/\alpha}/P_r$. The efficiency is then given by:

$$\eta = \frac{A_r}{A + 1/\tau} = \frac{A_r}{A + P_r(4\Gamma/L_c^2)^{1/\alpha}} \tag{80}$$

We assume $P_r = 1$ for EL due to the high field, so that every exciton that reaches the edge will be lost. We then fit P_r to the PL data. Also, we take the lifetime as 1 ns, so $A = 10^9$ s^{-1}. We obtain a good fit for PL and EL with $\Gamma = 7 \times 10^{-10}\ m^2/s^{\alpha}$, $\alpha = 0.4$ and $P_r = 0.08$. This anomalous coefficient is somewhat lower than that reported in [131], likely due to the higher roughness of the Al_2O_3 oxide used here compared with SiO_2. The effective diffusion coefficient is plotted in Fig. 86a. It ranges from ~0.4 to 3 cm^2/s, within the ~1-10 cm^2/s range commonly reported in literature [130]. The fits to the PL and EL data are shown in Fig. 86b and 86c respectively (grey

lines). (The fit for EL IQE has an overall scaling factor from non-radiative carrier recombination $B_{nr}n^2$ versus exciton formation $B_{ex}n^2$ [81, 104]). We also fit it to the normal diffusion model for uniform generation given above, with D = 1 cm^2/s and v_e = 10^7 cm/s for EL and $v_e = P_r v_{th} = 8 \times 10^5$ cm/s for PL, shown in Fig. 86b and 86c (orange lines). The anomalous diffusion model provides slightly higher efficiencies than normal diffusion at intermediate channel lengths, while decreasing efficiency at lower channel lengths (although the single bright 0.1 μm device is close to the orange curve). Thus, to obtain more favorable length scaling $\eta \propto L_c$ or $\eta \propto L_c^2$, control of disorder in the system is required, possibly by using an atomically smooth oxide such as hBN. The rate equation model for exciton diffusion above could then be applied, which showed that antenna enhancement can overcome edge recombination even for ERVs at the thermal velocity.

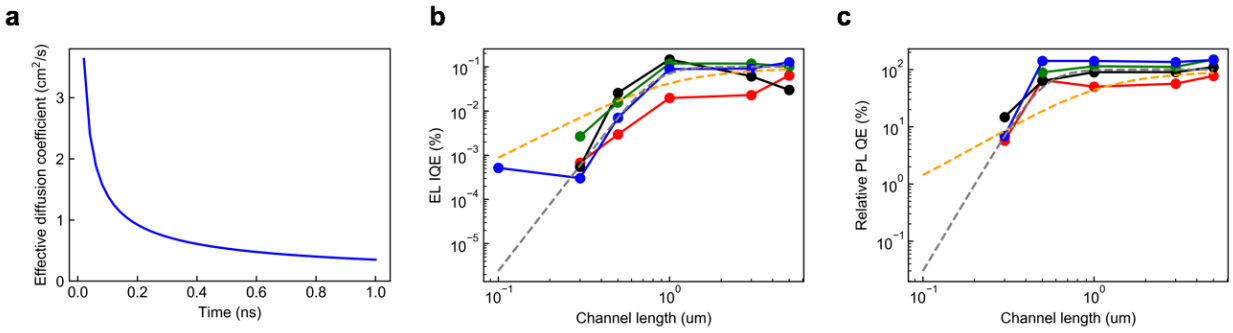

Figure 86. a) Calculated effective exciton diffusion coefficient versus time. b) Relative PL QE versus channel length, with fit to anomalous diffusion model (grey line) and normal diffusion model (orange line). c) EL IQE versus channel length, with same fits.

6.3.1 Photocurrent measurements

The decrease in the EL QE compared to the PL QE could be due to carrier overshoot or increased exciton dissociation at high field regions. To investigate exciton dissociation, photocurrent measurements were performed on the same devices. Positive and negative pulsed bias was applied to individual contacts to isolate the effects of each. Either V_p = 4V, V_n = 0V, or V_p = 0V, V_n = -4V was applied, and the current was measured during the pulse with and without laser excitation. 4V was chosen to be close to the voltages used in EL. The difference in current with and without the laser was taken as the induced photocurrent. Fig. 87 shows an example pulse for the 0.1 μm device.

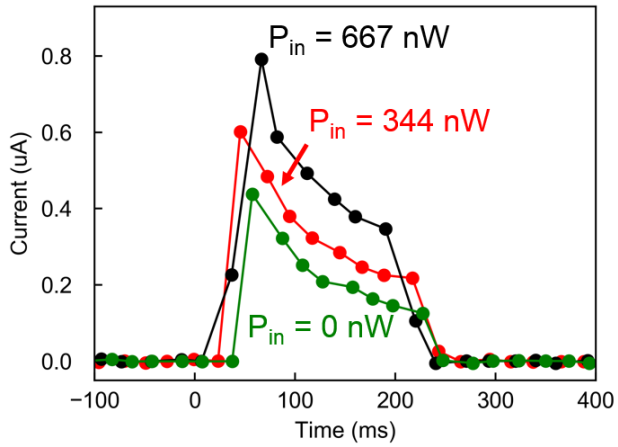

Figure 87. Photocurrent versus time for a 0.1 μm device, with a 0.2 s voltage pulse applied: V_p = 0V, V_n = -4V.

We estimate the IQE of photodetection using:

$$\eta_i = \frac{\hbar\omega}{q}\frac{I}{P\eta_{abs}\eta_{overlap}} \tag{81}$$

where P is the laser power, I is the current, η_{abs} is the absorption (estimated as ~6% from simulation), and $\eta_{overlap}$ is the overlap of the laser spot with the channel. A 20x objective was used due to space constraints with the electrical probes, so the laser spot is much larger than the small channels. Although excitons are excited outside the channel region, the current collected was nearly equal and opposite on source and drain contacts, confirming current flow across the channel region only. The overlap was estimated using an image of the laser spot together with an optical image of the devices, by integrating the laser power over the channel region and dividing by the total power of the laser spot. The current vs power curves are shown in Fig. 88 for 0.1 and 0.3 μm devices. Generally, applying a negative bias resulted in much higher IQE, which may be due to the metal work function being closer to the valence band, resulting in higher field when applying a negative bias. A peak IQE of 65% was estimated for the 0.1 μm device with V_n = -4V. The high field region is clearly large enough to cause substantial photocurrent generation, and thus exciton dissociation for EL.

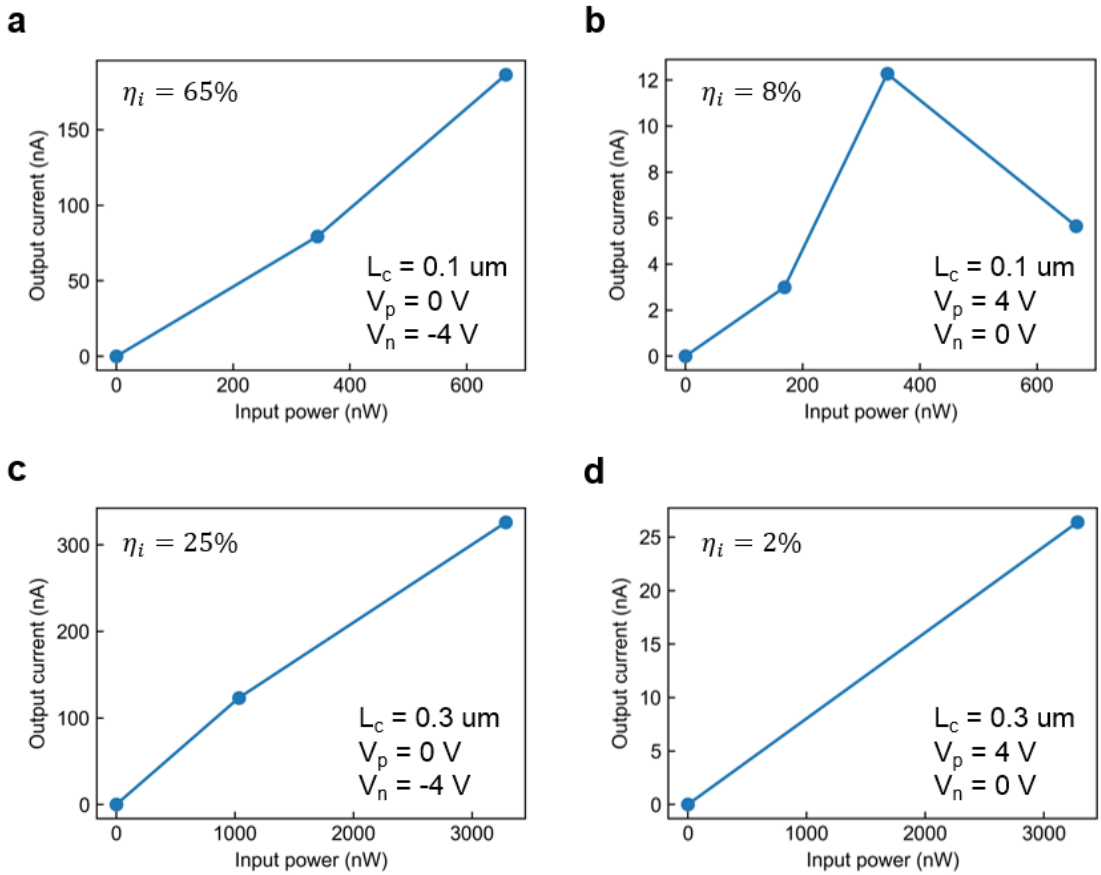

Figure 88. Photocurrent versus optical power absorbed for 0.1 μm (a,b) and 0.3 μm (c,d) devices, with V_n = -4V (a,c) or V_p = 4V (b,d).

We plot the peak IQE versus channel length for both V_p = 4V and V_n = -4V in Fig. 89. The IQE as a function of channel length can be simply estimated as:

$$\eta_i = \frac{L_{hf}}{L_c} \tag{82}$$

where L_{hf} is the length of the high field region, assuming all carriers generated in this region are collected. This gives a reasonable fit to the data, with L_{hf} = 60 nm for V_n = -4V and L_{hf} = 6 nm for V_p = 4V.

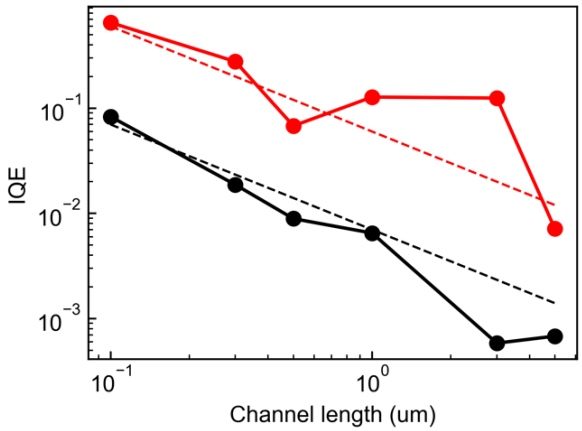

Figure 89. IQE versus channel length for V_p = 4V pulses (black) and V_n = -4V pulses (red). Solid lines: data. Dashed lines: fit.

In our exciton rate equation model, exciton dissociation is included by taking the ERV to be the thermal velocity near the contacts. Thus, if this is indeed the major cause of low efficiency in our experimental results, sufficient antenna enhancement should be able to overcome this. However, the high field region was estimated as ~60 nm, which can be a substantial fraction of the channel, while the ERV model is only an edge effect. Thus, contact optimization is necessary to lower the field strength near the contacts.

To summarize, we have studied the efficiency and modulation speed of single-antenna devices. We showed that given the assumptions of our model, decent exciton formation efficiencies >40% and exciton radiative efficiencies 40-70% can be achieved at currents of ~0.1 – 1 μA. At low current, carrier overshoot limits efficiency, while at high currents EEA dominates. Modulation speed can reach ~80-200 GHz with 100 x 20 nm^2 devices. We measured the PL and EL efficiencies of devices with varying channel lengths, and showed a sharp decrease in efficiency below 0.3 μm for PL and 0.5 μm for EL. We performed photocurrent measurements to study the effect of high fields, and showed efficient photocarrier collection for small channel lengths, pointing to exciton dissociation as a cause of low EL efficiency.

7 Conclusion

In this dissertation, we have shown that antenna-enhanced nanoLEDs are a promising route to achieve high-speed, high-efficiency on-chip light emitters, with potential to drastically reduce power consumption in modern electronics. NanoLEDs with high spontaneous emission enhancement feature speeds competitive with lasers together with high quantum efficiencies ~50% theoretically limited only by metal loss. We have shown that helium-ion milling is a promising technique to fabricate the required nanoscale gaps (~10-20 nm) with high precision, demonstrating slot antennas with extremely high scattering polarization ratios ~37x. We have introduced monolayer transition metal dichalcogenides as an active material for nanoLEDs, which have pristine surfaces with no dangling bonds. They feature novel excitonic physics due to the strong Coulomb interaction in 2D, opening up new challenges and opportunities for nanoLED design. We introduce pulsed injection as a method to stabilize light emission of TMDC LEDs in ambient conditions, greatly extending device lifetime. We study the causes of current decay in ambient and vacuum conditions. We also demonstrate antenna-coupled light emitting devices: a light-emitting capacitor with high polarization ratios >30x, and a light-emitting diode with >10x enhanced EL intensity. Finally, we theoretically study highly-scaled TMDC light emitters coupled to single antennas, and show that high speed (>80 GHz) is possible with moderate efficiencies (>10%). While there has been rapid advances in theoretical and practical understanding of TMDC light emitters in recent years, much work remains to be done to realize this optimistic picture. These include:

1) **Improved EL QE.** The highest reported QEs for TMDC LEDs in literature are ~1-10%, limited by the internal quantum yield of the material. Improved material growth must be undertaken, or chemical treatments such as superacid integrated into a practical nanoLED process.
2) **Improved contact resistance.** While work on the nanoelectronics front has shown numerous doping methods for TMDCs, it is challenging to incorporate both types of doping in a single device. Contact resistance will degrade the energy efficiency of the device even if quantum efficiency is high. One possibility on this front is lateral or vertical heterojunctions, where materials amenable to hole or electron injection are integrated together.
3) **Further demonstration of antenna-enhanced devices.** Few demonstrations of cavity or antenna-coupled electrically-injected TMDC LEDs exist. Antenna coupling is challenging due to the small device size or high area fill factor required. Therefore, further work on mode engineering (for antenna arrays) or device scaling (for single antennas) is required, as well as process improvements for better transfer yield and nanoscale patterning.

Finally, the sensitivity of TMDCs to their environment may be a blessing as well as a curse. Unlike bulk semiconductors, material properties such as mobility, exciton-exciton annihilation coefficient, band gap, exciton binding energy, and dielectric constant can be tuned by tailoring the surrounding environment. Creative use of such knobs may solve some of the present and future issues raised here. The field of 2D material optoelectronics is sure to have many exciting advances in science and engineering for years to come.

8 References

1. Magen, Nir, Avinoam Kolodny, Uri Weiser, and Nachum Shamir. 2004. Interconnect-power Dissipation in a Microprocessor. In *Proceedings of the 2004 International Workshop on System Level Interconnect Prediction*, 7–13. SLIP '04. New York, NY, USA: ACM. doi:10.1145/966747.966750.
2. Miller, D. A. B. 2009. Device Requirements for Optical Interconnects to Silicon Chips. *Proceedings of the IEEE* 97: 1166–1185. doi:10.1109/JPROC.2009.2014298.
3. Miller, D. A. B. 2000. Rationale and challenges for optical interconnects to electronic chips. *Proceedings of the IEEE* 88: 728–749. doi:10.1109/5.867687.
4. MIT Microphotonics Center. 2013. On-Board Optical Interconnection Digest. April.
5. Bakoglu, H.B. 1990. *Circuits, Interconnections, and Packaging for VLSI*. Addison-Wesley Publishing Company, Inc.
6. Teichmann, Philip. 2012. Fundamentals of Adiabatic Logic. In *Adiabatic Logic: Future Trend and System Level Perspective*, ed. Philip Teichmann, 5–22. Springer Series in Advanced Microelectronics. Dordrecht: Springer Netherlands. doi:10.1007/978-94-007-2345-0_2.
7. Fox, Mark. 2006. *Quantum Optics: An Introduction*. Oxford University Press.
8. Takeda, Koji, Tomonari Sato, Akihiko Shinya, Kengo Nozaki, Wataru Kobayashi, Hideaki Taniyama, Masaya Notomi, Koichi Hasebe, Takaaki Kakitsuka, and Shinji Matsuo. 2013. Few-fJ/bit data transmissions using directly modulated lambda-scale embedded active region photonic-crystal lasers. *Nature Photonics* 7: 569–575. doi:10.1038/nphoton.2013.110.
9. Khurgin, Jacob B., and Alexandra Boltasseva. 2012. Reflecting upon the losses in plasmonics and metamaterials. *MRS Bulletin* 37: 768–779. doi:10.1557/mrs.2012.173.
10. Khurgin, Jacob B., and Greg Sun. 2012. How small can "Nano" be in a "Nanolaser"? : Nanophotonics. July 1.
11. Oulton, Rupert F., Volker J. Sorger, Thomas Zentgraf, Ren-Min Ma, Christopher Gladden, Lun Dai, Guy Bartal, and Xiang Zhang. 2009. Plasmon lasers at deep subwavelength scale. *Nature* 461: 629–632. doi:10.1038/nature08364.
12. Liu, Ning, Agnieszka Gocalinska, John Justice, Farzan Gity, Ian Povey, Brendan McCarthy, Martyn Pemble, et al. 2016. Lithographically Defined, Room Temperature Low Threshold Subwavelength Red-Emitting Hybrid Plasmonic Lasers. *Nano Letters* 16: 7822–7828. doi:10.1021/acs.nanolett.6b04017.
13. Wei, Wei, Xin Yan, and Xia Zhang. 2016. Ultrahigh Purcell factor in low-threshold nanolaser based on asymmetric hybrid plasmonic cavity. *Scientific Reports* 6: srep33063. doi:10.1038/srep33063.
14. Hill, Martin T., Milan Marell, Eunice S. P. Leong, Barry Smalbrugge, Youcai Zhu, Minghua Sun, Peter J. van Veldhoven, et al. 2009. Lasing in metal-insulator-metal sub-wavelength plasmonic waveguides. *Optics Express* 17: 11107–11112. doi:10.1364/OE.17.011107.
15. Hill, Martin T., Yok-Siang Oei, Barry Smalbrugge, Youcai Zhu, Tjibbe de Vries, Peter J. van Veldhoven, Frank W. M. van Otten, et al. 2007. Lasing in metallic-coated nanocavities. *Nature Photonics* 1: 589–594. doi:10.1038/nphoton.2007.171.

16. Lau, Erwin K., Amit Lakhani, Rodney S. Tucker, and Ming C. Wu. 2009. Enhanced modulation bandwidth of nanocavity light emitting devices. *Optics Express* 17: 7790–7799. doi:10.1364/OE.17.007790.
17. Chuang, Shun Lien. 2009. *Physics of Photonic Devices*. 2nd ed.
18. E.M. Purcell. 1946. Spontaneous Emission Probabilities at Radio Frequencies. *Physical Review* 69: 681. doi:10.1103/PhysRev.69.674.2.
19. Taflove, A., A. Oskooi, and S.G. Johnson. 2013. *Advances in FDTD Computational Electrodynamics: Photonics and Nanotechnology*. Artech House.
20. Balanis, Constantine A. 2005. *Antenna Theory - Analysis and Design*. 3rd ed.
21. Shockley, W. 1938. Currents to Conductors Induced by a Moving Point Charge. *Journal of Applied Physics* 9: 635–636. doi:10.1063/1.1710367.
22. Gilberd, P. W. 1982. The anomalous skin effect and the optical properties of metals. *Journal of Physics F: Metal Physics* 12: 1845. doi:10.1088/0305-4608/12/8/024.
23. Eggleston, M., K. Messer, E. Yablonovitch, and M. C. Wu. 2014. Circuit theory of optical antenna shedding light on fundamental limit of rate enhancement. In *2014 Conference on Lasers and Electro-Optics (CLEO) - Laser Science to Photonic Applications*, 1–2. doi:10.1364/CLEO_QELS.2014.FM2K.4.
24. Suhr, T., N. Gregersen, K. Yvind, and J. Mørk. 2010. Modulation response of nanoLEDs and nanolasers exploiting Purcell enhanced spontaneous emission. *Optics Express* 18: 11230–11241. doi:10.1364/OE.18.011230.
25. Krishna, K. H., K. V. Sreekanth, and G. Strangi. 2016. Dye-embedded and nanopatterned hyperbolic metamaterials for spontaneous emission rate enhancement. *JOSA B* 33: 1038–1043. doi:10.1364/JOSAB.33.001038.
26. Reecht, Gaël, Fabrice Scheurer, Virginie Speisser, Yannick J. Dappe, Fabrice Mathevet, and Guillaume Schull. 2014. Electroluminescence of a Polythiophene Molecular Wire Suspended between a Metallic Surface and the Tip of a Scanning Tunneling Microscope. *Physical Review Letters* 112: 047403. doi:10.1103/PhysRevLett.112.047403.
27. Kinkhabwala, Anika, Zongfu Yu, Shanhui Fan, Yuri Avlasevich, Klaus Müllen, and W. E. Moerner. 2009. Large single-molecule fluorescence enhancements produced by a bowtie nanoantenna. *Nature Photonics* 3: nphoton.2009.187. doi:10.1038/nphoton.2009.187.
28. Gerard, J.-, and B. Gayral. 1999. Strong Purcell effect for InAs quantum boxes in three-dimensional solid-state microcavities. *Journal of Lightwave Technology* 17: 2089–2095. doi:10.1109/50.802999.
29. Fortuna, S. A., M. S. Eggleston, K. Messer, E. Yablonovitch, and M. C. Wu. 2015. Large spontaneous emission rate enhancement from an electrically-injected nanoLED coupled to an optical antenna. In *2015 IEEE Photonics Conference (IPC)*, 172–173. doi:10.1109/IPCon.2015.7323683.
30. Fortuna, S. A., C. Heidelberger, K. Messer, K. Han, E. A. Fitzgerald, E. Yablonovitch, and M. C. Wu. 2016. Optical antenna enhanced spontaneous emission rate in electrically injected nanoscale III #x2013;V LED. In *2016 International Semiconductor Laser Conference (ISLC)*, 1–2.
31. Luk, T., S. Xiong, B. G. Farfan, W. W. Chow, I. El-Kady, X. Miao, P. J. Resnick, et al. 2010. Strong Purcell enhancement of emission from close-packed colloidal quantum-dots in a photonic-lattice cavity. In *2010 IEEE Photonics Society Winter Topicals Meeting Series (WTM)*, 124–125. doi:10.1109/PHOTWTM.2010.5421949.
32. Biteen, Julie S., Domenico Pacifici, Nathan S. Lewis, and Harry A. Atwater. 2005. Enhanced Radiative Emission Rate and Quantum Efficiency in Coupled Silicon

Nanocrystal-Nanostructured Gold Emitters. *Nano Letters* 5: 1768–1773. doi:10.1021/nl051207z.
33. Liu, Chang-Hua, Genevieve Clark, Taylor Fryett, Sanfeng Wu, Jiajiu Zheng, Fariba Hatami, Xiaodong Xu, and Arka Majumdar. 2017. Nanocavity Integrated van der Waals Heterostructure Light-Emitting Tunneling Diode. *Nano Letters* 17: 200–205. doi:10.1021/acs.nanolett.6b03801.
34. Luo, Yue, Gabriella D. Shepard, Jenny V. Ardelean, Daniel A. Rhodes, Bumho Kim, Katayun Barmak, James C. Hone, and Stefan Strauf. 2018. Deterministic coupling of site-controlled quantum emitters in monolayer WSe 2 to plasmonic nanocavities. *Nature Nanotechnology*: 1. doi:10.1038/s41565-018-0275-z.
35. Butun, Serkan, Sefaattin Tongay, and Koray Aydin. 2015. Enhanced Light Emission from Large-Area Monolayer MoS2 Using Plasmonic Nanodisc Arrays. *Nano Letters* 15: 2700–2704. doi:10.1021/acs.nanolett.5b00407.
36. Wang, Zhuo, Zhaogang Dong, Yinghong Gu, Yung-Huang Chang, Lei Zhang, Lain-Jong Li, Weijie Zhao, et al. 2016. Giant photoluminescence enhancement in tungsten-diselenide–gold plasmonic hybrid structures. *Nature Communications* 7: 11283. doi:10.1038/ncomms11283.
37. Mashford, Benjamin S., Matthew Stevenson, Zoran Popovic, Charles Hamilton, Zhaoqun Zhou, Craig Breen, Jonathan Steckel, et al. 2013. High-efficiency quantum-dot light-emitting devices with enhanced charge injection. *Nature Photonics* 7: 407–412. doi:10.1038/nphoton.2013.70.
38. Gómez-Campos, Francisco M., Salvador Rodríguez-Bolívar, and Marco Califano. 2016. High-Mobility Toolkit for Quantum Dot Films. Research-article. doi:10.1021/acsphotonics.6b00377. October 26.
39. Bothra, S., S. D. Tyagi, S. K. Ghandhi, and J. M. Borrego. 1990. Surface recombination velocity and lifetime in InP measured by transient microwave reflectance. In *IEEE Conference on Photovoltaic Specialists*, 404–408 vol.1. doi:10.1109/PVSC.1990.111656.
40. Nolte, D. D. 1990. Surface recombination, free-carrier saturation, and dangling bonds in InP and GaAs. *Solid-State Electronics* 33: 295–298. doi:10.1016/0038-1101(90)90169-F.
41. Baek, D., S. Rouvimov, B. Kim, T.-C. Jo, and D. K. Schroder. 2005. Surface recombination velocity of silicon wafers by photoluminescence. *Applied Physics Letters* 86: 112110. doi:10.1063/1.1884258.
42. Yablonovitch, E., D. L. Allara, C. C. Chang, T. Gmitter, and T. B. Bright. 1986. Unusually Low Surface-Recombination Velocity on Silicon and Germanium Surfaces. *Physical Review Letters* 57: 249–252. doi:10.1103/PhysRevLett.57.249.
43. Yablonovitch, E., C. J. Sandroff, R. Bhat, and T. Gmitter. 1987. Nearly ideal electronic properties of sulfide coated GaAs surfaces. *Applied Physics Letters* 51: 439–441. doi:10.1063/1.98415.
44. Fortuna, S. A., A. Taghizadeh, E. Yablonovitch, and M. C. Wu. 2016. Toward 100 GHz direct modulation rate of antenna coupled nanoLED. In *2016 IEEE Photonics Conference (IPC)*, 216–217. doi:10.1109/IPCon.2016.7831047.
45. Hill, Raymond, John Notte, and Bill Ward. 2008. The ALIS He ion source and its application to high resolution microscopy. *Physics Procedia* 1. Proceedings of the Seventh International Conference on Charged Particle Optics (CPO-7): 135–141. doi:10.1016/j.phpro.2008.07.088.
46. Wang, Yudong, Martina Abb, Stuart A. Boden, Javier Aizpurua, C. H. de Groot, and Otto L. Muskens. 2013. Ultrafast Nonlinear Control of Progressively Loaded, Single Plasmonic

Nanoantennas Fabricated Using Helium Ion Milling. *Nano Letters* 13: 5647–5653. doi:10.1021/nl403316z.
47. Scholder, Olivier, Konstantins Jefimovs, Ivan Shorubalko, Christian Hafner, Urs Sennhauser, and Gian-Luca Bona. 2013. Helium focused ion beam fabricated plasmonic antennas with sub-5 nm gaps. *Nanotechnology* 24: 395301. doi:10.1088/0957-4484/24/39/395301.
48. Xia, Deying, John Notte, Lewis Stern, and Bernhard Goetze. 2015. Enhancement of XeF2-assisted gallium ion beam etching of silicon layer and endpoint detection from backside in circuit editing. *Journal of Vacuum Science & Technology B* 33: 06F501. doi:10.1116/1.4928744.
49. Ramachandra, Ranjan. 2009. A Study of Helium Ion Induced Secondary Electron Production. *Doctoral Dissertations*.
50. Wang, Haotian, Zhiyi Lu, Shicheng Xu, Desheng Kong, Judy J. Cha, Guangyuan Zheng, Po-Chun Hsu, et al. 2013. Electrochemical tuning of vertically aligned MoS2 nanofilms and its application in improving hydrogen evolution reaction. *Proceedings of the National Academy of Sciences* 110: 19701–19706. doi:10.1073/pnas.1316792110.
51. Mak, Kin Fai, Changgu Lee, James Hone, Jie Shan, and Tony F. Heinz. 2010. Atomically Thin MoS2: A New Direct-Gap Semiconductor. *Phys. Rev. Lett.* 105: 136805. doi:10.1103/PhysRevLett.105.136805.
52. Xiao, Jun, Mervin Zhao, Yuan Wang, and Xiang Zhang. 2017. Excitons in atomically thin 2D semiconductors and their applications. *Nanophotonics* 6: 1309–1328. doi:10.1515/nanoph-2016-0160.
53. He, Keliang, Nardeep Kumar, Liang Zhao, Zefang Wang, Kin Fai Mak, Hui Zhao, and Jie Shan. 2014. Tightly Bound Excitons in Monolayer ${\mathrm{WSe}}_{2}$. *Physical Review Letters* 113: 026803. doi:10.1103/PhysRevLett.113.026803.
54. Yu, Zhihao, Zhun-Yong Ong, Songlin Li, Jian-Bin Xu, Gang Zhang, Yong-Wei Zhang, Yi Shi, and Xinran Wang. 2017. Analyzing the Carrier Mobility in Transition-Metal Dichalcogenide MoS2 Field-Effect Transistors. *Advanced Functional Materials* 27: 1604093. doi:10.1002/adfm.201604093.
55. Allain, Adrien, Jiahao Kang, Kaustav Banerjee, and Andras Kis. 2015. Electrical contacts to two-dimensional semiconductors. *Nature Materials* 14: 1195–1205. doi:10.1038/nmat4452.
56. Kim, Changsik, Inyong Moon, Daeyeong Lee, Min Sup Choi, Faisal Ahmed, Seunggeol Nam, Yeonchoo Cho, Hyeon-Jin Shin, Seongjun Park, and Won Jong Yoo. 2017. Fermi Level Pinning at Electrical Metal Contacts of Monolayer Molybdenum Dichalcogenides. *ACS Nano* 11: 1588–1596. doi:10.1021/acsnano.6b07159.
57. Tosun, Mahmut, Leslie Chan, Matin Amani, Tania Roy, Geun Ho Ahn, Peyman Taheri, Carlo Carraro, Joel W. Ager, Roya Maboudian, and Ali Javey. 2016. Air-Stable n-Doping of WSe2 by Anion Vacancy Formation with Mild Plasma Treatment. *ACS Nano* 10: 6853–6860. doi:10.1021/acsnano.6b02521.
58. Kiriya, Daisuke, Mahmut Tosun, Peida Zhao, Jeong Seuk Kang, and Ali Javey. 2014. Air-Stable Surface Charge Transfer Doping of MoS2 by Benzyl Viologen. *Journal of the American Chemical Society* 136: 7853–7856. doi:10.1021/ja5033327.
59. Das, Saptarshi, Hong-Yan Chen, Ashish Verma Penumatcha, and Joerg Appenzeller. 2013. High Performance Multilayer MoS2 Transistors with Scandium Contacts. *Nano Letters* 13: 100–105. doi:10.1021/nl303583v.

60. Fang, Hui, Steven Chuang, Ting Chia Chang, Kuniharu Takei, Toshitake Takahashi, and Ali Javey. 2012. High-Performance Single Layered WSe2 p-FETs with Chemically Doped Contacts. *Nano Letters* 12: 3788–3792. doi:10.1021/nl301702r.
61. Late, Dattatray J., Bin Liu, H. S. S. Ramakrishna Matte, Vinayak P. Dravid, and C. N. R. Rao. 2012. Hysteresis in Single-Layer MoS2 Field Effect Transistors. *ACS Nano* 6: 5635–5641. doi:10.1021/nn301572c.
62. Shimazu, Yoshihiro, Mitsuki Tashiro, Satoshi Sonobe, and Masaki Takahashi. 2016. Environmental Effects on Hysteresis of Transfer Characteristics in Molybdenum Disulfide Field-Effect Transistors. *Scientific Reports* 6: srep30084. doi:10.1038/srep30084.
63. Bartolomeo, Antonio Di, Luca Genovese, Filippo Giubileo, Laura Iemmo, Giuseppe Luongo, Tobias Foller, and Marika Schleberger. 2018. Hysteresis in the transfer characteristics of MoS 2 transistors. *2D Materials* 5: 015014. doi:10.1088/2053-1583/aa91a7.
64. Shu, Jiapei, Gongtao Wu, Yao Guo, Bo Liu, Xianlong Wei, and Qing Chen. 2016. The intrinsic origin of hysteresis in MoS2 field effect transistors. *Nanoscale* 8: 3049–3056. doi:10.1039/C5NR07336G.
65. Carrion, E. A., A. Y. Serov, S. Islam, A. Behnam, A. Malik, F. Xiong, M. Bianchi, R. Sordan, and E. Pop. 2014. Hysteresis-Free Nanosecond Pulsed Electrical Characterization of Top-Gated Graphene Transistors. *IEEE Transactions on Electron Devices* 61: 1583–1589. doi:10.1109/TED.2014.2309651.
66. Wang, Junjie, Daniel Rhodes, Simin Feng, Minh An T. Nguyen, K. Watanabe, T. Taniguchi, Thomas E. Mallouk, Mauricio Terrones, Luis Balicas, and J. Zhu. 2015. Gate-modulated conductance of few-layer WSe2 field-effect transistors in the subgap regime: Schottky barrier transistor and subgap impurity states. *Applied Physics Letters* 106: 152104. doi:10.1063/1.4918282.
67. Park, Junghak, Hyunsuk Woo, and Sanghun Jeon. 2017. Impact of fast transient charging and ambient on mobility of WS2 field-effect transistor. *Journal of Vacuum Science & Technology B, Nanotechnology and Microelectronics: Materials, Processing, Measurement, and Phenomena* 35: 050601. doi:10.1116/1.4989781.
68. Pospischil, Andreas, Marco M. Furchi, and Thomas Mueller. 2014. Solar-energy conversion and light emission in an atomic monolayer p-n diode. *Nat Nano* 9: 257–261.
69. Baugher, Britton W. H., Hugh O. H. Churchill, Yafang Yang, and Pablo Jarillo-Herrero. 2014. Optoelectronic devices based on electrically tunable p-n diodes in a monolayer dichalcogenide. *Nature Nanotechnology* 9: 262–267. doi:10.1038/nnano.2014.25.
70. Ross, Jason S., Philip Klement, Aaron M. Jones, Nirmal J. Ghimire, Jiaqiang Yan, MandrusD. G., Takashi Taniguchi, et al. 2014. Electrically tunable excitonic light-emitting diodes based on monolayer WSe2 p-n junctions. *Nat Nano* 9: 268–272.
71. Withers, F., O. Del Pozo-Zamudio, A. Mishchenko, A. P. Rooney, A. Gholinia, K. Watanabe, T. Taniguchi, et al. 2015. Light-emitting diodes by band-structure engineering in van der Waals heterostructures. *Nature Materials* 14: 301–306. doi:10.1038/nmat4205.
72. Bie, Ya-Qing, Gabriele Grosso, Mikkel Heuck, Marco M. Furchi, Yuan Cao, Jiabao Zheng, Darius Bunandar, et al. 2017. A $MoTe_2$-based light-emitting diode and photodetector for silicon photonic integrated circuits. *Nature Nanotechnology* 12: 1124–1129. doi:10.1038/nnano.2017.209.
73. Wang, Junyong, Ivan Verzhbitskiy, and Goki Eda. Electroluminescent Devices Based on 2D Semiconducting Transition Metal Dichalcogenides. *Advanced Materials* 0: 1802687. doi:10.1002/adma.201802687.

74. Dhyani, Veerendra, and Samaresh Das. 2017. High-Speed Scalable Silicon-MoS_2 P-N Heterojunction Photodetectors. *Scientific Reports* 7: 44243. doi:10.1038/srep44243.
75. Sundaram, R. S., M. Engel, A. Lombardo, R. Krupke, A. C. Ferrari, Ph. Avouris, and M. Steiner. 2013. Electroluminescence in Single Layer MoS2. *Nano Letters* 13: 1416–1421. doi:10.1021/nl400516a.
76. Ye, Yu, Ziliang Ye, Majid Gharghi, Hanyu Zhu, Mervin Zhao, Yuan Wang, Xiaobo Yin, and Xiang Zhang. 2014. Exciton-dominant electroluminescence from a diode of monolayer MoS2. *Applied Physics Letters* 104: 193508. doi:10.1063/1.4875959.
77. Jariwala, Deep, Artur R. Davoyan, Joeson Wong, and Harry A. Atwater. 2017. Van der Waals Materials for Atomically-Thin Photovoltaics: Promise and Outlook. *ACS Photonics* 4: 2962–2970. doi:10.1021/acsphotonics.7b01103.
78. Lopez-Sanchez, Oriol, Dominik Lembke, Metin Kayci, Aleksandra Radenovic, and Andras Kis. 2013. Ultrasensitive photodetectors based on monolayer MoS_2. *Nature Nanotechnology* 8: 497–501. doi:10.1038/nnano.2013.100.
79. Yore, Alexander E., Kirby K. H. Smithe, Sauraj Jha, Kyle Ray, Eric Pop, and A. K. M. Newaz. 2017. Large array fabrication of high performance monolayer MoS2 photodetectors. *Applied Physics Letters* 111: 043110. doi:10.1063/1.4995984.
80. Mohamed, Nur Baizura, Feijiu Wang, Hong En Lim, Wenjin Zhang, Sandhaya Koirala, Shinichiro Mouri, Yuhei Miyauchi, and Kazunari Matsuda. 2017. Evaluation of photoluminescence quantum yield of monolayer WSe2 using reference dye of 3-borylbithiophene derivative. *physica status solidi (b)* 254: n/a-n/a. doi:10.1002/pssb.201600563.
81. Amani, Matin, Der-Hsien Lien, Daisuke Kiriya, Jun Xiao, Angelica Azcatl, Jiyoung Noh, Surabhi R. Madhvapathy, et al. 2015. Near-unity photoluminescence quantum yield in MoS2. *Science* 350: 1065–1068. doi:10.1126/science.aad2114.
82. Withers, F., O. Del Pozo-Zamudio, S. Schwarz, S. Dufferwiel, P. M. Walker, T. Godde, A. P. Rooney, et al. 2015. WSe2 Light-Emitting Tunneling Transistors with Enhanced Brightness at Room Temperature. *Nano Letters* 15: 8223–8228. doi:10.1021/acs.nanolett.5b03740.
83. Lien, Der-Hsien, Matin Amani, Sujay B. Desai, Geun Ho Ahn, Kevin Han, Jr-Hau He, Joel W. Ager, Ming C. Wu, and Ali Javey. 2018. Large-area and bright pulsed electroluminescence in monolayer semiconductors. *Nature Communications* 9: 1229. doi:10.1038/s41467-018-03218-8.
84. Eggleston, Michael S., Sujay B. Desai, Kevin Messer, Seth A. Fortuna, Surabhi Madhvapathy, Jun Xiao, Xiang Zhang, Eli Yablonovitch, Ali Javey, and Ming C. Wu. 2018. Ultrafast Spontaneous Emission from a Slot-Antenna Coupled WSe2 Monolayer. *ACS Photonics* 5: 2701–2705. doi:10.1021/acsphotonics.8b00381.
85. Akselrod, Gleb M., Tian Ming, Christos Argyropoulos, Thang B. Hoang, Yuxuan Lin, Xi Ling, David R. Smith, Jing Kong, and Maiken H. Mikkelsen. 2015. Leveraging Nanocavity Harmonics for Control of Optical Processes in 2D Semiconductors. *Nano Letters* 15: 3578–3584. doi:10.1021/acs.nanolett.5b01062.
86. Ceballos, Frank, Qiannan Cui, Matthew Z. Bellus, and Hui Zhao. 2016. Exciton formation in monolayer transition metal dichalcogenides. *Nanoscale* 8: 11681–11688. doi:10.1039/C6NR02516A.
87. Cui, Qiannan, Frank Ceballos, Nardeep Kumar, and Hui Zhao. 2014. Transient Absorption Microscopy of Monolayer and Bulk WSe2. *ACS Nano* 8: 2970–2976. doi:10.1021/nn500277y.

88. Steinleitner, Philipp, Philipp Merkl, Philipp Nagler, Joshua Mornhinweg, Christian Schüller, Tobias Korn, Alexey Chernikov, and Rupert Huber. 2017. Direct Observation of Ultrafast Exciton Formation in a Monolayer of WSe2. *Nano Letters* 17: 1455–1460. doi:10.1021/acs.nanolett.6b04422.
89. Kalt, Heinz, and Michael Hetterich. 2004. *Optics of Semiconductors and Their Nanostructures*. Springer Science & Business Media.
90. Robert, C., D. Lagarde, F. Cadiz, G. Wang, B. Lassagne, T. Amand, A. Balocchi, et al. 2016. Exciton radiative lifetime in transition metal dichalcogenide monolayers. *Physical Review B* 93: 205423. doi:10.1103/PhysRevB.93.205423.
91. Piermarocchi, C., F. Tassone, V. Savona, A. Quattropani, and P. Schwendimann. 1997. Exciton formation rates in GaAs/${\mathrm{Al}}_{\mathrm{x}}$${\mathrm{Ga}}_{1\mathrm{\ensuremath{-}}\mathrm{x}}$As quantum wells. *Physical Review B* 55: 1333–1336. doi:10.1103/PhysRevB.55.1333.
92. Bonnot, A., R. Planel, and C. Benoit à la Guillaume. 1974. Optical orientation of excitons in CdS. *Physical Review B* 9: 690–702. doi:10.1103/PhysRevB.9.690.
93. Robart, D, X Marie, B Baylac, T Amand, M Brousseau, G Bacquet, G Debart, R Planel, and J. M Gerard. 1995. Dynamical equilibrium between excitons and free carriers in quantum wells. *Solid State Communications* 95: 287–293. doi:10.1016/0038-1098(95)00265-0.
94. Strobel, R., R. Eccleston, J. Kuhl, and K. Köhler. 1991. Measurement of the exciton-formation time and the electron- and hole-tunneling times in a double-quantum-well structure. *Physical Review B* 43: 12564–12570. doi:10.1103/PhysRevB.43.12564.
95. Singh, Jasprit. 1995. *Semiconductor Optoelectronics: Physics and Technology*. McGraw-Hill College.
96. Jin, Zhenghe, Xiaodong Li, Jeffrey T. Mullen, and Ki Wook Kim. 2014. Intrinsic transport properties of electrons and holes in monolayer transition-metal dichalcogenides. *Physical Review B* 90: 045422. doi:10.1103/PhysRevB.90.045422.
97. Palummo, Maurizia, Marco Bernardi, and Jeffrey C. Grossman. 2015. Exciton Radiative Lifetimes in Two-Dimensional Transition Metal Dichalcogenides. *Nano Letters* 15: 2794–2800. doi:10.1021/nl503799t.
98. Shi, Hongyan, Rusen Yan, Simone Bertolazzi, Jacopo Brivio, Bo Gao, Andras Kis, Debdeep Jena, Huili Grace Xing, and Libai Huang. 2013. Exciton Dynamics in Suspended Monolayer and Few-Layer MoS2 2D Crystals. *ACS Nano* 7: 1072–1080. doi:10.1021/nn303973r.
99. Kumar, Nardeep, Qiannan Cui, Frank Ceballos, Dawei He, Yongsheng Wang, and Hui Zhao. 2014. Exciton-exciton annihilation in MoSe${}_{2}$ monolayers. *Physical Review B* 89: 125427. doi:10.1103/PhysRevB.89.125427.
100. Mouri, Shinichiro, Yuhei Miyauchi, Minglin Toh, Weijie Zhao, Goki Eda, and Kazunari Matsuda. 2014. Nonlinear photoluminescence in atomically thin layered ${\mathrm{WSe}}_{2}$ arising from diffusion-assisted exciton-exciton annihilation. *Physical Review B* 90: 155449. doi:10.1103/PhysRevB.90.155449.
101. Vilms, Jüri, and William E. Spicer. 1965. Quantum Efficiency and Radiative Lifetime in p-Type Gallium Arsenide. *Journal of Applied Physics* 36: 2815–2821. doi:10.1063/1.1714587.
102. Baranowski, M., A. Surrente, D. K. Maude, M. Ballottin, A. A. Mitioglu, P. C. M. Christianen, Y. C. Kung, D. Dumcenco, A. Kis, and P. Plochocka. 2017. Dark excitons

and the elusive valley polarization in transition metal dichalcogenides. *2D Materials* 4: 025016. doi:10.1088/2053-1583/aa58a0.
103. Malic, Ermin, Malte Selig, Maja Feierabend, Samuel Brem, Dominik Christiansen, Florian Wendler, Andreas Knorr, and Gunnar Berghäuser. 2018. Dark excitons in transition metal dichalcogenides. *Physical Review Materials* 2: 014002. doi:10.1103/PhysRevMaterials.2.014002.
104. Zhao, Peida, Matin Amani, Der-Hsien Lien, Geun Ho Ahn, Daisuke Kiriya, James P. Mastandrea, Joel W. Ager, Eli Yablonovitch, Daryl C. Chrzan, and Ali Javey. 2017. Measuring the Edge Recombination Velocity of Monolayer Semiconductors. *Nano Letters* 17: 5356–5360. doi:10.1021/acs.nanolett.7b01770.
105. Boroditsky, M., I. Gontijo, M. Jackson, R. Vrijen, E. Yablonovitch, T. Krauss, Chuan-Cheng Cheng, A. Scherer, R. Bhat, and M. Krames. 2000. Surface recombination measurements on III–V candidate materials for nanostructure light-emitting diodes. *Journal of Applied Physics* 87: 3497–3504. doi:10.1063/1.372372.
106. Hoshi, Yusuke, Takashi Kuroda, Mitsuhiro Okada, Rai Moriya, Satoru Masubuchi, Kenji Watanabe, Takashi Taniguchi, Ryo Kitaura, and Tomoki Machida. 2017. Suppression of exciton-exciton annihilation in tungsten disulfide monolayers encapsulated by hexagonal boron nitrides. *Physical Review B* 95: 241403. doi:10.1103/PhysRevB.95.241403.
107. Froehlicher, Guillaume, Etienne Lorchat, and Stéphane Berciaud. 2016. Direct versus indirect band gap emission and exciton-exciton annihilation in atomically thin molybdenum ditelluride $({\mathrm{MoTe}}_{2})$. *Physical Review B* 94: 085429. doi:10.1103/PhysRevB.94.085429.
108. Sun, Dezheng, Yi Rao, Georg A. Reider, Gugang Chen, Yumeng You, Louis Brézin, Avetik R. Harutyunyan, and Tony F. Heinz. 2014. Observation of Rapid Exciton–Exciton Annihilation in Monolayer Molybdenum Disulfide. *Nano Letters* 14: 5625–5629. doi:10.1021/nl5021975.
109. Man, Michael K. L., Skylar Deckoff-Jones, Andrew Winchester, Guangsha Shi, Gautam Gupta, Aditya D. Mohite, Swastik Kar, Emmanouil Kioupakis, Saikat Talapatra, and Keshav M. Dani. 2016. Protecting the properties of monolayer MoS_2 on silicon based substrates with an atomically thin buffer. *Scientific Reports* 6: 20890. doi:10.1038/srep20890.
110. Lien, Der-Hsien, Jeong Seuk Kang, Matin Amani, Kevin Chen, Mahmut Tosun, Hsin-Ping Wang, Tania Roy, et al. 2015. Engineering Light Outcoupling in 2D Materials. *Nano Letters* 15: 1356–1361. doi:10.1021/nl504632u.
111. Liu, Jiang-Tao, Hong Tong, Zhen-Hua Wu, Jin-Bao Huang, and Yun-Song Zhou. 2017. Greatly enhanced light emission of MoS 2 using photonic crystal heterojunction. *Scientific Reports* 7: 16391. doi:10.1038/s41598-017-16502-2.
112. Wang, Zegao, Qiang Li, Yuanfu Chen, Bianxiao Cui, Yanrong Li, Flemming Besenbacher, and Mingdong Dong. 2018. The ambipolar transport behavior of WSe 2 transistors and its analogue circuits. *NPG Asia Materials* 10: 703. doi:10.1038/s41427-018-0062-1.
113. Zhao, Weijie, Zohreh Ghorannevis, Leiqiang Chu, Minglin Toh, Christian Kloc, Ping-Heng Tan, and Goki Eda. 2013. Evolution of Electronic Structure in Atomically Thin Sheets of WS2 and WSe2. *ACS Nano* 7: 791–797. doi:10.1021/nn305275h.
114. Ahn, Geun Ho, Matin Amani, Haider Rasool, Der-Hsien Lien, James P. Mastandrea, Joel W. Ager Iii, Madan Dubey, Daryl C. Chrzan, Andrew M. Minor, and Ali Javey. 2017. Strain-engineered growth of two-dimensional materials. *Nature Communications* 8: 608. doi:10.1038/s41467-017-00516-5.

115. Kim, Hyungjin, Geun Ho Ahn, Joy Cho, Matin Amani, James P. Mastandrea, Catherine K. Groschner, Der-Hsien Lien, et al. 2019. Synthetic WSe2 monolayers with high photoluminescence quantum yield. *Science Advances* 5: eaau4728. doi:10.1126/sciadv.aau4728.
116. Pao, Y. C., K. Tran, C. Shih, and N. Hardy. *Solution to the E-beam Gate Resist Blistering Problem of 0.15 micron PHEMTs*.
117. Nagel, James R. 2013. Light extraction by Lambertian sources from light emitting diodes. In , ed. Bernd Witzigmann, Marek Osinski, Fritz Henneberger, and Yasuhiko Arakawa, 86190L. San Francisco, California, USA. doi:10.1117/12.2002115.
118. Compact Stabilized Broadband Light Sources. 2019. https://www.thorlabs.com/newgrouppage9.cfm?objectgroup_id=7269. Accessed January 18.
119. Liu, Hsiang-Lin, Chih-Chiang Shen, Sheng-Han Su, Chang-Lung Hsu, Ming-Yang Li, and Lain-Jong Li. 2014. Optical properties of monolayer transition metal dichalcogenides probed by spectroscopic ellipsometry. *Applied Physics Letters* 105: 201905. doi:10.1063/1.4901836.
120. Illarionov, Yury Yu, Theresia Knobloch, Michael Waltl, Gerhard Rzepa, Andreas Pospischil, Dmitry K. Polyushkin, Marco M. Furchi, Thomas Mueller, and Tibor Grasser. 2017. Energetic mapping of oxide traps in MoS2 field-effect transistors. *2D Materials* 4: 025108. doi:10.1088/2053-1583/aa734a.
121. Eggleston, Michael, Sujay Desai, Kevin Messer, Surabhi Madhvapathy, Jun Xiao, Xiang Zhang, Eli Yablonovitch, Ali Javey, and Ming C. Wu. 2015. Enhanced Spontaneous Emission from an Optical Antenna Coupled WSe_2 Monolayer. In *CLEO: 2015 (2015), paper FTu1E.5*, FTu1E.5. Optical Society of America. doi:10.1364/CLEO_QELS.2015.FTu1E.5.
122. Zan, Recep, Quentin M. Ramasse, Rashid Jalil, Thanasis Georgiou, Ursel Bangert, and Konstantin S. Novoselov. 2013. Control of Radiation Damage in MoS2 by Graphene Encapsulation. *ACS Nano* 7: 10167–10174. doi:10.1021/nn4044035.
123. Liu, Yuan, Jian Guo, Enbo Zhu, Lei Liao, Sung-Joon Lee, Mengning Ding, Imran Shakir, Vincent Gambin, Yu Huang, and Xiangfeng Duan. 2018. Approaching the Schottky–Mott limit in van der Waals metal–semiconductor junctions. *Nature* 557: 696. doi:10.1038/s41586-018-0129-8.
124. Hoole, A. C. F., M. E. Welland, and A. N. Broers. 1997. Negative PMMA as a high-resolution resist - the limits and possibilities. *Semiconductor Science and Technology* 12: 1166–1170. doi:10.1088/0268-1242/12/9/017.
125. Wu, Y. Q., H. C. Lin, P. D. Ye, and G. D. Wilk. 2007. Current transport and maximum dielectric strength of atomic-layer-deposited ultrathin Al2O3 on GaAs. *Applied Physics Letters* 90: 072105. doi:10.1063/1.2535528.
126. Li, Chenlei, Dajian Liu, and Daoxin Dai. 2019. Multimode silicon photonics. *Nanophotonics* 8: 227–247. doi:10.1515/nanoph-2018-0161.
127. McMahon, D. H. 1975. Efficiency limitations imposed by thermodynamics on optical coupling in fiber-optic data links*. *JOSA* 65: 1479–1482. doi:10.1364/JOSA.65.001479.
128. Massicotte, Mathieu, Fabien Vialla, Peter Schmidt, Mark B. Lundeberg, Simone Latini, Sten Haastrup, Mark Danovich, et al. 2018. Dissociation of two-dimensional excitons in monolayer WSe 2. *Nature Communications* 9: 1633. doi:10.1038/s41467-018-03864-y.
129. Gusakova, Julia, Xingli Wang, Li Lynn Shiau, Anna Krivosheeva, Victor Shaposhnikov, Victor Borisenko, Vasilii Gusakov, and Beng Kang Tay. 2017. Electronic Properties of

Bulk and Monolayer TMDs: Theoretical Study Within DFT Framework (GVJ-2e Method). *physica status solidi (a)* 214: 1700218. doi:10.1002/pssa.201700218.
130. Yuan, Long, Ti Wang, Tong Zhu, Mingwei Zhou, and Libai Huang. 2017. Exciton Dynamics, Transport, and Annihilation in Atomically Thin Two-Dimensional Semiconductors. *The Journal of Physical Chemistry Letters* 8: 3371–3379. doi:10.1021/acs.jpclett.7b00885.
131. Cordovilla Leon, Darwin F., Zidong Li, Sung Woon Jang, Che-Hsuan Cheng, and Parag B. Deotare. 2018. Exciton transport in strained monolayer WSe2. *Applied Physics Letters* 113: 252101. doi:10.1063/1.5063263.
132. Wu, Jianrong, and Keith M. Berland. 2008. Propagators and Time-Dependent Diffusion Coefficients for Anomalous Diffusion. *Biophysical Journal* 95: 2049–2052. doi:10.1529/biophysj.107.121608.
133. Grove, A. S. 1967. *Physics and Technology of Semiconductor Devices*.